Search for Third Generation Vector Leptoquarks in 1.96-TeV Proton-Antiproton Collisions

Takashi Akimoto

February 2007

Search for Third Generation Vector Leptoquarks in 1.96-TeV Proton-Antiproton Collisions

Takashi Akimoto

(Doctoral Program in Physics)

Submitted to the Graduate School of

Pure and Applied Sciences

in Partial Fulfillment of the Requirements

for the Degree of Doctor of Philosophy in

Science

at the

University of Tsukuba

Abstract

The CDF experiment has searched for production of a third generation vector leptoquark (VLQ3) in the di-tau plus di-jet channel using 322 pb^{-1} of Run II data. We review the production and decay theory and describe the VLQ3 model we have used as a benchmark. We study the analysis, including the data sample, triggers, particle identification, and event selection. We also discuss background estimates and systematic uncertainties. We have found no evidence for VLQ3 prodction and have set a 95% C.L. upper limit on the pair production cross section σ to 344 fb, and exclude VLQ3 in the mass range $m_{\mathrm{VLQ3}} > 317$ GeV/c^2, assuming Yang-Mills couplings and Br(LQ3 $\rightarrow b\tau$) $= 1$. If theoretical uncertainties on the cross section are taken into account, the results are $\sigma < 353$ fb and $m_{\mathrm{VLQ3}} > 303$ GeV/c^2. For a VLQ3 with Minimal couplings, the upper limit on the cross section is $\sigma < 493$ fb ($\sigma < 554$ fb) and the lower limit on the mass is $m_{\mathrm{VLQ3}} > 251$ GeV/c^2 ($m_{\mathrm{VLQ3}} > 235$ GeV/c^2) for the nominal (1σ varied) theoretical expectation.

Acknowledgments

This thesis could not have been completed without the support and encouragement of countless people. I would like to mention some of them here.

I would like to thank my adviser, Prof. Shinhong Kim for giving me really lots of great guidances and advices totally during 5 years of periods which I was working on the CDF experiment. You gave me an great chance to work at the world's highest collider experiment. I would like to thank Prof. Teruki Kamon for your many thoughtful advices. I would like to thank VLQ3 group people, Maxwell Chertok, Stanley Forrester, Yukihiro Kato, Richard Lander, Sung-Won Lee, Alexei Safonov, John R. Smith, Aron Soha and Soushi Tsuno for their useful help at critical times of the analysis. And I would like to thank Lepton+Track Trigger group people, Sasha Baroiant, Vadim Khotilovich, Takashi Ogawa and Andrew Ivanov. I am also grateful to the Exotics group conveners, Song Ming Wang, Jane Nachtman, Beate Heinemann and Stephan Lammel, who were very supportive and pushed me forward in my study. Special thanks are due to Aron Soha, who was everytime helpful for me. I really don't know how to thank you.

I am thankful to all the members of the high energy experiment group of University of Tsukuba, Koji Takikawa, Fumihiko Ukegawa, Kazuhiko Hara, Takasumi Maruyama, Yuji Takeuchi, Hiroyuki Matsunaga, Tomonobu Tomura and Kazuko Kumashiro. Also, I would like to thank all CDF students, Masato Aoki, Yoshio Ishizawa, Koji Sato, Hirokazu Kobayashi, Satoru Uozumi and Alberto Belloni, who shared great Fermilab life with me.

I really appreciate to my family, Hiroshi and Hiroko Akimoto, and my brothers and sister. You provided me with all of the warmth, support, and encouragement I could have ever wanted and more. Thank you.

This work was supported by the U.S. Department of Energy and National Science Foundation; the Italian Istituto Nazionale di Fisica Nucleare; the Ministry of Education, Culture, Sports, Science and Technology of Japan; the Natural Sciences and Engineering Research Council of Canada; the National Science Council of the Republic of China, the Swiss National Science Foundation; the A.P. Sloan Foundation; the Bundesministerium für Bildung und Forschung, Germany; the Korean Science and Engineering Foundation and the Korean Research Foundation; the Particle Physics and Astronomy Research Council and the Royal Society, UK; the Russian Foundation for Basic Research; the Comision Interministerial de Ciencia y Tecnologia, Spain; and in part by the European Community's Human Potential Programme under contract HPRN-CT-20002, Probe for New Physics.

Contents

List of Figures

List of Tables

Chapter 1

Introduction

1.1 Leptoquark Hypothesis

Common to many Standard Model extensions is a symmetry between leptons and quarks. Because the Standard Model has benefited from the relationship between symmetries and conserved quantities, it is common for theorists to attempt to connect the quark phenomenology and lepton phenomenology of the Standard Model. Any model which attempts to unify forces via more fundamental couplings is likely to introduce a coupling between quarks and leptons. If such a coupling exists, then there must be a gauge boson which is the carrier of force between them.

The existence of leptoquarks (LQs) is motivated by the striking parallels between the three generations of quarks and the three generations of leptons. The similarities suggest a possible link between the two sectors at higher mass scales, likely in the range $m \geq m_{\rm top}$. The phenomenology of leptoquarks is determined by the fact that they couple to both leptons and quarks, carrying both a lepton quantum number and a baryon quantum number. Figure 1.1 shows the two general categories of LQ couplings. One LQ decays into quark and lepton, the other LQ decays into quark and neutorino. Furthermore, LQs are color-triplet bosons, with fractional charge. Leptoquark theory provides two possible spin structures: scalar ($\rm spin = 0$) LQs have fixed couplings and decay isotropically, while vector ($\rm spin = 1$) LQs have what are called anomalous magnetic dipole and electric quadrupole moments.

This section discusses the variety of LQs that may exist, and Sections 1.2 and 1.3 detail the production cross section and decay mechanisms for the $3^{\rm rd}$ generation vector leptoquarks we are considering. One of the most compelling motivations for leptoquarks is that they appear in a consistent way in a wide range of theories, including SU(5) GUT [1], Superstrings, SU(4) Pati-Salam [2], Compositeness [3], and Technicolor [4]. The Particle Data Group includes a short review article on leptoquarks [5].

The leptoquark search carried out here assumes a Lagrangian, as formulated by Buchmüller *et al.* [6], which satisfies the SU(3)×SU(2)×U(1) group combination. As done in a CDF Run I search [7, 8], we accept the following three restrictions: we assume lepton and baryon number

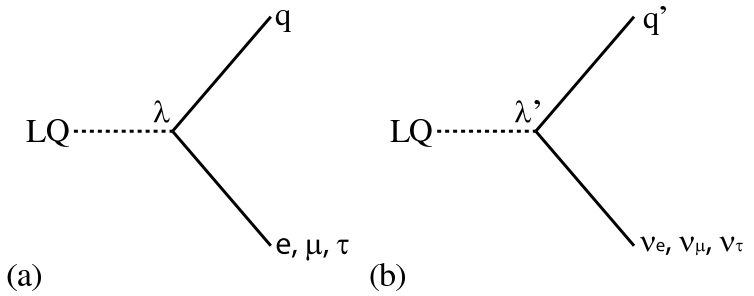

Figure 1.1: Two classes of leptoquark couplings.

conservation, and couplings that remain within a given generation, so as to agree with the lack of flavor changing neutral currents; we assume couplings that are chiral, so as to prevent a rate of $\pi \rightarrow e\nu$ decays that is beyond what is experimentally observed. The resulting possible LQ species are listed in Table 1.1 [6].

1.2 Production Cross Section

At the Tevatron, leptoquarks can be produced via two primary processes. The leading order Feynman diagrams on the quark-antiquark annihilation processes are shown in Figure 1.2. The second process, gluon-gluon fusion, is depicted in Figure 1.3. For LQ masses that have not previously been excluded, the quark anti-quark annihilation process dominates at the Tevatron.

The effective Lagrangian is given by

$$L = L_S^g + L_V^g, \tag{1.1}$$

where

$$L_S^g = \sum_{scalars} \left[(D_{ij}^{\mu} \Phi^j)^{\dagger} (D_{\mu}^{ik} \Phi_k) - M_S^2 \Phi^{i\dagger} \Phi_i \right] \tag{1.2}$$

and

$$L_V^g = \sum_{vectors} \left[-\frac{1}{2} G_{\mu\nu}^{i\dagger} G_i^{\mu\nu} + M_V^2 \Phi_{\mu}^{i\dagger} \Phi_i^{\mu} - i g_s \left[(1-\kappa) \Phi_{\mu}^{i\dagger} t_{ij}^a \Phi_{\nu}^j \mathcal{G}_a^{\mu\nu} + \frac{\lambda}{M_V^2} G_{\sigma\mu}^{i\dagger} t_{ij}^a G_{\nu}^{j\mu} \mathcal{G}_a^{\nu\sigma} \right] \right]. \tag{1.3}$$

In the above Lagrangians, g_s is the strong coupling constant, t^a are the generators of SU$(3)_{\rm C}$ (in the appropriate representation), M_S and M_V are the scalar and vector Leptoquark masses and κ and λ are the anomalous couplings. κ and λ are assumed to be real and are related to the anomalous magnetic moment, μ_V, and electric quadrupole moment, q_V, by the following relationship

$$\mu_V = \frac{g_s}{2M_V}(2 - \kappa + \lambda) \tag{1.4}$$

$$q_V = -\frac{g_s}{M_V^2}(1 - \kappa - \lambda) \tag{1.5}$$

Table 1.1: Quantum numbers, decay channels, and couplings for species of scalar and vector leptoquarks. The subscript on the LQ is the dimensionality of the SU(2) group representation, as also given in the fifth column. The third column gives the fermion number, F = 3B+L, where B is the baryon quantum number and L is the the lepton quantum number. In the last column, L and R refer to the tau chirality.

LQ	Spin	3B+L	$SU(3)_C$	$SU(2)_W$	$U(1)_Y$	Q_{EM}	Channel(s) [coupling(s)]
S_1	0	-2	3^*	1	$\frac{1}{3}$	$-\frac{1}{3}$	$\tau^-_{L,R}t\ [g_{1L,R}],\ \nu_L b\ [-g_{1L}]$
$\tilde{S}_1$	0	-2	3^*	1	$\frac{4}{3}$	$-\frac{4}{3}$	$\tau^-_R b\ [\tilde{g}_{1R}]$
S_3	0	-2	3^*	3	$\frac{1}{3}$	$\frac{2}{3}$	$\nu_L t\ [\sqrt{2}g_{3L}]$
						$-\frac{1}{3}$	$\tau^-_L t\ [-g_{3L}],\ \nu_L b\ [-g_{3L}]$
						$-\frac{4}{3}$	$\tau^-_L b\ [-\sqrt{2}g_{3L}]$
V_2	1	-2	3^*	2	$\frac{5}{6}$	$-\frac{1}{3}$	$\tau^-_R t\ [g_{2R}],\ \nu_L b\ [g_{2L}]$
						$-\frac{4}{3}$	$\tau^-_{L,R}b\ [g_{2L,R}]$
$\tilde{V}_2$	1	-2	3^*	2	$-\frac{1}{6}$	$\frac{2}{3}$	$\nu_L t\ [\tilde{g}_{2L}]$
						$-\frac{1}{3}$	$\tau^-_L t\ [\tilde{g}_{2L}]$
R_2	0	0	3	2	$\frac{7}{6}$	$-\frac{2}{3}$	$\tau^-_R\overline{b}\ [-h_{2R}],\ \nu_L\overline{t}\ [h_{2L}]$
						$-\frac{5}{3}$	$\tau^-_{L,R}\overline{t}\ [h_{2L,R}]$
$\tilde{R}_2$	0	0	3	2	$\frac{1}{6}$	$\frac{1}{3}$	$\nu_L\overline{b}\ [\tilde{h}_{2L}]$
						$-\frac{2}{3}$	$\tau^-_L\overline{b}\ [\tilde{h}_{2L}]$
U_1	1	0	3	1	$\frac{2}{3}$	$-\frac{2}{3}$	$\tau^-_{L,R}\overline{b}\ [h_{1L,R}],\ \nu_L\overline{t}\ [h_{1L}]$
$\tilde{U}_1$	1	0	3	1	$\frac{5}{3}$	$-\frac{5}{3}$	$\tau^-_R\overline{t}\ [\tilde{h}_{1R}]$
U_3	1	0	3	3	$\frac{2}{3}$	$\frac{1}{3}$	$\nu_L\overline{b}\ [\sqrt{2}h_{3L}]$
						$-\frac{2}{3}$	$\tau^-_L\overline{b}\ [-h_{3L}],\ \nu_L\overline{t}\ [h_{3L}]$
						$-\frac{5}{3}$	$\tau^-_L\overline{t}\ [\sqrt{2}h_{3L}]$

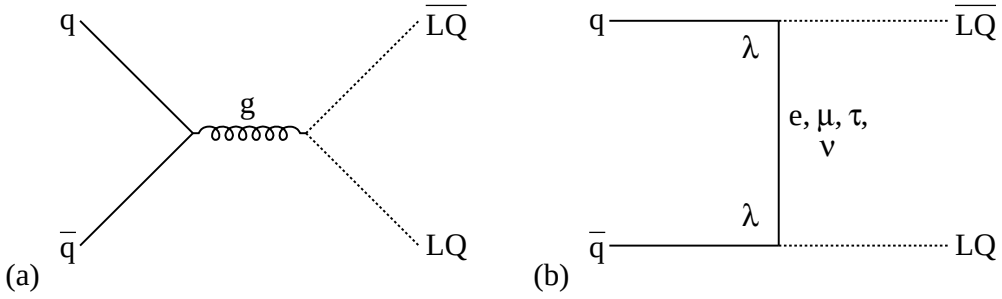

Figure 1.2: Leading order Feynman diagrams for leptoquark pair-production by quark anti-quark annihilation. Diagram (a) dominates, while diagram (b) has two instances of the LQ-quark-lepton coupling, λ, which for the third generation would require top or bottom quarks to be present in the initial state.

The tensors for the field strength for the gluon and vector leptoquark field are given by

$$\mathcal{G}^a_{\mu\nu} = \partial_\mu \mathcal{A}^a_\nu - \partial \mathcal{A}^a_\mu + g_s f^{abc} \mathcal{A}_{a\mu} \mathcal{A}_{b\nu}, \tag{1.6}$$

$$\mathcal{G}^i_{\mu\nu} = D^{ik}_\mu \Phi_{\nu k} - D^{ik} \Phi_{\mu k}, \tag{1.7}$$

This lagrangian is model independent modulo anomalous couplings for the magnetic moment and the electric quadrapole moment of the Leptoquarks in the color field. The case of $\kappa = \lambda = 0$ corresponds to the assumption that the Vector Leptoquark couples like a Yang-Mills gauge field and the case $\kappa = 1$, $\lambda = 0$ corresponds to the case of Minimal Vector type coupling, following the particular conventions as in [10].

Previously, no tool existed to accurately simulate the pair-production and decay of $3^{\rm d}$ generation vector leptoquarks (VLQ3s). We have implemented the first such generator for vector leptoquarks, the details of which are documented elsewhere [11]. The new production channel has been added using the GRACE matrix element generator and the GR@PPA interface. This yields the pair-production cross section, as well as a set of events that run through the full CDF simulation software.

The VLQ3 pair production cross section ($\sigma_{\rm VLQ3\overline{VLQ3}}$) is shown in Table 1.2. Figure 1.4 shows the total pair production cross section, as well as the contributions from quark anti-quark annihilation and gluon-gluon fusion, all for the case where $\mathrm{Br}(\mathrm{VLQ3} \to b\tau) = 1$. Figure 1.5 shows the impact on total cross section due to the $\mathrm{Br}(\mathrm{VLQ3} \to b\tau) = 1$ requirement. We used the CTEQ5L PDF library and $Q^2 = m^2_{\rm VLQ3}$. The systematics related to these choices are discussed in Section 5.1.2.

1.3 Decay

It is common to define the quantity $\beta = \mathrm{Br}(\mathrm{LQ} \to \ell q)$ to categorize the possible leptoquark decay channels. The diagram in Figure 1.1(a) corresponds to $\beta = 1$ while the diagram in Figure 1.1(b)

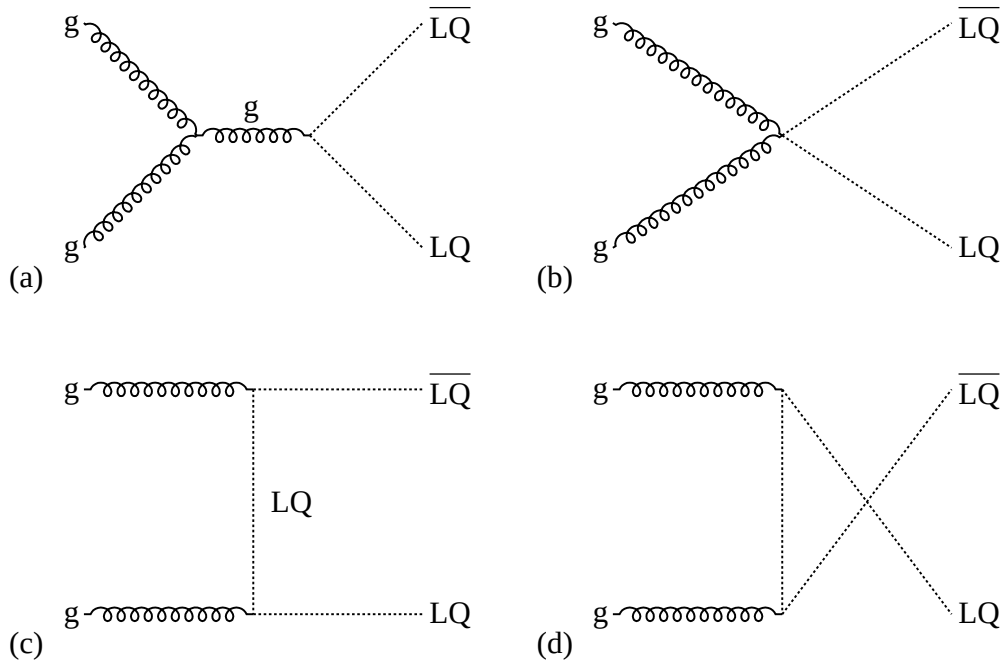

Figure 1.3: Leading order Feynman diagrams for leptoquark pair-production by gluon-gluon fusion. At the Tevatron, the contribution from the gluon-gluon fusion process is predicted to be about ten times smaller than that due to quark anti-quark annihilation.

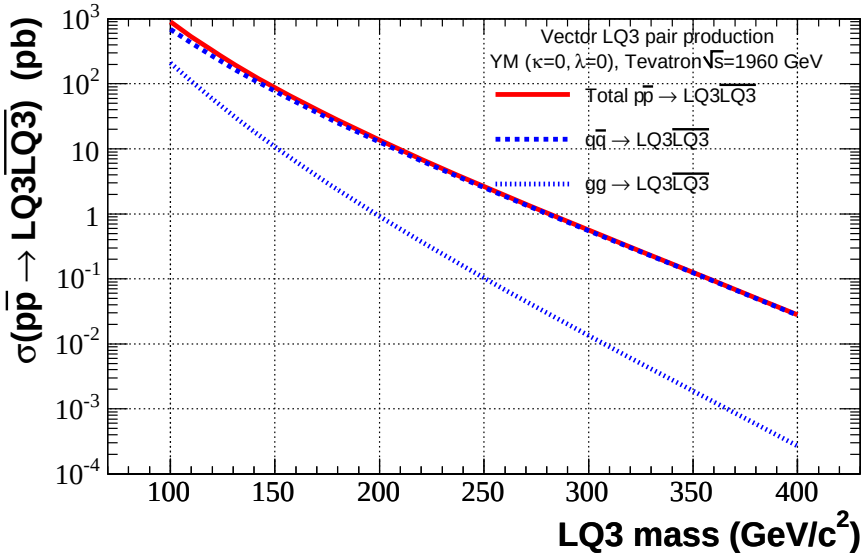

Figure 1.4: Pair production cross section as a function of VLQ3 mass for the total (solid red), quark anti-quark annihilation contribution (dashed blue), and gluon-gluon fusion contribution (dotted blue). In these cases the the generator uses Yang-Mills couplings and $\mathrm{Br}(\mathrm{VLQ3} \to b\tau) = 1$. The numbers corresponding to the total are given in Table 1.2.

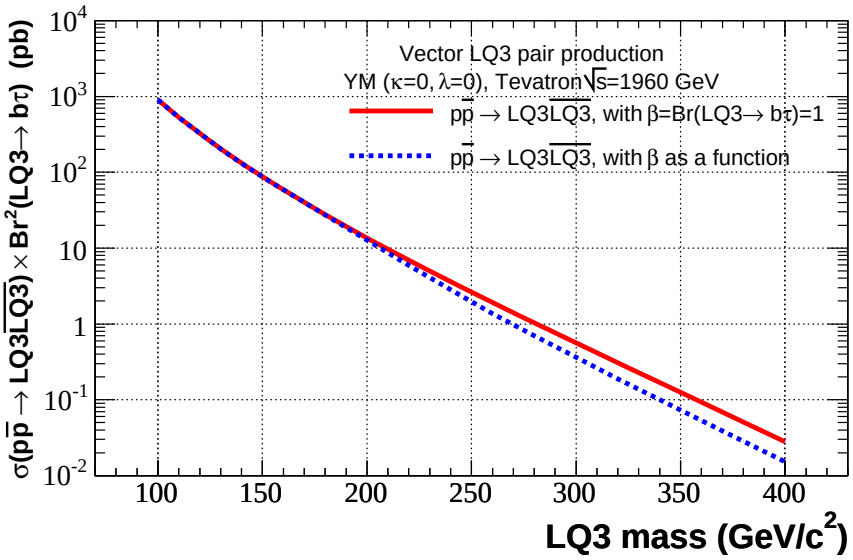

Figure 1.5: Pair production cross section as a function of VLQ3 mass with $\beta = 1$ (solid red) and with β included as a function in the generator (dashed blue). Note, the vertical scale is different from that of Figure 1.4, but the red curve is the same.

.

Table 1.2: Cross section, in pb, for VLQ3 pair production at the Tevatron using the GRACE/GR@PPA matrix element generator, for a various of VLQ3 masses, and assuming Yang-Mills couplings.

$m_{\mathrm{VLQ3}}\,(\mathrm{GeV}/c^2)$	100	120	140	160	180	200	220	240
$\sigma_{\mathrm{VLQ3}\overline{\mathrm{VLQ3}}}\,(\mathrm{pb})$	898.4	324.5	132.1	58.55	27.59	13.60	6.928	3.614

$m_{\mathrm{LQ3}}\,(\mathrm{GeV}/c^2)$	260	280	300	320	340	360	380	400
$\sigma_{\mathrm{VLQ3}\overline{\mathrm{VLQ3}}}\,(\mathrm{pb})$	1.911	1.035	0.562	0.307	0.169	0.093	0.051	0.028

corresponds to $\beta = 0$. In this analysis, we search for VLQ3 $\rightarrow \tau^{-}\overline{b}$, which has $\beta = 1$, and is called the type U_1 in Table 1.1.

Because the LQs are pair-produced, the final state contains two taus and two b quarks. The signature we search for is one tau decaying leptonically to an electron or muon, one tau decaying hadronically to two jets. This combination of $\tau_e^{\pm}\tau_h^{\mp}b\overline{b}$ or $\tau_\mu^{\pm}\tau_h^{\mp}b\overline{b}$ represents 46% of the possible $\tau\tau$ decay variations.

The choice of this signature is motivated in the following two points: First we have to select a channel where the decay products can be triggered, and candidate events have to be obtained with a large ratio of signal over background. The $\tau_\ell\tau_h bb$ final state is well selected with a *Lepton+Track* trigger (see Section 3.2). On the other hand, each of the νb, νt, and τt decay modes (LQ3 pair production leading to potential mixtures of these decay modes) represents significantly different analyses, likely with more challenging backgrounds. Second, we select the U_1 type for its simplicity: with β set to 1 (so no contribution from $\nu\overline{t}$), the decay is entirely to the $\tau\overline{b}$ channel (with no contribution through τt). In addition to leptoquarks of the type named U_1, we are also potentially sensitive to decays from the vector leptoquarks named V_2 and U_3, as well as the scalar leptoquarks named $\tilde{S}_1$, S_3, R_2, and $\tilde{R}_2$, as shown in Table 1. This is because they all potentially share the final state of τb, and so if we were to see a statistically significant excess in this channel it could represent the discovery of one or more of these species. Also note that if the true value of β is not 1 ($\beta \neq 1$), it does not change which decay modes we consider in this analysis, but instead changes the expected relative branching ratio between $\tau\overline{b}$ and $\nu\overline{t}$ in the case of U_1. This would weaken our limits.

1.4 History of Search for Leptoquarks

In February 1997, a sign of a leptoquark signature has been seen at HERA. The H1 [12] and ZEUS [13] collaborations working on $e^{+}p$ collisions at HERA simultaneously released papers reporting an excess of neutral-current deep-inelastic scattering events with high Q^2. Since the reports, a large number of papers have been published on experimental leptoquark mass limits. H1 found 12 events with $Q^2 > 15,000\ \mathrm{GeV}^2$ where the Standard Model (SM) predicts 4.71 ± 0.76, and ZEUS found 2 events with $Q^2 > 35,000\ \mathrm{GeV}^2$ in comparison to the SM prediction of 0.145 ± 0.013 events for that range of Q^2. The probability that these excesses were due to statistical fluction was 0.5%. Then at the Lepton-Photon conference in 1997, H1 and ZEUS reported more neutral current events as well as charged current events from data taken up to June of that year [14] [15]. Collectively, they found 22 charged current events with a $Q^2 > 10,000\ \mathrm{GeV}^2$ where the SM predicts 17.7 ± 4.3 events. So, any leptoquark theory would have to account for not only neutral currents, but charged current as well.

What made the excess more interesting was that H1 observed a cluster of the events at a mass of about $200\ \mathrm{GeV}/c^2$. This excess could be explained by the existence of 1^{st} generation scalar leptoquarks, including scalar squarks in supersymmetric theories with R-parity violation (RPV). But if low mass scalar leptoquarks exist, they would be produced at significant rates at a $p\bar{p}$ collider. So, immediately both CDF [16] and DØ [17] conducted searches for leptoquarks using Tevatron

Run I data and reported a combined lower limit of $M_S > 242$ GeV/c^2 [18]. For the vector leptoquark case, even at choice of κ and λ such that the cross section is minimized [9], the lower mass bounds were significantly higher than the scalar limit.

The leptoquark searches from Run I at the Tevatron exclude the interpretaion of the excess events found at HERA as being a result of the production of a leptoquark state with chiral and family-diagonal coupling to fermions [19]. ZEUS also observed a cluster in their data, but at a mass of about 220 GeV/c^2. This difference in mass between H1's cluster and ZEUS's cluster was later ruled out by being the cause of initial state radiation or detector effects [14]. Thus it has been ruled unlikely that the excess observed at HERA was due to the production and decay of a single narrow resonance. Since then, the data collected at H1 and ZEUS have doubled, however, no excess events have been observed.

Continuously, the limits of the leptoquarks are updated by the Tevatron Run II. For the 1$^{\rm st}$ and 2$^{\rm nd}$ generation scalar leptoquark states with decay branching fraction $\beta = 1$, the CDF and DØ experiments obtain the lower limits on the leptoquark mass > 235 GeV/c^2 (1$^{\rm st}$ generation, CDF), > 256 GeV/c^2 (1$^{\rm st}$ generation, DØ), > 224 GeV/c^2 (2$^{\rm nd}$ generation, CDF) and > 251 GeV/c^2 (2$^{\rm nd}$ generation, DØ) at the 95% C.L. For the 3$^{\rm rd}$ generation scalar leptoquark, the CDF set a limit > 129 GeV/c^2, which also set a limit of RPV scalar top mass [20].

For the vector leptoquark, the CDF Run I obtained the lower limit on VLQ3 mass [7]. The lower limits on the VLQ3 mass are following two cases:

- $m_{\rm VLQ3} > 225$ GeV/c^2 for Yang-Mills couplings.
- $m_{\rm VLQ3} > 170$ GeV/c^2 for Minimal couplings.

These limits are latest for 3$^{\rm rd}$ generation vector leptoquark before this analysis.

1.5 Comments on *b*-Tagging

Because the final state contains two b quarks, one can consider requiring one or two b-tagged jets in the event selection. These options have been explored, but with the relatively low efficiency of b-tagging, the reduction in signal due to requiring even a single loose b-tag would reduce the sensitivity (the background level is already low enough that any further reduction in backgrounds would not make up for the loss of signal efficiency). Loosening other cuts, such as tau ID, while adding b-tagging is a possible improvement for a future version of this analysis, but the complexity of allowing more fake taus, in combination with understanding the b-tagging efficiency and mis-tag rates on these events, would have added considerable time to the completion of this round of the analysis.

We have performed a rough quantitative estimate of the impact of requiring at least one b-tag. The b-tagging efficiency for one "loose" b-tag is $\sim 45\%$, and so the expected fraction of signal events that would have at least one b-tag is $\sim 70\%$. In the $e\tau_h$ and $\mu\tau_h$ channels combined, the signal/background would change from roughly 5.5 to 8.5 after adding the b-tagging requirement, while the sensitivity ($S/\sqrt{S+B}$) would change from about 1.5 to 1.3. In this estimate we have

accounted for the fact that the majority of the background in the signal region is from $\bar{t}t$ events, which will pass a b-tagging requirement at a similar rate to that of our $\tau_\ell\tau_h bb$ signal.

Chapter 2

Experimental Setup

The Fermilab Tevatron Collider represents the high energy frontier in particle physics. It is currently the source of the highest energy proton-antiproton ($p\bar{p}$) collisions. The collisions occur at two points on an underground ring, which has a radius of about 1 km. At these collision points there are two detectors: the Collider Detector at Fermilab (CDF II) and DØ. This analysis uses data collected with the CDF II Detector.

Between 1997 and 2001, both the accelerator complex and the collider detectors underwent major upgrades, mainly aimed at increasing the luminosity of the accelerator, and gathering data samples of $2\ \mathrm{fb}^{-1}$ or more. The upgraded machine accelerates 36 bunches of protons and antiprotons, whereas the previous version of the accelerator operated with only 6. Consequently, the time between bunch crossings has been decreased from 3.5 μs for the previous version to 396 ns for the current collider.

The new configuration required detector upgrades at CDF II to ensure a maximum response time shorter than the time between beam crossings. In the following pages, we describe how the proton and antiproton beams are produced, accelerated to their final center of mass energy of 1.96 TeV, and collided. We then describe the components used to identify and measure properties of the particles produced in the collision.

2.1 The Tevatron Collider

To create the world's most powerful particle beams, Fermilab uses a series of accelerators. The diagram in Figure 2.1 shows the paths taken by protons and antiprotons from initial acceleration to collision in the Tevatron.

The Cockcroft-Walton [21] pre-accelerator provides the first stage of acceleration. Inside this device, hydrogen gas is ionized to create H^- ions, which are accelerated to 750 keV of kinetic energy. Next, the H^- ions enter a linear accelerator (Linac) [22], approximately 500 feet long, where they are accelerated to 400 MeV. The acceleration in the Linac is done by a series of "kicks" from Radio Frequency (RF) cavities. The oscillating electric field of the RF cavities groups the ions into bunches.

The 400 MeV H^- ions are then injected into the Booster, a circular synchrotron [22] $74.5\ \mathrm{m}$

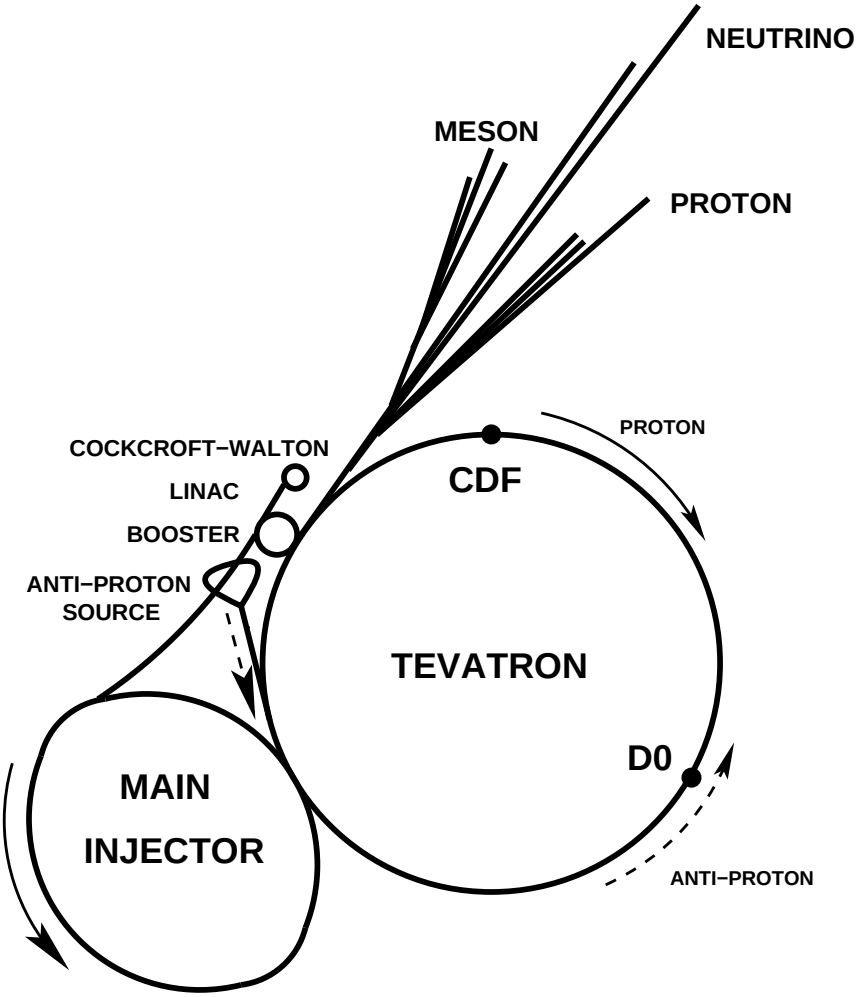

Figure 2.1: Layout of the Fermilab accelerator complex.

in diameter. A carbon foil strips the electrons from the H^- ions at injection, leaving bare protons. The intensity of the proton beam is increased by injecting new protons into the same orbit as the circulating ones. The protons are accelerated from 400 MeV to 8 GeV by a series of "kicks" applied by RF cavities. Each turn around the Booster, the protons accrue about 500 keV of kinetic energy.

Protons are extracted from the Booster into the Main Injector [23], which operates at 53 MHz. It has four functions. It accelerates protons from 8 GeV to 150 GeV before injection into the Tevatron, it produces 120 GeV protons which are used for antiproton production, it receives antiprotons from the Antiproton Source and accelerates them to 150 GeV for injection into the Tevatron, and finally, it injects protons and antiprotons into the Tevatron.

The Main Injector replaced the Main Ring accelerator which was situated in the Tevatron tunnel. The Injector is capable of containing larger proton currents than its predecessor, which results in a higher rate of antiproton production. The Main Injector tunnel also houses the Antiproton Recycler. Not all antiprotons in a given store are used up by the collisions. Recycling the unused antiprotons and reusing them in the next store significantly reduces the stacking time. The task of the Antiproton Recycler is to receive antiprotons from a Tevatron store, cool them and re-integrate them into the stack, so that they can be used in the next store.

To produce antiprotons, 120 GeV protons from the Main Injector are directed into a nickel target. In the collisions, about 20 antiprotons are produced per one million protons, with a mean kinetic energy of 8 GeV. The antiprotons are focused by a lithium lens and separated from other particle species by a pulsed magnet.

Before the antiprotons can be used in the narrow beams needed in the collider, the differences in kinetic energy between the different particles need to be reduced. Since this process reduces the spread of the kinetic energy spectrum of the beam, it is referred to as "cooling" the beam. New batches of antiprotons are initially cooled in the Debuncher synchrotron, collected and further cooled using stochastic cooling [24] in the 8 GeV Accumulator synchrotron. The principle of stochastic cooling is to sample a particles motion with a pickup sensor and correct its trajectory later with a kicker magnet. In reality, the pickup sensor samples the average motion of particles in the beam and corrects for the average. Integrated over a long period of time, this manifests itself as a damping force applied onto individual particles which evens out their kinetic energies. It takes between 10 and 20 hours to build up a "stack" of antiprotons which is then used in collisions in the Tevatron. Antiproton availability is the most limiting factor for attaining high luminosities, assuming there are no technical problems with the accelerator (assuming, for example, perfect transfer efficiencies between accelerator subsystems) [22, 23].

Roughly once a day, the stacked antiprotons (36 bunches of about 3×10^{10} antiprotons per bunch) are injected back into the Main Injector. They are accelerated to 150 GeV together with 36 bunches of roughly 3×10^{11} protons. Both the protons and antiprotons are transferred to the Tevatron.

The Tevatron is the last stage of Fermilab's accelerator chain. It receives 150 GeV protons and antiprotons from the Main Injector and accelerates them to 980 GeV. The protons and antiprotons circle the Tevatron in opposite directions. The beams are brought to collision at two "collision

parameter	Run I	Run II
Number of bunches (N_B)	6	36
Bunch length [m]	0.6	0.37
Bunch spacing [ns]	3500	396
Protons/bunch (N_p)	2.3×10^{11}	2.7×10^{11}
Antiprotons/bunch ($N_{\bar{p}}$)	5.5×10^{10}	3.0×10^{10}
Total antiprotons	3.3×10^{11}	1.1×10^{12}
β^* [cm]	35	35
Interactions/crossing	2.5	2.3
Integrated luminosity [pb^{-1}]	112	450
Peak luminosity [$\mathrm{cm}^{-2}\mathrm{s}^{-1}$]	2×10^{31}	1.2×10^{32}

Table 2.1: Accelerator parameters for Run I and Run II configurations.

points," B0 and DØ. The two collider detectors, the Collider Detector at Fermilab (CDF II) and DØ, are built around the respective collision points.

The luminosity of collisions can be expressed as:

$$\mathcal{L} = \frac{f N_B N_p N_{\bar{p}}}{2\pi(\sigma_p^2 + \sigma_{\bar{p}}^2)} F\left(\frac{\sigma_l}{\beta^*}\right), \tag{2.1}$$

where f is the revolution frequency, N_B is the number of bunches, $N_{p(\bar{p})}$ is the number of protons(antiprotons) per bunch, and $\sigma_{p(\bar{p})}$ is the protons(antiprotons) rms beam size at the interaction point. F is a form factor which corrects for the bunch shape and depends on the ratio of q, the bunch length to β^*, the beta function, at the interaction point. The beta function is a measure of the beam width, and it is proportional to the beam's x and y extent in phase space.

Table 2.1 shows a comparison of Run I and design Run II [23] accelerator parameters.

2.2 The CDF II Detector

The CDF II Detector [25] is a substantial upgrade of the original CDF Detector [26]. It is located at the B0 collision point of the Tevatron Collider. The detector is designed to detect and measure properties of particles emanating from $p\bar{p}$ collisions. The design is not geared toward one particular physics measurement, but rather optimized toward extracting a number of different properties about all particle species created in the $p\bar{p}$ collision. Such particle detectors are often called multi-purpose detectors.

A diagram of the CDF II Detector is shown in Figure 2.2. A quadrant of the detector is cut out to expose the different subdetectors. The detector subsystems can be grouped as follows. The innermost system is the integrated tracking system. The tracking system is barrel-shaped and consists of cylindrical subsystems which are concentric with the beam. It is designed to detect charged particles, measure their momenta and displacements from the point of collision (primary interaction vertex). The tracking system is surrounded by the Time-of-Flight system, designed to

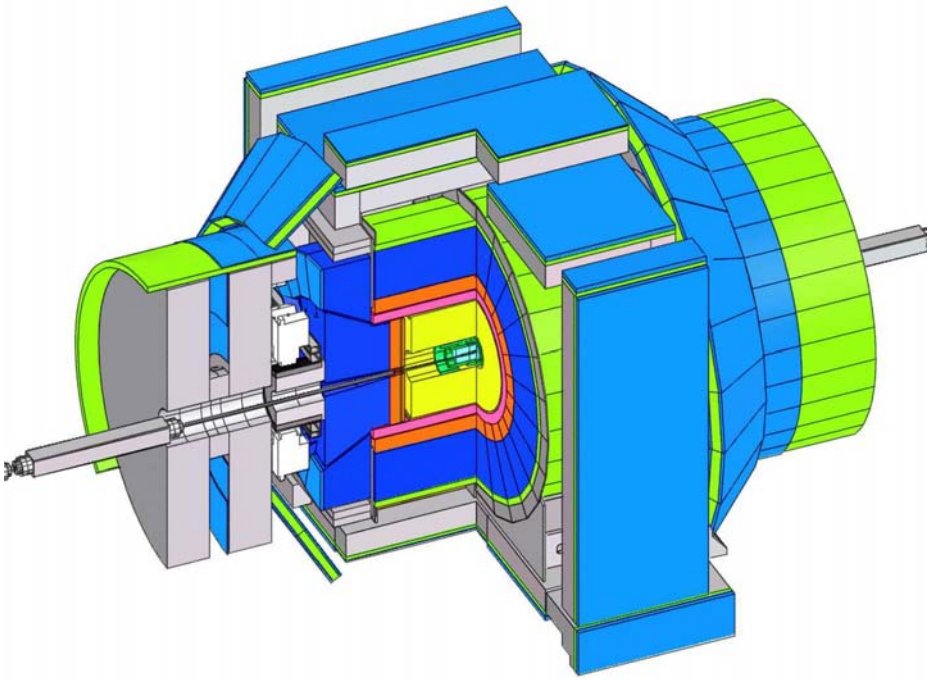

Figure 2.2: The CDF II Detector with quadrant cut to expose the different subdetectors.

provide particle identification for low-momentum charged particles. Both the tracking and Time of Flight systems are placed inside a superconducting coil, which generates a 1.4 T solenoidal magnetic field. The coil is surrounded by calorimetry systems, which measure the energy of particles that shower when interacting with matter. The calorimetry systems are surrounded by muon detector systems. When interacting with matter, muons act as "minimally ionizing particles" - they only deposit small amounts of ionization energy in the material. Therefore, they are able to penetrate both the tracking and calorimeter systems. The integrated material of the tracking system, TOF, solenoid and calorimetry systems serves as a particle filter. Particles which penetrate through all that material are mostly muons, and they are detected by leaving tracks in the muon detection system, located outside of the calorimeter.

The most important parts of the detector for this analysis are the tracking system and the trigger, and these will be described in detail in the following sections. The description of the remaining systems will be brief. More detailed information on these systems can be found in the Technical Design Reports of the CDF II Detector [26, 25].

2.3 Coordinate System in CDF

Because of its barrel-like detector shape, the CDF II Detector uses a cylindrical coordinate system (r, ϕ, z) with the origin at the center of the detector and the z-axis along the nominal direction of the proton beam. The y-axis points upwards. Since the coordinate system is right-handed, this also defines the direction of the x-axis. Particles moving through a homogeneous solenoidal magnetic field follow helical trajectories. Reconstructed charged particle trajectories are referred

to as "tracks". The plane perpendicular to the beam is referred to as the "transverse plane", and the transverse momentum of the track is referred to as p_T. As opposed to e^+e^- collisions, in $p\bar{p}$ collisions not all of the center of mass energy of the $p\bar{p}$ system is absorbed in the collision. The colliding partons inside the proton carry only a fraction of the kinetic energy of the proton. As a result, the center of mass system of the parton collisions is boosted along the beam direction (the "longitudinal" direction) by an unknown amount, but quantities defined in the transverse plane are conserved in the collisions. For instance, the sum of all transverse momenta of particles in a collision is zero, $\sum \vec{p_T} = 0$.

To uniquely parameterize a helix in three dimensions, five parameters are needed. The CDF coordinate system chooses three of these parameters to describe a position, and two more to describe the momentum vector at that position. The three parameters which describe a position describe the point of closest approach of the helix to the beam line. These parameters are d_0, ϕ_0, and z_0, which are the r, ϕ and z cylindrical coordinates of the point of closest approach of the helix to the beam. The momentum vector is described by the track curvature (c) and the angle of the momentum in the $r-z$ plane ($\cot\theta$). From the track curvature we can calculate the transverse momentum. The curvature is signed so that the charge of the particle matches the charge of the curvature. From $\cot\theta$, we can calculate $p_z = p_T \cdot \cot\theta$. At any given point of the helix, the track momentum is a tangent to the helix. This basically means that the angle ϕ_0 implicitly defines the direction of the transverse momentum vector at the point of closest approach, $\vec{p_T}$.

The impact parameter (d_0) of a track is another signed variable; its absolute value corresponds to the distance of closest approach of the track to the beamline. The sign of d_0 is taken to be that of $\hat{p} \times \hat{d} \cdot \hat{z}$, where $\hat{p}$, $\hat{d}$ and $\hat{z}$ are unit vectors in the directions of $\vec{p}$, $\vec{d_0}$ and $\vec{z}$, respectively. An alternate variable that describes the angle between the z-axis and the momentum of the particle is the pseudorapidity η, which is defined as:

$$\eta \equiv -\ln\tan\left(\frac{\theta}{2}\right). \tag{2.2}$$

For decaying particles, we often define the displacement L_{xy},

$$L_{xy} = \vec{d} \cdot \hat{p_T}\,, \tag{2.3}$$

where $\vec{d}$ is the displacement of the decay vertex, and $\hat{p_T}$ is the unit vector in the direction of $\vec{p_T}$.

2.4 Tracking Systems

The detector has a cylindrical tracking system immersed in a 1.4 T solenoidal magnetic field for the measurement of charged-particles momenta. We will describe this system starting from the devices closest to the beam and moving outwards. The innermost tracking device is a silicon strip vertex detector, which consists of three subdetectors. A layer of silicon sensors, called Layer 00 (L00) [27], is installed directly onto the beryllium vacuum beam pipe, with the sensors at radii 1.35 and 1.62 cm from the beam. The beam pipe is made of beryllium because this metal has the best mechanical qualities, yet lowest nuclear interaction cross section of all materials.

The layer of silicon on the beam pipe is followed by five concentric layers of silicon sensors (SVX-II) [28] located at radii between 2.45 and 10.6 cm. The Intermediate Silicon Layers (ISL) [29] are the outermost silicon subdetector systems, consisting of one layer at a radius of 22 cm in the central region and two layers at radii 20 and 28 cm in the forward regions. Surrounding the silicon detector is the Central Outer Tracker (COT) [30], a 3.1 m-long cylindrical open-cell drift chamber covering radii from 43.4 to 132.3 cm.

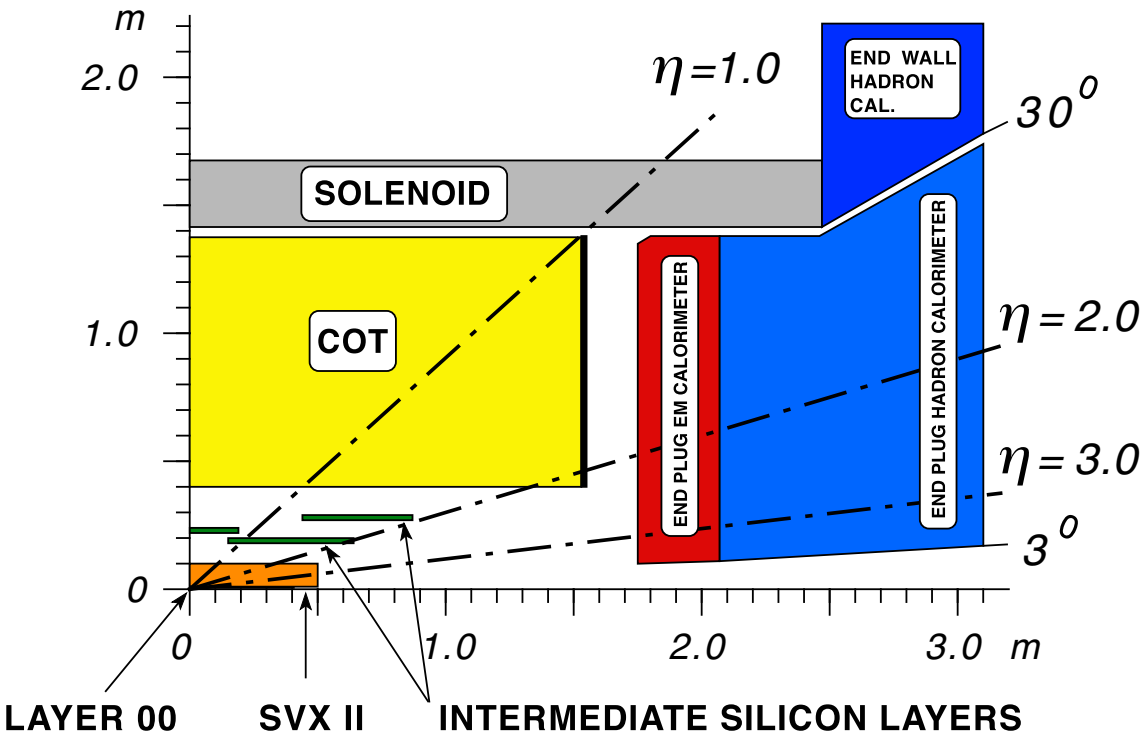

Figure 2.3: The CDF II tracker layout showing the different subdetector systems.

2.4.1 Silicon Tracking Detectors

Silicon tracking detectors are used to obtain precise position measurements of the path of a charged particle. A silicon tracking detector is fundamentally a reverse-biased p-n junction. When a charged particle passes through the detector material, it causes ionization. In the case of a semiconductor material, this means that electron-hole pairs will be produced. Electrons drift towards the anode, and holes drift toward the cathode, where the charge is gathered. The amount of charge is, to first order, proportional to the path length traversed in the detector material by the charged particle.

By segmenting the p or n side of the junction into "strips" and reading out the charge deposition separately on every strip, we obtain sensitivity to the position of the charged particle. All the CDF II silicon tracking detectors are implemented as microstrip detectors. The typical distance between two strips is about 60 μm. Charge deposition from a single particle passing through the silicon sensor will be read out on one or more strips. This charge deposition is called a "cluster."

property	Layer 0	Layer 1	Layer 2	Layer 3	Layer 4
number of ϕ strips	256	384	640	768	869
number of z strips	256	576	640	512	869
stereo angle	90°	90°	+1.2°	90°	-1.2°
ϕ strip pitch $[\mu\mathrm{m}]$	60	62	60	60	65
z strip pitch $[\mu\mathrm{m}]$	141	125.5	60	141	65
active width $[\,\mathrm{mm}]$	15.30	23.75	38.34	46.02	58.18
active length$[\,\mathrm{mm}]$	72.43	72.43	72.38	72.43	72.43

Table 2.2: Relevant parameters for the layout of the sensors of the SVX-II layers.

There are two types of microstrip detectors: single and double-sided. In single-sided detectors only one side (p-n junction) is segmented into strips. Double-sided detectors have both sides (p-n junction and n-n ohmic) segmented into strips. The benefit of double-sided detectors is that while one (p) side has strips parallel to the z direction, providing $r-\phi$ position measurements, the other (n) side can have strips at an angle (stereo angle) with respect to the z direction, which will give z position information.

The innermost layer, L00, is made of single-sided silicon sensors which only provide $r-\phi$ measurements. The SVX-II and ISL are made of double-sided silicon sensors. The ISL detector provides small angle ($1.2°$) stereo information. As shown in Table 2.2, the SVX-II layers have different stereo angles. Two layers have a $1.2°$ stereo angle and three have a $90°$ stereo angle. Four silicon sensors are stacked length-wise into a "ladder" structure which is $29\ \mathrm{cm}$ long. The readout electronics are mounted onto the ends of the ladders. The ladders are organized in an approximately cylindrical configuration, creating "barrels". A SVX-II barrel is segmented into 12 wedges, each covering approximately $30°$ in ϕ with a small overlap at the edges, allowing for several silicon hits per track. There are three SVX-II barrels, adjacent to each other along the z-axis, covering the nominal interaction point in the center of the CDF II Detector. The coverage of the silicon detector subsystems is shown in Figure 2.4. The silicon tracking system is used in stand-alone mode to provide an extension of tracking down to 2.8 in pseudorapidity.

2.4.2 Central Outer Tracker

The COT drift chamber provides accurate information in the $r-\phi$ plane for the measurement of transverse momentum, and substantially less accurate information in the $r-z$ plane for the measurement of the z component of the momentum, p_z. The COT contains 96 sense wire layers, which are radially grouped into eight "superlayers", as inferred from the end plate section shown in Figure 2.5. Each superlayer is divided in ϕ into "supercells," and each supercell has 12 sense wires and a maximum drift distance that is approximately the same for all superlayers. Therefore, the number of supercells in a given superlayer scales approximately with the radius of the superlayer. The entire COT contains 30,240 sense wires. Approximately half the wires run along the z direction ("axial"). The other half are strung at a small angle ($\pm 2°$) with respect to the z direction

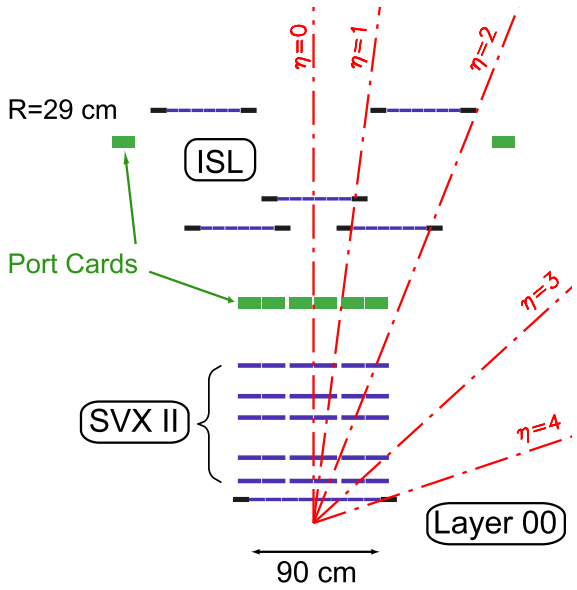

Figure 2.4: Coverage of the different silicon subdetectors projected into the $r-z$ plane. The r and z axes have different scales.

("stereo").

The active volume of the COT begins at a radius of 43.4 cm from the nominal beamline and extends out to a radius of 132.3 cm. The chamber is 310 cm long. Particles originating from the detector origin and interaction point which have $|\eta| < 1$ pass through all 8 superlayers of the COT. Particles which have $|\eta| < 1.3$ pass through 4 or more superlayers.

The supercell layout, shown in Figure 2.6 for superlayer 2, consists of a wire plane containing sense and potential (for field shaping) wires and a field (or cathode) sheet on either side. Both the sense and potential wires are 40 μm diameter gold plated tungsten. The field sheet is 6.35 μm thick Mylar with vapor-deposited gold on both sides. Each field sheet is shared with the neighboring supercell.

The COT is filled with an Argon-Ethane gas mixture and Isopropyl alcohol (49.5:49.5:1). The mixture is chosen to have a constant drift velocity across the cell width. When a charged particle passes through, the gas is ionized. Electrons drift towards the sense wires. The electric field in a cylindrical system grows exponentially with decreasing radius. As a result, the electric field very close to the sense wire is large, resulting in an avalanche discharge when the charge drifts close to the wire surface. This effect provides a gain of $\sim 10^4$. The maximum electron drift time is approximately 100 ns. Due to the magnetic field that the COT is immersed in, electrons drift at a Lorentz angle of $\sim 35°$. The supercell is tilted by $35°$ with respect to the radial direction to compensate for this effect.

Signals on the sense wires are processed by the ASDQ (Amplifier, Shaper, Discriminator with charge encoding) chip, which provides input protection, amplification, pulse shaping, baseline restoration, discrimination and charge measurement [31]. The charge measurement is encoded in the width of the discriminator output pulse, and is used for particle identification by measuring the

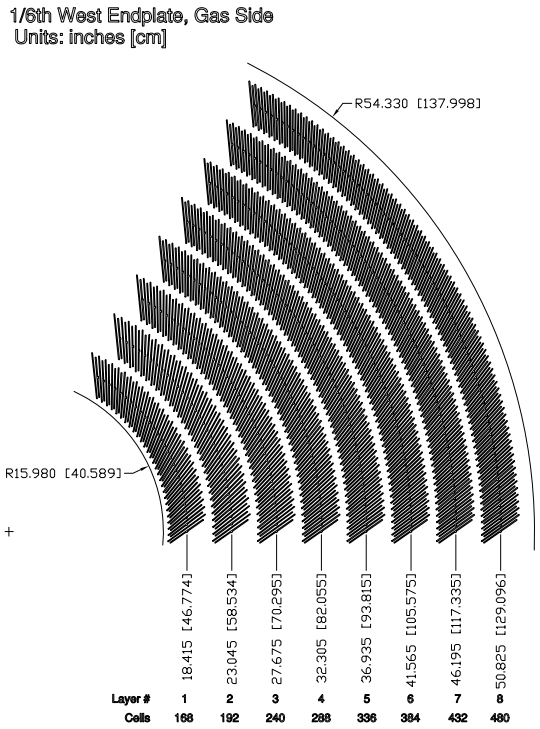

Figure 2.5: Layout of wire planes on a COT endplate.

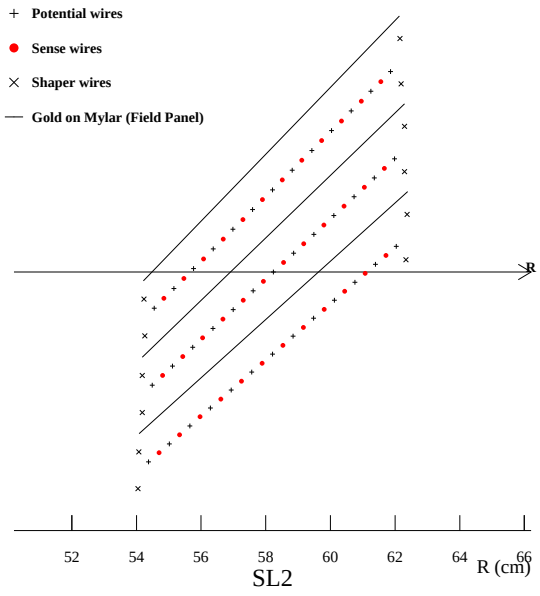

Figure 2.6: Layout of wires in a COT supercell.

ionization along the trail of the charged particle (dE/dx). The pulse is sent through ~ 11 m of micro-coaxial cable, via repeater cards to Time to Digital Converter (TDC) boards in the collision hall. Hit times are later processed by pattern recognition (tracking) software to form helical tracks. The hit resolution of the COT is about $140\ \mu\mathrm{m}$. The transverse momentum resolution has been measured using cosmic ray events to be

$$\frac{\sigma_{p_T}}{p_T^2} = 0.0017\ [\mathrm{GeV}/c]^{-1}. \tag{2.4}$$

2.4.3 Pattern Recognition Algorithms

As explained in the previous sections, charged particles leave small charge depositions as they pass through the tracking system. By following, or "tracking," these depositions, pattern recognition algorithms can reconstruct the charged particle track.

There are several pattern recognition algorithms used to reconstruct tracks in the CDF II tracking system. Most of the tracks are reconstructed using "Outside-In" algorithms which we will describe here. The name of this group of algorithms suggests that the track is followed from the outside of the tracking system inwards.

The track is first reconstructed using only COT information. The COT electronics report hit time and integrated charge for every wire in an event. The hit time corresponds to the time that an avalanche occurred at a sense wire. The hit time can be interpreted as the drift time of the charge in the gas, but first it has to be corrected for time of flight. The hit timing resolution is of the order of a few ns; this roughly corresponds to the average spread in collision times. It is assumed that the collision times always happen at the same time in a cycle during a store. An average of collision times is done for many previous events and this is used as the event collision time. Hit times corrected for the collision time are interpreted as drift times and used in pattern recognition. To perform the final track fit, an additional time of flight correction is performed assuming massless particles.

The helical track, when projected into the two dimensional $r-\phi$ plane, is a circle. This simplifies pattern recognition, so the first step of pattern recognition in the COT looks for circular paths in radial superlayers of the COT. Supercells in the radial superlayers are searched for sets of 4 or more hits that can be fit to a straight line. These sets are called "segments." The straight-line fit for a segment gives sufficient information to extrapolate rough measurements of curvature and ϕ_0. Once segments are found, there are two approaches to track finding. One approach is to link together segments for which the measurements of curvature and ϕ_0 are consistent. The other approach is to improve the curvature and ϕ_0 measurement of a segment reconstructed in superlayer 8 by constraining its circular fit to the beamline, and then adding hits which are consistent with this path. Once a circular path is found in the $r-\phi$ plane, segments and hits in the stereo superlayers are added by their proximity to the circular fit. This results in a three-dimensional track fit. Typically, if one algorithm fails to reconstruct a track, the other algorithm will not. This results in a high track reconstruction efficiency ($\sim 95\%$) in the COT for tracks which pass through all 8 superlayers ($p_T \geq 400\ \mathrm{MeV}/c$). The track reconstruction efficiency mostly depends on how

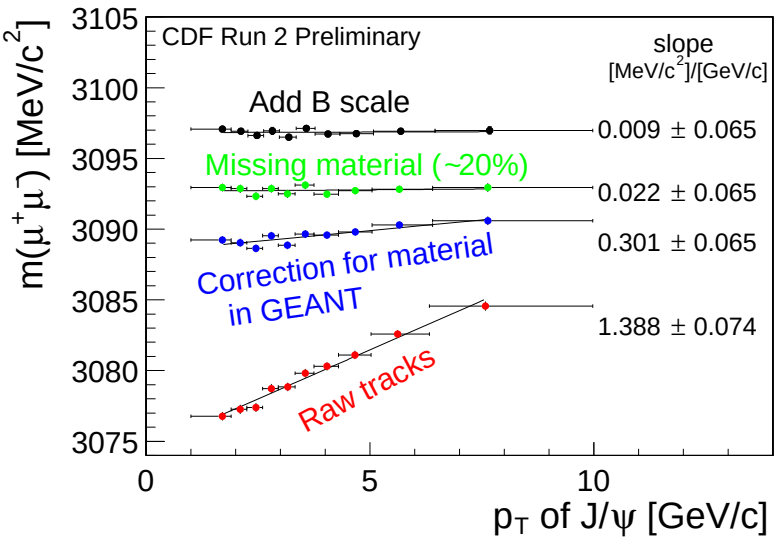

Figure 2.7: Dependence of the reconstructed invariant mass of $J/\psi \to \mu^+\mu^-$ decays on the p_T of the J/ψ.

many tracks there are to be reconstructed in the event. If there are many tracks present close to each other, hits from one track can shadow hits from the other track, resulting in efficiency loss.

Once a track is reconstructed in the COT, it is extrapolated into the SVX-II. Based on the estimated errors on the track parameters, a three-dimensional "road" is formed around the extrapolated track. Starting from the outermost layer, and working inwards, silicon clusters found inside the road are added to the track. As a cluster gets added, the road gets narrowed according to the knowledge of the updated track parameters. Reducing the width of the road reduces the chance of adding a wrong hit to the track, and also reduces computation time. In the first pass of this algorithm, $r-\phi$ clusters are added. In the second pass, clusters with stereo information are added to the track.

2.4.4 Momentum Scale

As the charged particle traverses through the tracker material, it loses energy. For a track that passes through the entire SVX-II volume, the amount of energy loss is roughly 9 MeV. The value is practically independent of the momentum of the particle. In the reconstructed distribution of invariant mass of $J/\psi \to \mu^+\mu^-$ decays, this effect will be more noticeable for low-momentum J/ψ decays than for high-momentum decays. Figure 2.7 illustrates this effect. We use the momentum-dependence of the $\mu^+\mu^-$ invariant mass to calibrate the momentum scale of our detector. The J/ψ mass has to be invariant of transverse momentum and match with the world average [5] value if the momentum scale is correctly calibrated. Our calibration procedure follows two steps. First, the momentum dependence of the J/ψ mass is removed by correctly accounting for the energy loss in the tracker material, and then the overall shift of the J/ψ mass is removed by correcting the value of the magnetic field used in the conversion of curvature into transverse momentum.

There are two types of material in the SVX-II tracker. The silicon sensors are read out and therefore called active material. Everything else in the silicon tracker (readout chips, cards, cables, cooling pipes) is passive material. The energy loss in the active material of the tracking system is taken into account by mapping out the material in the GEANT [32] description of our detector. The passive material in the detector description is not complete, so some energy loss is unaccounted for by this method. An additional layer of material is added to the detector description, to correct for the missing material on average. By tuning the amount of missing material, the momentum dependence of the J/ψ mass is removed. The remaining discrepancy with respect to the PDG average is corrected for by scaling the magnetic field. Because of the implementation of this procedure, we can not use it to measure the J/ψ mass, but the results of the calibration process (the amount of missing material and the corresponding magnetic field) can be used to correct the momentum scale in any other measurement. A more detailed description can be found in [33].

2.5 Time-of-Flight Counter

Outside the tracking system, still inside the superconducting magnetic coil, CDF II has a Time-of-Flight (TOF) [34] system. The TOF system is designed to distinguish low momentum pions, kaons and protons by measuring the time it takes these particles to travel from the primary vertex of the $p\bar{p}$ collision to the TOF system. The system consists of 216 bars of scintillating material, roughly $300\ \mathrm{cm}$ in length and with a cross section of $4 \times 4\ \mathrm{cm}$. The bars are arranged into a barrel around the COT cylinder. They are surrounded by the superconducting solenoid on the outside. Particles passing through the scintillating material of the bars deposit energy causing small flashes of visible light. This light is detected by photomultiplier (PMT) tubes which are attached at both ends of each bar. The signal from the photomultiplier tube is processed by a pre-amplifier circuit mounted directly onto the tube. The amplified signal is sent via a twisted pair to the readout electronics in the collision hall. The readout electronics perform both time and amplitude digitization of the signal. The TDC information is a digitization of the time when the signal pulse reaches a fixed discriminator threshold. This time depends on the amplitude of the pulse, since a large pulse crosses the threshold earlier (time walk). The digitization of the pulse amplitude is needed to correct for this effect. After correcting for time walk effects, the timing resolution of the TOF system is currently about 110 ps for particles crossing the bar exactly in front of one of the photomultiplier tubes. The timing resolution varies with displacement from the photomultiplier tube. Large pulses give better timing resolution, and light attenuates while traveling through the scintillator material. Therefore, particles passing through the bar near the photomultiplier tube have better timing resolution than those which are farther away.

2.6 Calorimeters

The main effort of the Run II upgrade of the CDF II central calorimeter system dealt with upgrading the electronics to handle the faster bunch crossings. The active detector parts were taken over from Run I without modification. The plug calorimeter system was completely re-designed and

system	η coverage	energy resolution (%)	thickness
CEM	$\lvert\eta\rvert < 1.1$	$13.5/\sqrt{E_T} \oplus 3$	$18X_0$
PEM	$1.1 < \lvert\eta\rvert < 3.5$	$16/\sqrt{E} \oplus 1$	$21X_0$
CHA	$\lvert\eta\rvert < 0.9$	$50/\sqrt{E_T} \oplus 3$	$4.5\lambda_0$
WHA	$0.7 < \lvert\eta\rvert < 1.3$	$75/\sqrt{E_T} \oplus 4$	$4.5\lambda_0$
PHA	$1.3 < \lvert\eta\rvert < 3.5$	$80/\sqrt{E} \oplus 5$	$7\lambda_0$

Table 2.3: Pseudorapidity coverage, energy resolution and thickness for the different calorimeter subdetectors of the CDF II Detector. The $\oplus$ symbol means that the constant term is added in quadrature to the resolution. λ_0 signifies interaction lengths and X_0 radiation lengths.

constructed. This system will be described briefly. A detailed description can be found in the CDF II Technical Design Report [26].

The CDF II calorimeter has a "projective tower" geometry. This means that it is segmented in η and ϕ "towers" that point to the interaction region. The coverage of the calorimetry system is 2π in ϕ and $|\eta| < 4.2$ in pseudorapidity. The calorimeter system is divided into three regions: central, plug and forward. Corresponding to these regions, the subsystems will have one of the letters C and P in their acronym. Each calorimeter tower consists of an electromagnetic shower counter followed by a hadron calorimeter. This allows for comparison of the electromagnetic and hadronic energies deposited in each tower, and therefore separation of electrons and photons from hadrons.

There are two subdetectors for the electromagnetic calorimeter: CEM and PEM. These correspond to the central and plug regions of $|\eta|$, respectively. These calorimeters use lead sheets interspersed with scintillator as the active detector medium. The hadron calorimeters in the central region are the central (CHA) and the endwall (WHA). The plug region is covered by the PHA calorimeter. These calorimeters are composed of alternating layers of iron and scintillator. The pseudorapidity coverage, resolutions and thickness for the different electromagnetic and hadron calorimeters are given in Table 2.3.

2.7 Muon Systems

Muons are particles which interact with matter only by ionization. For energies relevant to this experiment, they do not cause showers in the electromagnetic or hadronic calorimeters. As a result, if a muon is created in the collision and has enough momentum, it will pass through the calorimeter with minimal interaction with the material inside. Therefore, the calorimeter can be considered as a filter which retains particles that shower when interacting with matter and muons, which do not. Muon detection systems are therefore placed radially outside the calorimeters.

The CDF II Detector has four muon systems: the Central Muon Detector (CMU), the Central Muon Upgrade Detector (CMP), the Central Muon Extension Detector (CMX), and the Intermediate Muon Detector (IMU) [35]. The CMU detector is made of drift cells, and the CMP, CMX

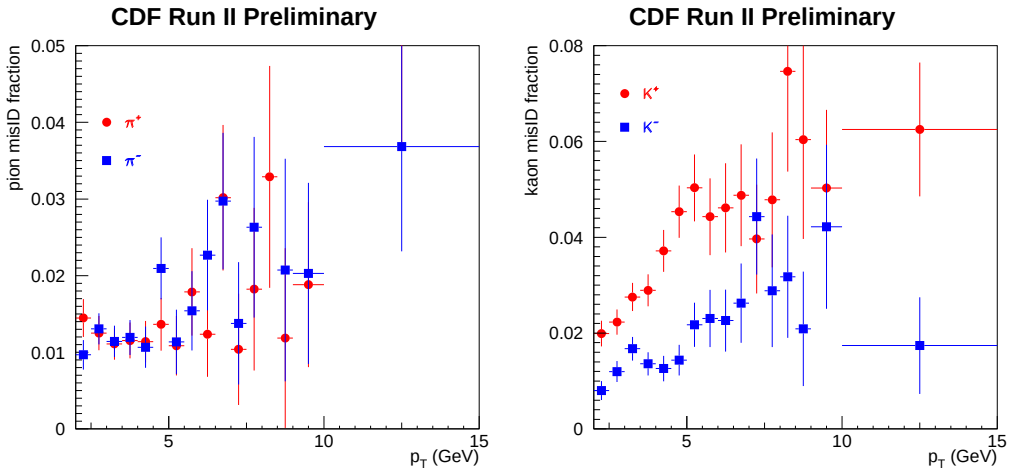

Figure 2.8: Rate of kaon and pion tracks faking muon signals in the CDF II Detector. Roughly 1% of all pions (left) and $2-4\%$ of all kaons (right) will fake a muon signal.

detectors are made of drift cells and scintillation counters, which are used to reject background based on timing information. Using the timing information from the drift cells of the muon systems, short tracks (called "stubs") are reconstructed. Tracks reconstructed in the COT are extrapolated to the muon systems. Based on the projected track trajectory in the muon system, the estimated errors on the tracking parameters and the position of the muon stub, a χ^2 value of the track-stub match is computed. To ensure good quality of muons, an upper limit is placed on the value of χ^2_ϕ, the χ^2 of the track-stub match in the ϕ coordinate.

Most of the particles that pass through the calorimeter without showering are muons, but it is also possible for pions or kaons to survive the passage. These particles can then fake muon signals in the muon chambers. Typically, these fake rates are at the percent level, as seen in Figure 2.8 for the CMU and CMP detectors combined. The Figure 2.8 shows the rate at which charged pions and kaons fake muon signals in the muon systems. The difference between K^+ and K^- rates comes from the different cross section for interaction of these two mesons with the calorimeter material. The different interaction cross section for these two mesons comes from their quark content: in the K^+, the strange quark is the antiquark.

2.8 Trigger System

Triggering systems are necessary because it is not physically possible to store information about every single $p\bar{p}$ collision. Collisions happen roughly at a rate of 2.5 MHz, and the readout of the full detector produces an event roughly the size of 250 kB. There is no medium available which is capable of recording data this quickly, nor would it be practical to analyze all this data later on. The trigger system is a pre-filter, which reduces data rates and volumes to manageable levels, according to all possible or foreseen physics prescriptions.

The CDF Ⅱ triggering system is designed based on three conditions. The first condition is that the trigger has to be deadtimeless. This means that the trigger system has to be quick enough to make a decision for every single event, before the next event occurs. The condition is imposed by the Tevatron upgrade for Run Ⅱ, and it is the time between collisions, 396 ns. The second condition is that the data logging system can write about 30-50 events per second to tape, because of limited resources. In short, the trigger has to be fast enough to analyze every collision, and it has to figure out which 50 of 2.5 million events it should save in a given second. This is achieved by staging trigger decisions in three levels, as shown in Figure 2.9.

Each level of the trigger is given a certain amount of time to reach a decision about accepting or rejecting an event. By increasing the time allowed for triggering at different levels of the trigger, the complexity of reconstruction tasks can be increased at every level. At the first level of the trigger, only very rough and quick pattern recognition and filtering algorithms are used. In order to do this in time, the Level 1 and Level 2 triggering mechanisms are implemented with custom electronics. The third level of the trigger is implemented with a PC farm with about 300 CPUs. Using each CPU as an event buffer allows for nearly one second to be allocated for the trigger decision. As a result, nearly offline quality of event reconstruction is available at the third level of triggering. The Level 3 rejection rate is about 10, resulting in 30 events/sec being accepted by the Level 3 trigger and written to tape.

The delay necessary to make a trigger decision is achieved by storing detector readout information in a storage pipeline. At Level 1, for every Tevatron clock cycle, the event is moved up one slot in the pipeline. By the time it reaches the end of the pipeline, the trigger will have reached a decision whether to accept or reject this event. If the event is accepted, its information will be sent to the higher level of the trigger. Otherwise, the event is simply ignored. Since the Level 1 takes up to about $5\ \mu$s to reach an accept/reject decision, the front-end electronics is equipped with a 14-event deep buffer to accommodate new events while the Level 1 decision is taken. The accept rate is less than 50 kHz, much smaller than the total input rate of 2.5 MHz. The rejection factor after Level 1 is about 150. The Level 2 trigger takes more time and adds more information to take a further decision about the event. The Level 2 trigger hardware takes less than $30\ \mu$s to make the global decision, and with implementation of a set of 4 event buffers the total accept rate is below 300 Hz.

A set of requirements that an event has to fulfill at Level 1, Level 2 and Level 3 constitutes a trigger path. Requiring that an event be accepted through a well defined trigger path eliminates volunteer events. The CDF Ⅱ trigger system implements about 100 trigger paths. An event will be accepted if it passes the requirements of any one of these paths.

In this thesis three trigger paths have been used, which will be described in detail.

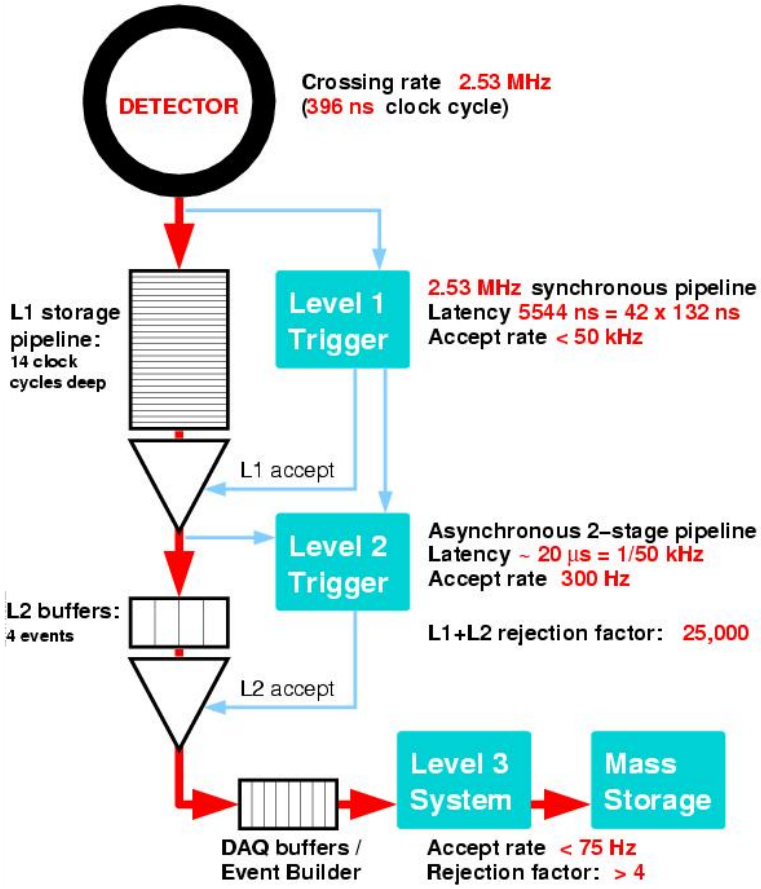

Figure 2.9: Schematic diagram of the CDF global Trigger system.

Chapter 3

Event Selection

3.1 Search Signature

We search for VLQ3 pair production events with VLQ3 decaying into $\tau^- + \overline{b}$, when we assume $\beta = 1$. Therefore the final state contains two taus and two b quarks. The signature we search for is one tau decaying leptonically to an electron or muon, one tau decaying hadronically to two jets. This combination of $\tau_e^{\pm}\tau_h^{\mp}b\overline{b}$ or $\tau_\mu^{\pm}\tau_h^{\mp}b\overline{b}$ represents 46% of the possible $\tau\tau$ decay variations.

For $\tau_e^{\pm}\tau_h^{\mp}b\overline{b}$ channel, we use the central electron and $E_T > 10$ GeV and central hadronic τ with $E_T > 15$ GeV, plus two jets from $b\overline{b}$. For $\tau_\mu^{\pm}\tau_h^{\mp}b\overline{b}$ channel, we use the muon detected in CMU and CMP (such muons are called CMUP muons) or in CMX detector, with $p_T > 10$ GeV/c and central hadronic τ with $E_T > 15$ GeV, plus two jets from $b\overline{b}$.

3.2 Data Sample

This analysis uses $322\,\text{pb}^{-1}$ of data collected using the *Lepton+Track* triggers, and in particular the trigger paths `TAU_CEM8_TRACK5`, `TAU_CMUP8_TRACK5`, and `TAU_CMX8_TRACK5`. The Level 1 trigger requirements for these paths are a CEM electron with $E_T > 8$ GeV, a CMUP muon with a matching XFT track of $p_T \geq 8$ GeV/c, or a CMX muon with a matching XFT track of $p_T \geq 8$ GeV/c, respectively. For the CEM path, some of the later data includes an additional requirement at Level 2 of a second XFT track, with $p_T \geq 5$ GeV/c, separated from the primary electron candidate by at least 10 degrees in ϕ. The Level 3 trigger requires an electron (muon) with $E_T \geq 8$ GeV ($p_T \geq 8$ GeV/c), plus a track of $p_T \geq 5$ GeV/c with what is called *tau-like* isolation, which means there are no $p_T \geq 1.5$ GeV/c tracks in an annulus of $0.17 < \Delta R = \sqrt{(\Delta\eta)^2 + (\Delta\phi)^2} < 0.52$ around the primary track. Detailed requirements of the trigger paths are listed in Table 3.1, 3.2 and 3.3.

Table 3.1: Requirements of the TAU_CEM8_TRACK5 trigger path used to collect data for this analysis.

Trigger	Requirement
Level 1	
L1_CEM8_PT8	Seed Tower $E_T > 8$ GeV in CEM
	$E_{\rm had}/E_{\rm em} < 0.125$ if $E_T < 16$ GeV
	3 or 4 layer XFT track w/$p_T > 8$ GeV/c
	pointing to seed.
Level 2	
L2_CEM8_PT8	Cluster $E_T > 8$ GeV in CEM
	Shoulder $E_T > 7.5$ GeV
	$E_{\rm had}/E_{\rm em} < 0.125$
	4 layer XFT track w/$p_T > 8$ GeV/c
	pinting to seed
L2_CEM8_PT8_CES3	Same as L2_CEM8_PT8
	CES $E > 3.0$ GeV
L2_CEM8_PT8_CES3_TRK5_DPHI10	Same as L2_CEM8_PT8_CES3
	Second 4 layer XFT track with $p_T > 5.0$ GeV/c
	Angle between two tracks $> 10^{\circ}$
Level 3	
L3_ELE8_TRK5_ISO	
Electron	$E_T > 8$ GeV ($z_0 = 0$)
	$p_T > 8$ GeV/c
	$\lvert\Delta z\rvert < 8$ cm
	$\chi^2_{\rm strip} < 20$
Isolated Track	$p_T > 5.0$ GeV/c
	$\lvert\eta\rvert < 1.5$
	No tracks w/$p_T > 1.5$ GeV/c, and $\lvert\Delta z_0\rvert < 15$ cm
	in $0.175 < \Delta R < 0.524$ of "Isolated Track"
Event Level	$\lvert z_0(e) - z_0({\rm trk})\rvert < 15$ cm
	$\Delta R(e, {\rm trk}) > 0.175$

Table 3.2: Requirements of the TAU_CEM8_TRACK5 trigger path used to collect data for this analysis.

Trigger	Requirement
Level 1	
L1_CMUP6_PT4	CMU stub $p_T \geq 6\ \mathrm{GeV}/c$
	CMP stub $p_T > 3\ \mathrm{GeV}/c$
	Number of CMP hit layers > 2
	4 layer XFT track w/$p_T > 4\ \mathrm{GeV}/c$
Level 2	
L2_AUTO_L1_CMUP6_PT4	Auto accept
L2_TRK8_L1_CMUP6_PT4	XFT $p_T > 8\ \mathrm{GeV}/c$
Level 3	
L3_CMUP8_TRACK5_ISO	
Muon	$p_T \geq 8\ \mathrm{GeV}/c$
	$\lvert\Delta x\rvert_{\mathrm{CMU}} < 15.0\ \mathrm{cm}$
	$\lvert\Delta x\rvert_{\mathrm{CMP}} < 20.0\ \mathrm{cm}$
Isolated Track	$p_T > 5.0\ \mathrm{GeV}/c$
	$\lvert\eta\rvert < 1.5$
	No tracks w/$p_T > 1.5\ \mathrm{GeV}/c$, and $\lvert\Delta z_0\rvert < 15\ \mathrm{cm}$
	in $0.175 < \Delta R < 0.524$ of "Isolated Track"
Event Level	$\lvert z_0(e) - z_0(\mathrm{trk})\rvert < 15\ \mathrm{cm}$
	$\Delta R(e, \mathrm{trk}) > 0.175$

Table 3.3: Requirements of the TAU_CMX8_TRACK5 trigger path used to collect data for this analysis.

Trigger	Requirement
Level 1	
L1_CMX6_PT8	CMX stub $p_T \geq 6\ \mathrm{GeV}/c$
	4 layer XFT track w/$p_T > 8\ \mathrm{GeV}/c$
L1_CMX6_PT8_CSX	Same as L1_CMX6_PT8
	CSX required
Level 2	
L2_AUTO_L1_CMX6_PT8	Auto accept
L2_AUTO_L1_CMX6_PT8_CSX	Auto accept
Level 3	
L3_CMX8_TRACK5_ISO	
Muon	$p_T \geq 8\ \mathrm{GeV}/c$
	$\lvert\Delta x\rvert_{\mathrm{CMX}} < 30.0\ \mathrm{cm}$
Isolated Track	$p_T > 5.0\ \mathrm{GeV}/c$
	$\lvert\eta\rvert < 1.5$
	No tracks w/$p_T > 1.5\ \mathrm{GeV}/c$, and $\lvert\Delta z_0\rvert < 15\ \mathrm{cm}$
	in $0.175 < \Delta R < 0.524$ of "Isolated Track"
Event Level	$\lvert z_0(e) - z_0(\mathrm{trk})\rvert < 15\ \mathrm{cm}$
	$\Delta R(e, \mathrm{trk}) > 0.175$

3.3 Particle Identification

In this section, we give the requirements placed on the individual particle candidates (for hadronic taus, electrons, muons, and jets). First, we detail the geometrical and kinematic requirements that guarantee a well understood detector acceptance for the candidates. Second, we describe the specifics of additional particle separation and identification (ID) requirements. There are also requirements on the level of isolation of the candidates. Also, the trigger efficiencies for each particle type are reported.

The total efficiency is factorized as follows:

$$\epsilon = \epsilon_{\rm acc}\,\epsilon_{\ell}\,\epsilon_{\tau}\,\epsilon_{\rm evt}\ , \tag{3.1}$$

where

$$\epsilon_{\rm acc} = \epsilon_{{\rm acc}(\ell)}\,\epsilon_{{\rm acc}(\tau)}\,\epsilon_{{\rm sep}(\ell,\tau)}\ , \tag{3.2}$$

$$\epsilon_{\ell} = \epsilon_{{\rm sep}(\ell,{\rm jet})}\,\epsilon_{{\rm ID}(\ell)}\,\epsilon_{{\rm iso}(\ell)}\,\epsilon_{{\rm trig}(\ell)}\ , \tag{3.3}$$

$$\epsilon_{\tau} = \epsilon_{{\rm sep}(\tau,{\rm jet})}\,\epsilon_{{\rm ID}(\tau)}\,\epsilon_{{\rm iso}(\tau)}\,\epsilon_{{\rm trig}(\tau)}\ . \tag{3.4}$$

The electron or muon acceptance term $\epsilon_{{\rm acc}(\ell)}$ (Sections 3.3.1 and 3.3.1) and the tau acceptance term $\epsilon_{{\rm acc}(\tau)}$ (section 3.3.1) contain a set of geometric and kinematic requirements. The separation term $\epsilon_{{\rm sep}(\ell,\tau)}$ (Section 3.3.1) is also included in the acceptance portion.

The final term, the event requirement efficiency $\epsilon_{\rm evt}$, is evaluated after all of the acceptance, lepton, and tau requirements, and is discussed in Section 3.4.

The lepton efficiency factors in ϵ_{ℓ} apply to the electron or muon candidates. The term $\epsilon_{{\rm sep}(\ell,{\rm jet})}$ (Section 3.3.2) is calculated with respect to those events passing all of the acceptance requirements. The lepton ID efficiency term $\epsilon_{{\rm ID}(\ell)}$ (Sections 3.3.2 and 3.3.2) is calculated with respect to those events passing the lepton-to-jet separation requirement. The lepton isolation efficiency term $\epsilon_{{\rm iso}(\ell)}$ (Section 3.3.2) is calculated with respect to those events passing the lepton ID requirements.

The tau efficiency term ϵ_{τ} is made up of analogous factors, all of which are evaluated after the electron/muon requirements have been made. The term $\epsilon_{{\rm sep}(\tau,{\rm jet})}$ (Section 3.3.2) is calculated with respect to those events passing all of the above lepton requirements. The tau ID efficiency term $\epsilon_{{\rm ID}(\tau)}$ (Section 3.3.2) is calculated with respect to those events passing the tau-to-jet separation requirement. The tau isolation efficiency term $\epsilon_{{\rm iso}(\tau)}$ (Section 3.3.2) is calculated with respect to those events passing the tau ID requirements.

The Monte Carlo simulation (MC) that is used for the measurement of the acceptance and ID requirements, with corrections applied where needed, is performed such that each event contains at least one leptonically decaying tau and one hadronically decaying tau, but (for technical reasons) with no constraint on where those taus come from. Therefore, prior to being considered for the acceptance requirements, the HEPG (Monte Carlo generator-level) information is used to verify that each event has the proper structure of one LQ decaying to $\tau_{\ell} b$ and the other decaying to $\tau_h b$.

3.3.1 Geometrical and Kinematic Acceptance

To avoid the effect of mis-identification, prior to the application of the acceptance requirements, the candidate particles must match a corresponding particle in the HEPG bank. The requirement used is $\sqrt{(\Delta\theta)^2 + (\Delta\phi)^2} < 0.2$, where the angles are between the reconstructed candidate object and the HEPG object. Mis-identified particles are rare after all of the ID requirements, but to measure the efficiencies of the acceptance and separation requirements accurately, *before* the ID requirements are applied, this HEPG matching is applied.

Electron Acceptance

The acceptance requirements for the electron candidate are given in the following list and the efficiencies for $m_{\mathrm{LQ3}} = 320\ \mathrm{GeV}/c^2$ (the acceptance efficiencies depend on the mass of the leptoquark) are given in Table 3.4. All reconstructed objects of electron type (CdfEmObject) that pass these requirements are considered.

- Central (presence of a bit corresponding to the CEM)
- $E_T^{\mathrm{corr}} > 10\ \mathrm{GeV}$ (corrected energy)
- $p_T > 8\ \mathrm{GeV}/c$
- $|z_0| < 60\ \mathrm{cm}$
- Fiducial requirements:

  Fiducial in the ShowerMax: $|x_{\mathrm{CES}}| < 21.5\ \mathrm{cm}$ and $9 < |z_{\mathrm{CES}}| < 230\ \mathrm{cm}$
  Fiducial in the COT: $|z_{\mathrm{COT}}| < 150\ \mathrm{cm}$ at a radius of $R_{\mathrm{COT}} = 137\ \mathrm{cm}$

Muon Acceptance

The acceptance requirements for the muon candidate are given in the following list and the efficiencies are given in Table 3.4. All reconstructed objects of muon type (CdfMuon) that pass these requirements are considered.

- Presence of, and classification based upon, CMUP or CMX bit
- $p_T > 10\ \mathrm{GeV}/c$
- $|z_0| < 60\ \mathrm{cm}$
- Fiducial requirements:

  Fiducial in the CMUP or CMX
  Fiducial in the COT: $|z_{\mathrm{COT}}| < 150\ \mathrm{cm}$ at a radius of $R_{\mathrm{COT}} = 137\ \mathrm{cm}$

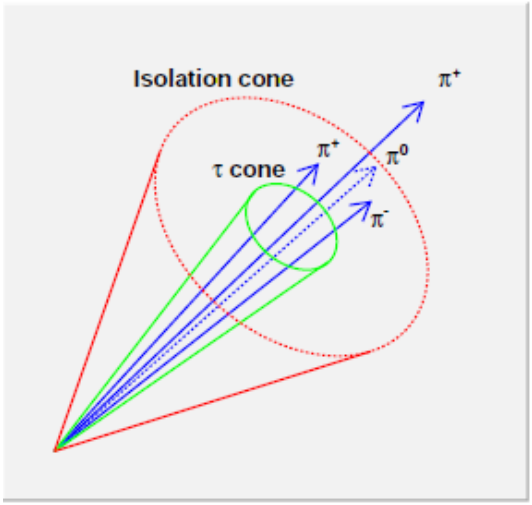

Figure 3.1: A hadronic tau decay wich three charged pions and a neutral pion localized to a relatively small solid angle. The green cone is able to shrink.

Hadronic Tau Acceptance

The acceptance requirements for the hadronic tau candidate are given in the following list and the efficiencies are given in Table 3.4. All reconstructed objects of tau type (CdfTau) that pass these requirements are considered.

In Run II, tau analysis are using a "shrinking cone" to define the localization of the tau. The rationale is that, as tuas become more boosted, their decay daughters should become more collinear in the lab frame. The cone-size adjusts according to the following formula:

$$\alpha_{\rm trk} = min[0.175, max(5 \ \ {\rm GeV}/E^{\rm cal}, 0.05)] \tag{3.5}$$

where $E^{\rm cal}$ is the energy in GeV of the calorimeter cluster associated with the tau candidate, and all other units are in radians. The minimal cone size corresponds to 2.9°, and applies to tau with energies above 100 GeV. The shrinking cone is shown in Figure 3.1.

- $|\eta_{\rm det}| < 1.0$ (detector η)
- $E_T^{\rm corr} > 15$ GeV (corrected energy)
- $p_T^{\rm seedtrk} > 6$ GeV/c
- Fiducial requirements:

  Seed track fiducial in the ShowerMax: $9 < z_{\rm CES}^{\rm seedtrk} < 230$ cm
  Seed track fiducial in the COT: $|z_{\rm COT}^{\rm seedtrk}| < 150$ cm at a radius of $R_{\rm COT} = 137$ cm

Lepton-Tau Separation

A lepton-tau separation requirement is placed after the above acceptance criteria. The requirement is given here (throughout this document, the symbol ℓ refers to either an electron or a muon) and the resulting efficiency is included in Table 3.4. For the purpose of this separation requirement, we use the direction of the visible momentum of the tau candidate (sum of momentum of tracks and π^0s within tau cones).

- $\Delta R(\tau_h, \ell) > 0.7$

Scale Factors and Total Acceptance

The total acceptance is the combination of the acceptance of the lepton candidate, the acceptance of the τ_h candidate, and the $\ell - \tau_h$ separation. The totals for the muon channels are corrected by a scale factor that compensates for differences in the stub finding efficiencies between MC and data. From reference [37], these scale factors are $f^{\rm acc}_{\rm CMUP} = 0.941 \pm 0.008$ and $f^{\rm acc}_{\rm CMX} = 0.987 \pm 0.003$, for the CMUP and CMX, respectively. This factor does not include a correction for potential differences between MC and data for the $|z_0| < 60$ cm requirement. However efficiencies for this requirement have been shown to be very similar in MC and data, so this small uncertainty is negligible compared to others. Also, note that while the above scale factors were derived from higher p_T muons, there should be nothing in the muon reconstruction that is momentum dependent for $p_T > 10$ GeV/c, and if we are missing some small effect, the impact will be further reduced by the fact that only $10-15\%$ of leptons from leptoquarks have $p_T < 20$ GeV/c. So, for example, a 2.5% effect would enter as a contribution of 0.3% to the final scale factor. Such an effect would be small compared to the other systematics that are included (and discussed in the following).

A systematic uncertainty is applied to the total acceptance for each channel. This uncertainty is obtained by the studies in references [38] and [39]. For the $e\tau_h$ channel, an uncertainty of 1.5% comes from two dominant sources: track reconstruction contributes 1.4% and material uncertainty contributes 0.4%. The track reconstruction component includes 0.4% for the electron, 0.4% for the 1-prong taus, and 3% for the 3-prongs taus, combined in a way that accounts for the ratio of 1-prong and 3-prongs tau decays. The material uncertainty has also been thoroughly studied for the $Z^0 \to \tau^+\tau^-$ cross-section measurement. That study involves using a Monte Carlo sample with an increased amount of material. For the $\mu\tau_h$ channel, without the impact of Bremsstrahlung that exists for the electron channel, the material uncertainty can be reduced. However, the systematic remains close to 1.5%. The uncertainties on the scale factor determinations (0.008 for $f^{\rm acc}_{\rm CMUP}$ and 0.003 for $f^{\rm acc}_{\rm CMX}$) are also included.

There is more discussion of the considered acceptance scale factors. The relevant subsections, which discuss samples used and techniques applied, are titled "Efficiency of $|\Delta Z| < 60$ cm Cut," "Track Reconstruction Efficiency," "Cut on the Number of Towers in a Tau Cluster," "Neutral Pion Reconstruction," and "Calorimeter Energy Scale and Resolution". The last of these contains a discussion of the material uncertainty, which has been superseded by a newer study: as discussed in reference [39], the knowledge of the material is accurate to better than 10% (found from the rate of conversions and tridents in $Z^0 \to e^+e^-$ and $W \to e\nu$). As mentioned above, the associated

Table 3.4: Summary of lepton acceptance, hadronic tau acceptance, lepton-tau separation, scale factors, and the total acceptance for the $e\tau_h$ channel and $\mu\tau_h$ channels, shown for $m_{\mathrm{LQ3}} = 320\ \mathrm{GeV}/c^2$. The details of the acceptance requirements are given in the text.

	$e\tau_h$		$\mu_{\mathrm{CMUP}}\tau_h$	$\mu_{\mathrm{CMX}}\tau_h$
Electron:	Efficiency (%)	Muon:	Efficiency (%)	Efficiency (%)
CdfElectrons	79.6 ± 0.1	CdfMuon	71.7 ± 0.1	71.7 ± 0.1
CEM	85.2 ± 0.1	CMUP/CMX	45.2 ± 0.2	21.5 ± 0.2
$E_T^{\mathrm{corr}} > 10\ \mathrm{GeV}$	88.4 ± 0.1			
$p_T > 8\ \mathrm{GeV}/c$	96.2 ± 0.1	$p_T > 10\ \mathrm{GeV}/c$	92.5 ± 0.2	89.1 ± 0.3
$\lvert z_0 \rvert < 60\ \mathrm{cm}$	97.0 ± 0.1	$\lvert z_0 \rvert < 60\ \mathrm{cm}$	96.9 ± 0.1	96.7 ± 0.2
Fiducial	82.9 ± 0.2	Fiducial	98.0 ± 0.1	68.3 ± 0.4
Subtotal	46.3 ± 0.2		28.4 ± 0.1	9.1 ± 0.1
Tau:				
CdfTau	72.7 ± 0.2		73.3 ± 0.3	72.6 ± 0.5
$\lvert \eta_{\mathrm{det}} \rvert < 1.0$	87.5 ± 0.2		87.8 ± 0.2	87.5 ± 0.4
$E_T^{\mathrm{corr}} > 15\ \mathrm{GeV}$	98.4 ± 0.1		98.6 ± 0.1	98.3 ± 0.2
$p_T^{\mathrm{seedtrk}} > 6\ \mathrm{GeV}/c$	98.9 ± 0.1		99.1 ± 0.1	99.1 ± 0.1
Fiducial	90.4 ± 0.2		90.3 ± 0.2	90.0 ± 0.4
Subtotal	56.0 ± 0.2		56.7 ± 0.3	55.6 ± 0.5
$\Delta R(\tau_h, \ell) > 0.7$	96.7 ± 0.1		96.3 ± 0.2	97.4 ± 0.2
Subtotal	25.1 ± 0.1		15.5 ± 0.1	4.9 ± 0.1
Scale Factor	1.000 ± 0.015		0.941 ± 0.017	0.987 ± 0.015
Total Acceptance	$25.1 \pm 0.1 \pm 0.4$		$14.6 \pm 0.1 \pm 0.2$	$4.8 \pm 0.1 \pm 0.1$

contributing scale factor and uncertainty are determined by comparing the default acceptance with a simulation where the amount of material is changed.

The scale factors and total acceptance efficiencies are shown at the bottom of Table 3.4 for the case of $m_{\mathrm{LQ3}} = 320\ \mathrm{GeV}/c^2$.

3.3.2 Efficiencies of Particle Identification and Trigger

Jets

What follows is a list of requirements placed to identify jets used as candidates for those coming from the b quarks resulting from LQ decays. For this purpose they are simply counted, however, the kinematic distributions are examined as part of the validation of the analysis, and in the future these jets might be used as part of a mass reconstruction technique. These jets are also used for the purpose of correcting missing transverse energy ($\not\!\!E_T$).

- $|\eta_{\rm det}| < 2.4$
- $E_T^{\rm raw} > 10$ GeV
- $E_T^{\rm corr} > 15$ GeV
- $\Delta R(\ell/\tau_h, {\rm jet}) > 0.8$

The jet reconstruction in this analysis employs a cone cluster algorithm with cone radius $\Delta R = 0.4$ [41]. We measure the transverse energy $E_T = Esin\theta$, where θ is the polar angle of the centroid of the cluster towers and calculated using the measured z position of the event vertex. Total energy E is the sum of the energy deposited in calorimeter towers within a cone. The jet energy corrections are up through following 5 steps [42, 43]:

- The η Dependence in Calorimeter Response: Correction to make the calorimeter response uniformed in η by using the di-jet balancing procedure. This is tested by the γ+jet samples in data and Monte Carlo simulation.
- Calorimeter Stability (Time dependence): Correcton for the variation in phototube response due to aging effecs, therefore the correction is applied only to the data sample.
- Multiple Interaction: It is possible to have more than one interaction per collision due to high-luminosity collisions at Tevatron. This correction takes into account them. The correcton is deduced from analyzing the minimum bias data as a function of the number of vertices in the same beam bunch crossing.
- Absolute Energy Scale: this correction accouts for the calorimeter non-linearity, jet fragmentation and underlying event.

Lepton-Jet Separation

The lepton-jet separation requirement removes any leptons (which already passed the acceptance criteria) from further consideration if they are too close to a jet candidate. The criterion is:

- Veto leptons with $0.3 < \Delta R(\ell, {\rm jet}) < 0.8$

The lower edge of this requirement is used to handle the fact that electron (and tau) candidates always have a corresponding jet candidate, in the list of primitive jet objects, that stems from the same original object. We do not want to veto electrons based on combinations with these "shadow" fake jets. The efficiency for the lepton-jet separation requirement is shown in the first line of Table 3.5 for the case of $m_{\rm LQ3} = 320$ GeV/c^2.

Election Identification

The electron ID requirements are listed, and the efficiencies given, in Table 3.6. The track quality requirements are for at least 3 segments in the axial and at least 3 segments in the stereo superlayers of the COT, with at least 5 hits per segment.

Table 3.5: Separation and isolation efficiencies for leptons and taus, evaluated for the case of $m_{\mathrm{LQ3}} = 320\ \mathrm{GeV}/c^2$.

Requirement	$e\tau_h$ Efficiency (%)	$\mu_{\mathrm{CMUP}}\tau_h$ Efficiency (%)	$\mu_{\mathrm{CMX}}\tau_h$ Efficiency (%)
Veto $0.3 < \Delta R(\ell, \mathrm{jet}) < 0.8$	90.3 ± 0.2	88.5 ± 0.3	90.8 ± 0.4
Lepton $I_{\mathrm{trk}}^{\Delta R<0.4} < 2\ \mathrm{GeV}/c$	88.4 ± 0.2	94.9 ± 0.2	95.4 ± 0.3
Veto $0.3 < \Delta R(\tau, \mathrm{jet}) < 0.8$	90.3 ± 0.2	88.5 ± 0.3	90.8 ± 0.4
$N_{\mathrm{trk}}^{\tau\ \Delta\Theta} = 0$ and $N_{\mathrm{trk}}^{\tau\ \Delta R} = 0$	82.3 ± 0.4	82.3 ± 0.5	83.0 ± 0.8
Tau $I_{\pi^0}^{\Delta\Theta} \leq 0.6\ \mathrm{GeV}/c$	96.1 ± 0.2	96.2 ± 0.3	96.2 ± 0.4
Scale Factor	1.00 ± 0.03	1.00 ± 0.03	1.00 ± 0.03

As done in the search for RPV stop [44], we apply a scale factor of $f_{\mathrm{CEM}}^{\mathrm{ID}} = 1.00 \pm 0.01$ to the ID efficiency measured using MC so that it applies to data. This uncertainty takes a weighted combination of the uncertainties from a study [45] at high p_T, with a scale factor of 1.000 ± 0.005, and a study [46] at medium p_T, with a scale factor of 1.000 ± 0.025. First, note that the combined scale factor is 1.00 since the numbers from the two momentum ranges are 1.000. Furthermore, the electrons resulting from LQ decays have $p_T > 20\ \mathrm{GeV}/c$ more than 80% of the time, so that is the fraction used to weight the result taken from the high p_T study. The weighting is calculated as follows: $\sigma = (0.80)0.005 + (0.20)0.025 = 0.009$ to account for 80% of electrons with $p_T > 20\ \mathrm{GeV}/c$ and 20% with $p_T < 20\ \mathrm{GeV}/c$. The 0.009 corresponds to a 0.9% uncertainty. We are slightly conservative in two ways: (1) The electron p_T distribution is such that there are actually more than 80% of electrons with $p_T > 20\ \mathrm{GeV}/c$, which is the region with lower uncertainty on the scale factor, and (2) we use 1.0% instead of 0.9%. So, the quoted electron ID scale factor is 1.00 ± 0.01.

Muon Identification

The muon ID requirements and efficiencies are given in Table 3.7. The track quality requirements are the same as used for the electron ID given in Section 3.3.2.

The efficiency measured using MC is scaled so that it applies to data by using scale factors derived in reference [44], which in turn uses input from reference [37, 47].

Lepton Isolation

The lepton isolation, $I_{\mathrm{trk}}^{\Delta R=0.4}$, is defined as a sum of the p_T of all tracks within a cone of $\Delta R = 0.4$ around the track of the electron or muon candidate. The criterion to have an isolated lepton is:

- $I_{\mathrm{trk}}^{\Delta R<0.4} < 2\ \mathrm{GeV}/c$

The efficiency for the isolation requirement, measured using signal MC, is shown in Table 3.5. The scale factor for the isolation requirement is 1.00, determined by studying the density of tracks

Table 3.6: Electron identification requirements and efficiencies, for the case of $m_{\mathrm{LQ3}} = 320\ \mathrm{GeV}/c^2$. The details of the track quality requirement are given in the text.

Requirement	Efficiency (%)
Track Quality	99.9 ± 0.0
$E_{\mathrm{had}}/E_{\mathrm{em}} < 0.055 + 0.00045 * E$	98.4 ± 0.1
$E_T^{\mathrm{corr}}/p_T < 2.0$ for $E_T^{\mathrm{corr}} < 50\ \mathrm{GeV}$	90.2 ± 0.2
$-3.0 < Q * \Delta x_{\mathrm{CES}} < 1.5\ \mathrm{cm}$	98.9 ± 0.1
$\lvert\Delta z_{\mathrm{CES}}\rvert < 3\ \mathrm{cm}$	99.6 ± 0.1
$\chi^2_{z\ \mathrm{CES}} < 10$	96.4 ± 0.1
$\mathrm{L_{shr}} < 0.2$	98.4 ± 0.1
$d_0 < 0.2\ \mathrm{cm}$	99.5 ± 0.1
Subtotal	82.4 ± 0.3
Scale Factor	1.00 ± 0.01
Total ID Efficiency	$82.4 \pm 0.3 \pm 0.8$

Table 3.7: Muon identification requirements and efficiencies, for the case of $m_{\mathrm{LQ3}} = 320\ \mathrm{GeV}/c^2$. The details of the track quality requirement are given in the text.

Requirement	CMUP muons Efficiency (%)	CMX muons Efficiency (%)
Track Quality	100.0 ± 0.0	100.0 ± 0.0
$E_{\mathrm{em}} < 2\ \mathrm{GeV}$ and $E_{\mathrm{had}} < 6\ \mathrm{GeV}$	91.6 ± 0.2	91.5 ± 0.4
$d_0 < 0.2\ \mathrm{cm}$	99.9 ± 0.0	99.9 ± 0.1
($\Delta x_{\mathrm{CMU}} < 4$ and $\Delta x_{\mathrm{CMP}} < 7$) or $\Delta x_{\mathrm{CMX}} < 6\ \mathrm{cm}$	99.1 ± 0.1	99.2 ± 0.1
Subtotal	90.7 ± 0.3	90.6 ± 0.4
Scale Factor	0.939 ± 0.030	0.990 ± 0.003
Total ID Efficiency	$85.2 \pm 0.3 \pm 2.7$	$89.7 \pm 0.4 \pm 0.3$

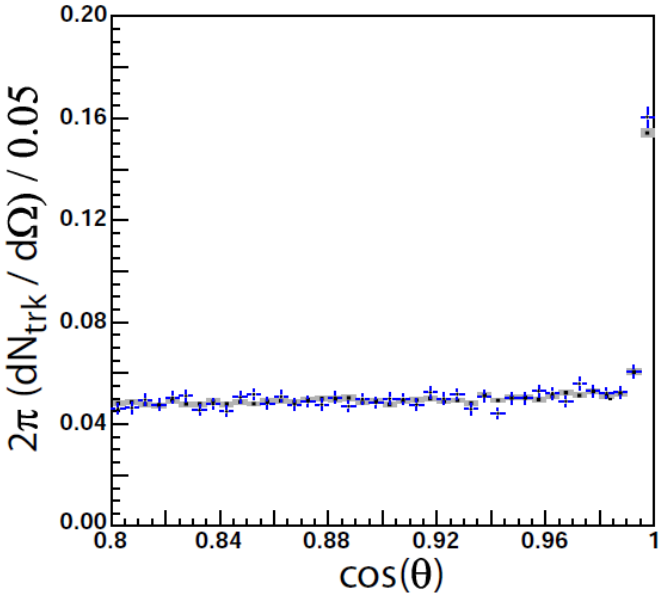

Figure 3.2: Density of all reconstructed tracks $2\pi dN_{\rm trk}/d\Omega$ per unit of solid angle plotted as a function of the angle θ with respect to the direction of the electron track in a clean sample of $Z^0 \to e^+e^-$ events. Only tracks contributing to the calculation of isolation variables are included.

for a given solid angle ($dN_{\rm trk}/d\Omega$) in $Z^0 \to e^+e^-$ decays in data and MC. This distribution can be seen in Figure 3.2 [39], as a funciton of the angle between the probe direction and the electron direction. The plot includes only tracks that are used in the isolation calculation. The "flat" region is due to the underlying event and multiple interactions, while the peak near $\cos\theta = 1$ is due to Bremsstrahlung photons that convert and is thus related to the amount of material. In this plot, the simulation is normalized to data in the "flat" region, and since the peak region (which also contains the "flat" contribution under it) also agrees, the conclusion is that inaccuracies in the material modeling have little impact on the measurement of the isolation efficiency. The difference in isolation efficiencies measured in $Z^0 \to e^+e^-$ data and MC is within 1.5%.

We use a scale factor of 1.0, and use the 1.5% as a contribution to the systematic [39]. There is an additional contribution to the systematic uncertainty of about 2% due to the potential difference in the stability and understanding of the isolation efficiency between LQ3 and Z^0 decays where the data-to-MC comparison mentioned above is made. Therefore, the total scale factor and systematic is taken as 1.00 ± 0.03.

There is a link between lepton isolation and the separation between leptons and jets discussed in Section 3.3.2. The lepton-jet separation requirement, with a veto on $0.3 < \Delta R(\ell, \text{jet}) < 0.8$ was in fact in part chosen to provide a cleaner environment for evaluating the efficiency of the isolation cut in simulation. Figure 3.3 shows the effect [44]. The plot shows the muon isolation cut efficiency as a function of ΔR between the muon and the closest jet, for $Z^0 \to \tau^+\tau^-$ (blue) and PYTHIA RPV stop pair production and decay (green). The jet environment in RPV stop decays to $\tau_\ell\tau_h bb$ is analogous to that of LQ3 decays to $\tau_\ell\tau_h bb$. The plot shows that the isolation

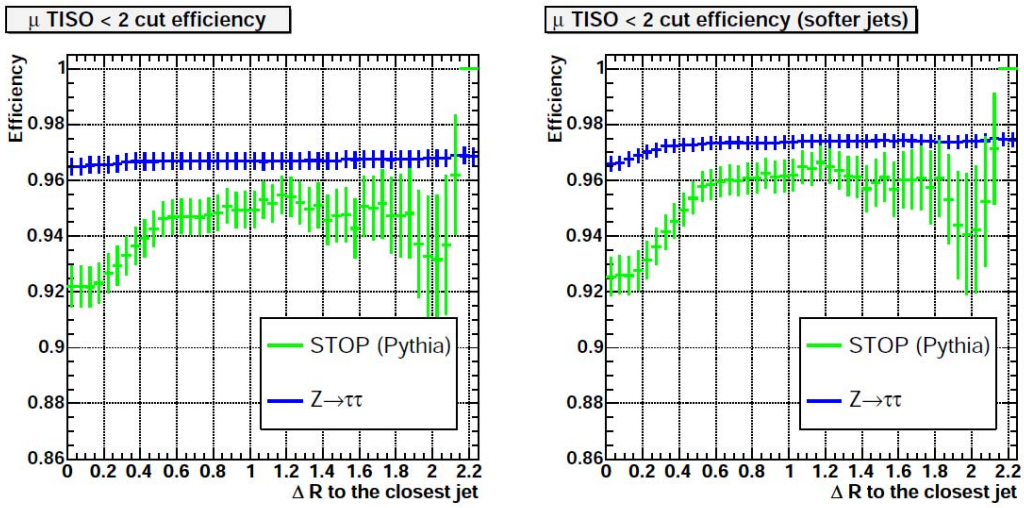

Figure 3.3: a) Cumulative efficiency of the lepton track isolation as a function of ΔR, where ΔR is the cut value of minimal separation between jet and a lepton. We compare $Z^0 \rightarrow \mu^+\mu^-$ and RPV stop events after all other ID cuts applied. This plot shows the track isolation strongly depends on jet closeness; b) To amplify this effect, we plot the same distribution, but with a softer jet definition threshold ($E_T^{\rm raw} > 6$ GeV, $E_T^{\rm cor} > 10$ GeV). This plot shows even better agreement between track isolation efficiencies in Z^0 and RPV stop samples for events with applied jet isolation $\Delta R > 0.8$.

efficiency is reasonably stable for the chosen region $\Delta R > 0.8$.

Lepton Trigger Efficiency

The events for this measurement are obtained through the *Lepton+Track* trigger. The triggering efficiencies for four different objects must be understood: CEM, CMUP, CMX, and TAU. Each is measured from a data sample, from the same time period as the sample used for the LQ3 search.

The efficiency for the electron leg (CEM) of the *Lepton+Track* trigger is measured using a sample of well-identified conversion candidates from jet and muon data [48, 49]. The efficiencies for the CMUP and CMX trigger paths of the *Lepton+Track* trigger are measured using samples of $Z^0 \rightarrow \mu^+\mu^-$ and $\Upsilon \rightarrow \mu^+\mu^-$ events [50]. Finally, the efficiency for the track leg, which is the seed for the hadronic tau candidate, is measured as a function of several variables used in tau identification [51, 52]. Furthermore, the referenced measurements include a study that finds that the track leg efficiency does not depend on the presence (or lack) of a lepton candidate.

For the cases of the electron and tau candidates, the parameterized trigger efficiencies are convoluted event by event with MC to obtain the effective trigger efficiencies. For the muon case, the efficiency is a constant over the relevant p_T range, so we use a single number. The results are summarized in Table 3.8.

Table 3.8: Trigger efficiencies (%) for electron (CEM), muon (CMUP and CMX), and tau (TAU) trigger paths. The effective efficiencies are shown for $\mathrm{LQ3}\overline{\mathrm{LQ3}} \to \tau\tau b\bar{b}$ using $m_{\mathrm{LQ3}} = 320\ \mathrm{GeV}/c^2$ MC. For comparison, efficiencies are also shown for $Z^0 \to \tau^+\tau^-$ and $\tilde{t}_1\bar{\tilde{t}}_1 \to \tau\tau b\bar{b}$ using $m_{\tilde{t}_1} = 150\ \mathrm{GeV}/c^2$ MC. In each case, the total efficiency is the combination of $\epsilon_{\mathrm{L1}} \times \epsilon_{\mathrm{L2}} \times \epsilon_{\mathrm{L3}}$. The first errors are statistical errors, and the second errors are systematic uncertainties

	$\mathrm{LQ3}\overline{\mathrm{LQ3}} \to \tau^+\tau^- b\bar{b}$	$Z^0 \to \tau^+\tau^-$	$\tilde{t}_1\bar{\tilde{t}}_1 \to \tau^+\tau^- b\bar{b}$
Trigger Path	Efficiency (%)	Efficiency (%)	Efficiency (%)
CEM electron	$97.0 \pm 0.1 \pm 1.0$	$96.0 \pm 0.1 \pm 1.0$	$97.6 \pm 0.2 \pm 1.0$
CMUP muon	$95.9 \pm 0.2 \pm 1.0$	$95.8 \pm 0.1 \pm 1.0$	$95.8 \pm 0.3 \pm 1.0$
CMX muon	$95.8 \pm 0.3 \pm 1.0$	$94.7 \pm 0.3 \pm 1.0$	$94.6 \pm 0.5 \pm 1.0$
TAU tau	$97.0 \pm 0.1 \pm 1.0$	$95.3 \pm 0.2 \pm 1.0$	$96.4 \pm 0.3 \pm 1.0$

Tau-Jet Separation

The tau-jet separation requirement is similar to that imposed for the lepton-jet combination (given in Section 3.3.2). This requirement removes taus from further consideration if they are too close to a jet candidate, but excludes those objects in the jet primitive list that are actually the same as the tau. The criterion is:

- Veto taus with $0.3 < \Delta R(\tau, \mathrm{jet}) < 0.8$

The efficiency for the tau-jet separation requirement is shown in the third line of Table 3.5 for the case of $m_{\mathrm{LQ3}} = 320\ \mathrm{GeV}/c^2$.

Tau Identification

The tau identification requirements are similar to those used in the $Z^0 \to \tau^+\tau^-$ measurement [38] and RPV stop measurement [44]. The tau track isolation is treated separately from identification in this measurement and is discussed in the next section. The efficiency is measured in LQ3 signal MC. The tau identification requirements and the corresponding efficiencies are given for the $e\tau_h$ channel and the $\mu\tau_h$ channel in Table 3.9.

- Seed Track Quality
  The seed track quality requirements are for at least 3 segments in the axial and at least 2 segments in the stereo supperlayers of the COT, with at least 5 hits per segment.
- $|z_0^{\tau\ \mathrm{seed}} - z_0^{\ell\ \mathrm{trk}}| \leq 5\ \mathrm{cm}$
- $|d_0^{\tau\ \mathrm{seed}}| < 0.2\ \mathrm{cm}$

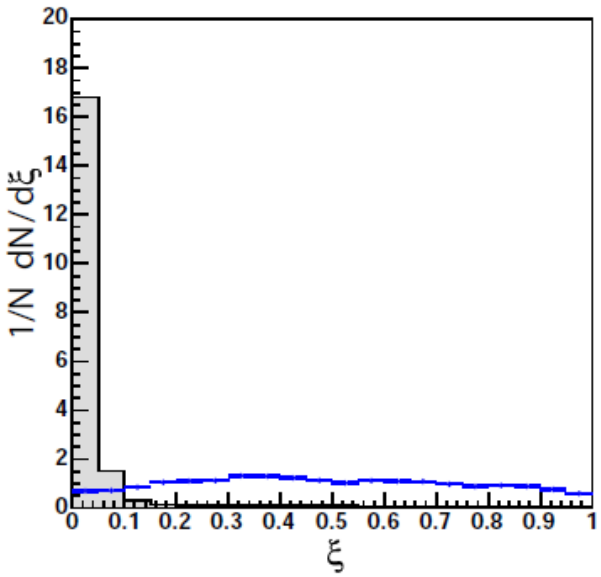

Figure 3.4: Distribution of valuable ξ for electrons and hadronic taus. Both distributions are normalized to a unit area.

- $\xi = E_{T\text{had}}/\sum p_T > 0.1$
  This selection is electron removal cut. Electorns can be reconstructed as hadronic tau objects if they have a narrow calorimeter cluster and a high p_T seed track. To remove electrons we demand that the tau be consistent with having only pions in the final state. The distribution for hadronic taus and electrons is shown in Figure 3.4, which allows substantial suppression of backgrounds from electrons faking a tau [40].

- $m_{\text{trk}} \leq 1.8$ and $m_{\text{trk}+\pi^0} \leq 2.5$ GeV/c^2
  The track mass, m_{trk} is the invariant mass of the 4-vector

$$p^{\tau-\text{trks}} \equiv \sum_{\Delta\Theta<\alpha_{\text{trk}}} p^{\pi^{\pm}} \tag{3.6}$$

  with the assumption that all tracks correpond to charged pions.

  The visible mass is invariant mass of the 4-vector

$$p^{\tau} \equiv \sum_{\Delta\Theta<\alpha_{\text{trk}}} p^{\pi^{\pm}} + \sum_{\Delta\Theta<\alpha_{\pi^0}} p^{\pi^0} \tag{3.7}$$

  We require $m_{\text{trk}+\pi^0} \leq 2.5$ GeV/c^2. This is somewhat higher than the actual 1.777 GeV/c^2 mass of the tau, however, a more stringent mass limit would be inefficient.

- $N_{\text{trk}}^{\tau\text{cone}} = 1, 3$
  Over 99.9% tau decays involve just 1 or 3 charged partices (prongs). We require that the tau candidate has 1 or 3 charged tracks with the angle α_{trk}.

$$\sum_{\Delta\Theta<\alpha_{\text{trk}}} \text{trk} = 1 \text{ or } 3 \tag{3.8}$$

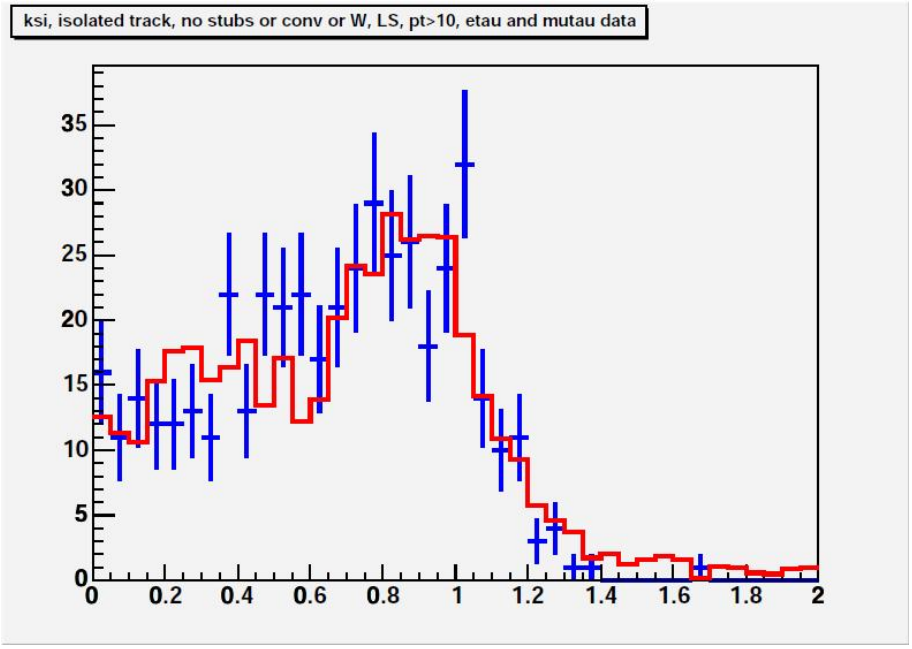

Figure 3.5: Distribution of ξ for the sample of charged track with $p_T > 10$ GeV/c compared with Monte Carlo.

The scale factors from the $Z^0 \to \tau^+\tau^-$ studies are applied. The result is 1.00 ± 0.03 [39, 40, 53].

Possible systematic biases to the efficiency of the ξ cut can be caused by improper simulation of the hadron calorimeter energy response to charged tracks showering early in the electromagnetic calorimeter. To study these effects, we select a sample of isolated charged pions by filtering jet events with exactly one 1-prong ta candidate passing all tau identification criteria. We ensure that these events have to other leptons in order to exclude contamination by electrons from $Z^0/\gamma^* \to e^+e^-$ and $Z^0/\gamma^* \to \tau^+\tau^-$ and also require no additional showers detected in CES to eliminate photons and neutral pions that may deposit additional energy in the hadron calorimeter. This ξ distribution with $p_T > 10$ GeV/c is plotted in Figure 3.5. Using this sample, we compare the efficiencies of the $\xi > \xi_0$ cut for several values of ξ_0 in the data and Monte Carlo simulation. The comparison shows a good agreement within the statistical precision of about 2%, which is taken as an estimate of the systematic uncertainty for this cut.

Efficiencies of the $m_{\rm trk}$ and $m_{{\rm trk}+\pi^0}$ cuts are compared in data and Monte Carlo using a clean sample of $W \to \tau\nu$ events. Figure 3.6 showns distribution of $m_{\rm trk}$ and $m_{{\rm trk}+\pi^0}$. The the $m_{{\rm trk}+\pi^0}$ shows disagreement of data and Monte Carlo for low and mid values of the mass. These effects are caused by that simulation is generated more π^0 than data, and tau energy correction is compensated for the lost π^0's, which are not used in caluclation of $m_{{\rm trk}+\pi^0}$. These cuts are intentionally set to be $\sim 100\%$ efficient, and systematic uncertainty is $\sim 0.4\%$.

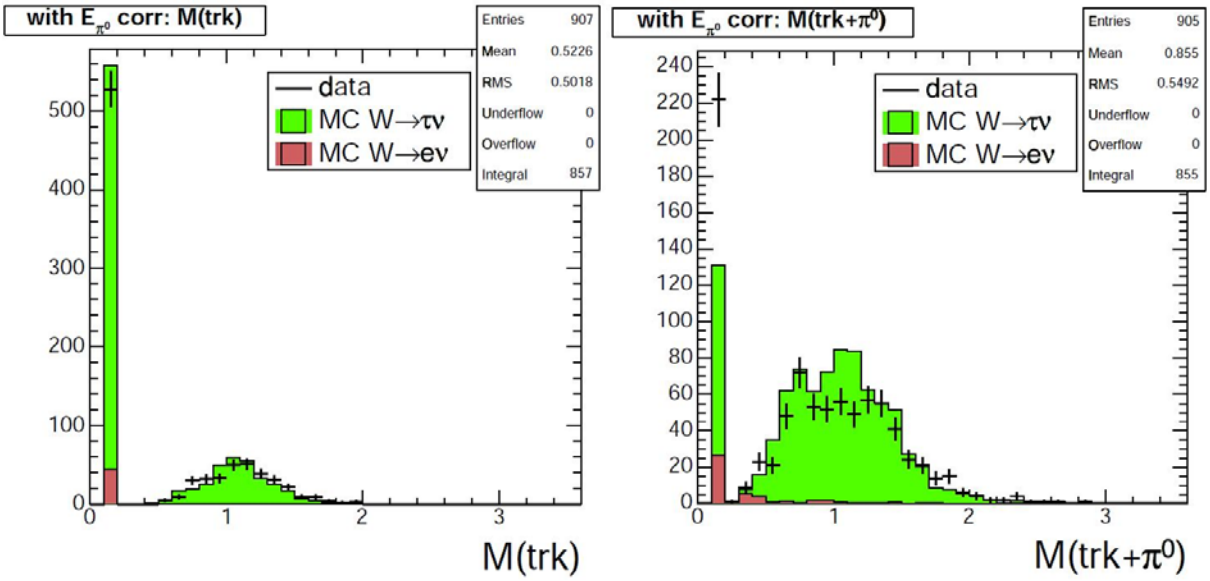

Figure 3.6: Tau track mass $m_{\rm trk}$ distribution (left) and tau visible mass $m_{\rm trk+\pi^0}$ distribution (right) for clean $W \rightarrow \tau\nu$ sample with requirement of tau charge to be ± 1. $W \rightarrow \tau\nu$ Monte Carlo is normalized on data minus $W \rightarrow e\nu$ Monte Carlo.

Table 3.9: Hadronic tau identification requirements and efficiencies, for the case of $m_{\rm LQ3} = 320\ {\rm GeV}/c^2$. The details of the track quality requirement are given in the text.

	$e\tau_h$	$\mu_{\rm CMUP}\tau_h$	$\mu_{\rm CMX}\tau_h$
Requirement	Efficiency (%)	Efficiency (%)	Efficiency (%)
Seed Track Quality	99.3 ± 0.1	99.1 ± 0.1	99.2 ± 0.2
$\lvert z_0^{\tau\ \rm seed} - z_0^{\ell\ \rm trk}\rvert \leq 5$ cm	98.0 ± 0.1	97.9 ± 0.1	98.1 ± 0.2
$\lvert d_0^{\tau\ \rm seed}\rvert < 0.2$ cm	97.3 ± 0.1	97.0 ± 0.2	97.3 ± 0.3
$\xi = E_{T\rm had}/\sum p_T > 0.1$	95.9 ± 0.2	95.5 ± 0.2	95.9 ± 0.4
$m_{\rm trk} \leq 1.8$ and $m_{\rm trk+\pi^0} \leq 2.5\ {\rm GeV}/c^2$	98.8 ± 0.0	98.6 ± 0.0	98.6 ± 0.0
$N_{\rm trk}^{\tau\rm cone} = 1, 3$	87.7 ± 0.3	87.6 ± 0.4	88.3 ± 0.6
Subtotal	66.1 ± 0.4	66.1 ± 0.5	67.5 ± 0.8
Scale Factor	1.00 ± 0.03	1.00 ± 0.03	1.00 ± 0.03
Total ID Efficiency	$66.1 \pm 0.4 \pm 0.2$	$66.1 \pm 0.5 \pm 0.2$	$67.5 \pm 0.8 \pm 0.2$

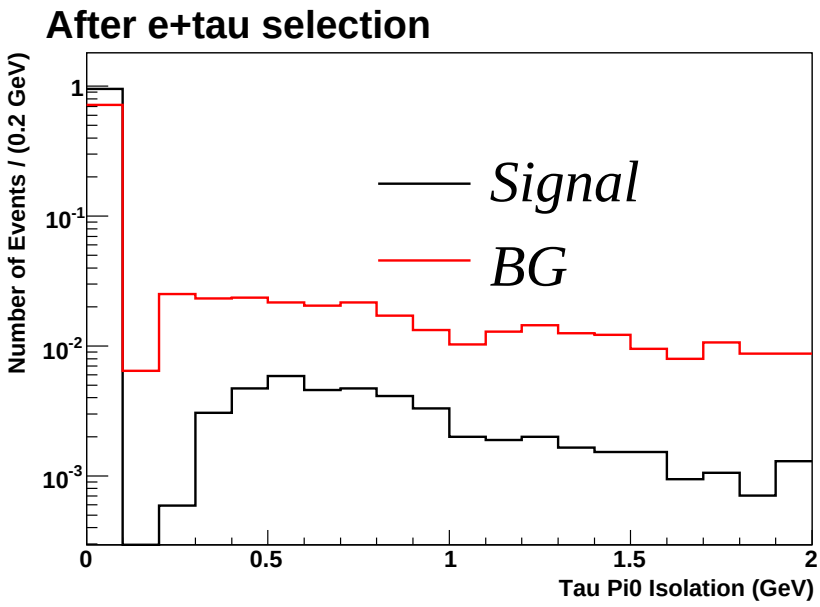

Figure 3.7: Distribution of hadronic tau π^0 isolation for signal MC with $m_{\mathrm{VLQ3}} = 280\ \mathrm{GeV}/c^2$ and background for $e\tau_h$ channel.

Tau Isolation

The tau isolation consists of two parts. First is a set of requirements on the number of additional candidate tracks near the tau seed track. There must be zero candidate tracks within an annulus, defined by a 3-dimensional angle $\Delta\Theta$ with respect to the tau seed track, with the inner edge of the annulus matching the energy-dependent cone that (by definition) surrounds the tau seed track and the outer edge at 30° from the seed track. Similarly, there must be zero candidate tracks within the range $10^\circ < \Delta R < 30^\circ$ with respect to the tau seed track. The second part of the tau isolation requirement is that the sum of the p_T of all π^0 candidates within an annulus (defined using $\Delta\Theta$ as above) surrounding the tau seed track, must be less than $0.6\ \mathrm{GeV}/c$.

The tau isolation criteria are summarized below, and the corresponding efficiencies are reported in Table 3.5.

- $N_{\mathrm{trk}}^{\tau\ \Delta\Theta} = 0$
- $N_{\mathrm{trk}}^{\tau\ \Delta R} = 0$
- $I_{\pi^0}^{\Delta\Theta} < 0.6\ \mathrm{GeV}/c\ \pi^0$ isolation is shown in Figure 3.7.

Tau Trigger Efficiency

The tau trigger efficiency is discussed in Section 3.3.2 and the results are displayed in Table 3.8.

Table 3.10: Event requirements and efficiencies, shown for the case of $m_{\mathrm{LQ3}} = 320\ \mathrm{GeV}/c^2$. The details of the requirements are discussed throughout Section 3.4.

Requirement	$e\tau_h$ Efficiency (%)	$\mu_{\mathrm{CMUP}}\tau_h$ Efficiency (%)	$\mu_{\mathrm{CMX}}\tau_h$ Efficiency (%)
Opposite sign charge ($Q_\ell \times Q_\tau = -1$)	99.3 ± 0.1	99.3 ± 0.1	99.4 ± 0.2
Conversion removal	97.8 ± 0.2	$--$	$--$
Cosmic removal	$--$	100.0 ± 0.0	100.0 ± 0.0
Z^0 removal	91.2 ± 0.3	96.1 ± 0.3	95.4 ± 0.5
$\not\!\!E_T > 10$ GeV	99.2 ± 0.1	99.4 ± 0.1	99.4 ± 0.2
$H_T > 400$ GeV	91.5 ± 0.3	91.0 ± 0.4	90.6 ± 0.7
$N_{\mathrm{jets}} \geq 2$	97.6 ± 0.2	97.2 ± 0.2	97.5 ± 0.4
Total Event Efficiency	78.4 ± 0.2	83.9 ± 0.2	83.3 ± 0.4

3.4 Event Level Requirements

This section gives the details of the event level requirements that are imposed to separate LQ3 signal from the backgrounds discussed in Section 4.1.

The summary of the efficiencies for all of the event selection requirements is shown in Table 3.10 for signal LQ3 MC with $m_{\mathrm{LQ3}} = 320\ \mathrm{GeV}/c^2$, separately for $e\tau_h$, $\mu_{\mathrm{CMUP}}\tau_h$, and $\mu_{\mathrm{CMX}}\tau_h$ channels.

Opposite Sign

The opposite sign charge requirement is as follows: The lepton candidate charge (Q_ℓ) and the tau candidate charge (Q_τ) must have opposite sign ($Q_\ell \times Q_\tau = -1$). The efficiency for this requirement, evaluated using signal LQ3 MC for the case of $m_{\mathrm{LQ3}} = 320\ \mathrm{GeV}/c^2$, is shown in Table 3.10.

Conversion Removal

For the $e\tau_h$ channel, electron candidates that are consistent with originating from a conversion process ($\gamma \rightarrow e^+e^-$) are removed from further consideration. The requirements used to identify possible conversions are one of the standard sets within CDF (see, for example, reference [54] which uses these same requirements, but a more complex algorithm) and are listed here:

- $|\Delta(\cot\theta)| \leq 0.04$
- $\Delta S_{xy} \leq 0.2\ \mathrm{cm}$

where θ is the angle between the two tracks being considered and S_{xy} is the distance between the two track helices where they are closest to each other. The concept for these requirements

comes from Run I (see for example [55]). The implementation of the conversion veto is in local code, rather than a shared module. The code uses tracks that pass a basic set of requirements (CDF tracks, with the additional requirements of at least 2 segments in the axial and at least 2 segments in the stereo supperlayers of the COT, with at least 5 hits per segment), and takes them in pairs to calculate the two quantities given above to see if they are consistent with coming from a conversion. The electron candidate in the LQ3 analysis is then vetoed if it appears in the list of conversion partner tracks. The efficiency for conversion removal is given in Table 3.10.

Cosmics Removal

For the $\mu\tau_h$ channel, muon candidates that are consistent with cosmic ray muons are removed from further consideration. We use a standard method for identifying cosmic ray candidates [56]. Even without the cosmics veto, to enter the final sample a cosmic ray event would have to overlap with additional activity in the detector and pass all of the other selection requirements. Cosmics removal is 100% efficient for our signal MC sample (as shown in Table 3.10).

Z^0 Removal

Z^0 removal is imposed to reject events where the lepton candidate, when paired with a second object (calorimeter object, tau candidate, or track), is consistent with the decay of a Z^0 boson. This applies to both the $e\tau_h$ and $\mu\tau_h$ channels, by veto of both $Z^0 \to e^+e^-$ and $Z^0 \to \mu^+\mu^-$. The efficiencies for Z^0 removal for the two channels are shown in Table 3.10, and the criteria for removal are given here:
Events are **removed** because of likeness to $Z^0 \to e^+e^-$ if a second `CdfEmObject`

- has $E_T^{\rm corr} > 8$ GeV,
- has $E_{\rm had}/E_{\rm em} < 0.12$,
- combines with the electron candidate to satisfy $76 < M(\mathrm{EmObj}, e) < 106$ GeV/c^2,

Figure 3.8(a) shows the Z^0 mass (Drell-Yan mass) reconstructed by all `CdfEmObject`. Figure 3.8(b) shows the Z^0 mass of above conditions before $76 < M(\mathrm{EmObj}, e) < 106$ GeV/c^2 selection.

Or they are **removed** if a tau candidate

- passes ID cuts,
- satisfies $\Delta\phi(\tau, e) > 2.9$,
- combines with the electron candidate to satisfy $76 < M(\tau, e) < 106$ GeV/c^2.

Events are **removed** because of likeness to $Z^0 \to \mu^+\mu^-$ if a second track

- matches any muon stub,
- has $p_T > 10$ GeV/c,

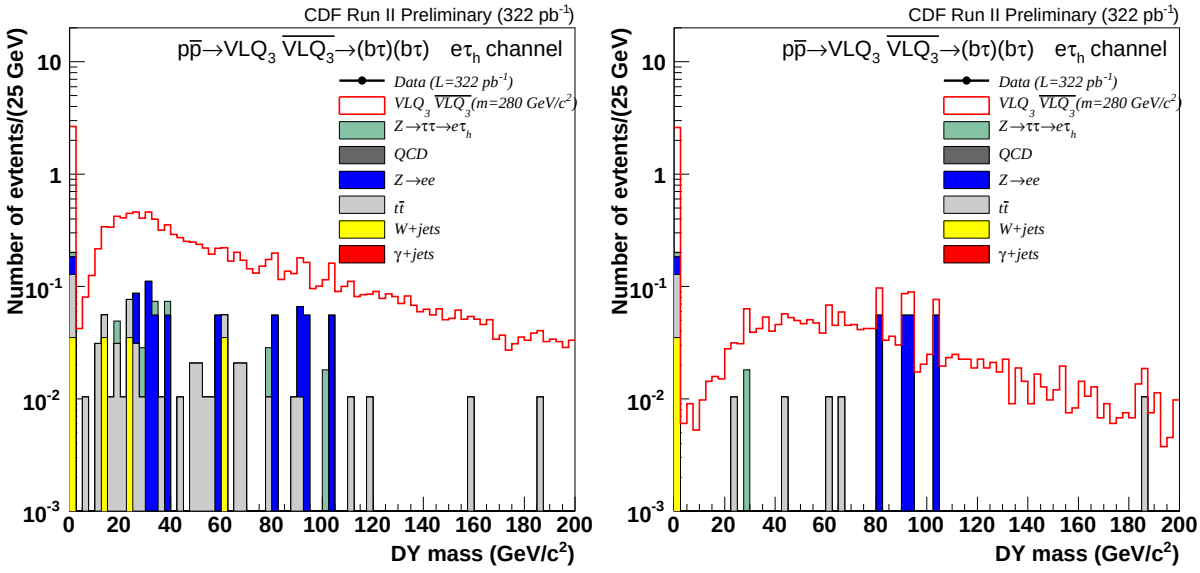

Figure 3.8: The distributions of Z^0 mass (Drell-Yan mass) reconstructed by (a) all electron candidates and (b) by electron candidates of $E_T^{\rm corr} > 8$ GeV and $E_{\rm had}/E_{\rm em} < 0.12$ for $m_{\rm LQ3} = 280$ GeV/c^2 and all background processes for the $e\tau_h$ channels.

- has $|z_0^{\rm trk} - z_0^{\mu}| < 5$ cm,
- combines with the muon candidate to satisfy $76 < M({\rm trk}, \mu) < 106$ GeV/c^2.

Baseline $\not\!\!E_T$ Requirement and $\not\!\!E_T$ Corrections

A baseline requirement of $\not\!\!E_T{}^{\rm corr} > 10$ GeV is applied, where $\not\!\!E_T{}^{\rm corr}$ is the corrected missing transverse energy. The corrections will be discussed below, but first some motivation for this requirement.

The baseline $\not\!\!E_T$ requirement reduces backgrounds of categories (mostly $Z^0 \to \tau^+\tau^-$ and QCD) that appear in the control region but do not appear in the signal region. On the other hand, it preserves background types (mostly $t\bar{t}$) which appear in both the control region and signal region, thus enhancing the usefulness of the control region in validation studies. The effect of the $\not\!\!E_T$ requirement on the signal Monte Carlo sample with $m_{\rm LQ3} = 320$ GeV/c^2 is given in Table 3.10, showing an efficiency of nearly 100%.

The $\not\!\!E_T$ requirement also eliminates a very specific class of non-control region and non-signal region events. While they are events that are not modeled by our current Monte Carlo simulation, they are not a background that appears in the signal or control regions of this analysis. They are eliminated from consideration by several analysis requirements including the $\not\!\!E_T$ requirement and the requirement that the hadronic taus have one or 3-prongs. They also fail the signal requirements of high H_T (discussed in Section 3.4) and the presence of two jets. Furthermore, they fall off quickly with H_T.

Several corrections are made to the raw $\not\!\!E_T$ of each event. First, in the $\mu\tau_h$ channel, the energy carried off by the primary muon candidate is subtracted, but the energy deposition in the

electromagnetic and hadronic calorimeters that has been associated with the muon candidate is added back into $\not\!\!E_T$ to keep from double counting that portion of the muon's total energy. This correction is summarized by the expression

$$\not\!\!E_T{}^{\rm corr}_{x,y} = \not\!\!E_T{}_{x,y} - p^{(\mu)}_{x,y}\left(1 - \frac{E_{\rm had} + E_{\rm em}}{p}\right) \ , \tag{3.9}$$

where the subscripts x and y refer to the x- and y-components of the relevant variable, and p is the magnitude of the muon momentum.

The second correction applies to the $e\tau_h$ channel and accounts for a transverse energy correction. It takes the following form:

$$\not\!\!E_T{}^{\rm corr}_{x,y} = \not\!\!E_T{}_{x,y} - p^{(e)}_{x,y}\left(f_T^{e\ {\rm corr}} - 1\right) \ , \tag{3.10}$$

where $f_T^{e\ {\rm corr}}$ is the same correction factor that is used to correct the transverse energy for use in the the electron acceptance and ID requirements (in particular $E_T^{\rm corr} = E_T f_T^{e\ {\rm corr}}$). This correction only uses the primary electron candidate.

Next is a correction of the $\not\!\!E_T$ due to the transverse energy correction of the jets used in the analysis

$$\not\!\!E_T{}^{\rm corr}_{x,y} = \not\!\!E_T{}_{x,y} - \sum_{\rm jets} p^{\rm (jet)}_{x,y}\left(f_T^{\rm jet\ corr} - 1\right) \ , \tag{3.11}$$

where the sum is over jets that satisfy the requirements given in Section 3.3.2, and $f_T^{\rm jet\ corr}$ is the level 5 jet energy correction factor. In the above sum, we are careful not to include the primitive jets that corresponds to any well identified electrons in the event.

Finally, there is a correction to the $\not\!\!E_T$ due to a difference between the default tau reconstruction algorithm and a newer preferred method. The former uses an $E_T > 1$ GeV threshold to choose cluster towers to include in the tau cluster momentum while the latter, called the expanded tau cluster momentum, includes neighboring low E_T towers in the cluster momentum to account for energy leakage into those towers. The correction, which uses only the information from the primary tau candidate, is given by the following expression:

$$\not\!\!E_T{}^{\rm corr}_{x,y} = \not\!\!E_T{}_{x,y} - \left(p^{\tau}_{x,y}({\rm visible}) - p^{\tau}_{x,y}({\rm expanded\,cluster})\right) \ . \tag{3.12}$$

H_T Requirement and Optimization

A highly effective event selection requirement for this analysis uses the scalar sum of the relevant available energies: the electron or muon candidate energy, the tau candidate energy, the missing energy, and the sum of the energies of the two highest energy jets that pass the jet requirements. This is written as

$$H_T = E_T(e,\mu) + E_T(\tau_h) + \not\!\!E_T{}^{\rm corr} + \sum E_T({\rm jets}) \ . \tag{3.13}$$

Figure 3.9(a) shows the H_T distribution for signal LQ3 MC with $m_{\rm LQ3} = 320$ GeV/c^2 and backgrounds. Both the signal and backgrounds are displayed separately for the $e\tau_h$ and $\mu\tau_h$ channels, and there is an additional requirement of $N_{\rm jets} \geq 2$, as discussed in Section 3.4. Figure 3.9(b) shows the significance $S/\sqrt{S+B}$ verses H_T. This optimization variable supports the choice of

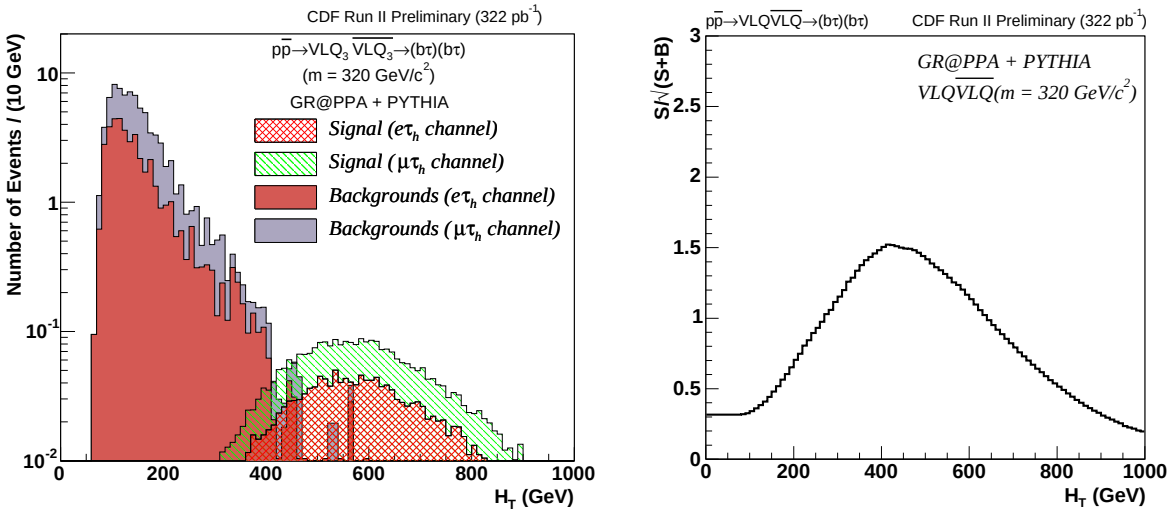

Figure 3.9: (a) Stacked distributions for H_T for signal MC with $m_{\mathrm{LQ3}} = 320\ \mathrm{GeV}/c^2$ and backgrounds, separated for the $e\tau_h$ and $\mu\tau_h$ channels. There is also a requirement of $N_{\mathrm{jets}} \geq 2$. [Note: if the signal MC histograms do not display as colored hatched regions, please switch OFF the anti-aliasing feature of your document viewer.] (b) Significance variable $S/\sqrt{S+B}$ verses H_T. This prompts the event selection requirement of $H_T > 400\ \mathrm{GeV}$.

- $H_T > 400\ \mathrm{GeV}$.

Note that the optimal choice of H_T requirement depends upon the LQ3 mass, and lower masses would prompt a lower choice of the requirement. Our goal has been to extend the mass reach as high as possible, but we are also careful not to miss an LQ3 between the previous search limit and our maximum sensitivity.

The safety region (SAFE) has $250 < H_T < 400\ \mathrm{GeV}$, and serves better sensitivity to lower mass range. Note that the final result uses a simultaneous fit included the safety region.

The use of the H_T requirement is one of the largest differences between this analysis and the RPV stop [44] analysis, where the variable Y_T was used. The quantity Y_T is the same as H_T except that it lacks the jet energies. The motivation is that there should be additional discriminating power provided by the energy carried away by the jets, from these relatively heavy LQ3s. Indeed the H_T cut has a slightly higher significance (1.23) than the significance (1.12) of the requirement of $Y_T > 200\ \mathrm{GeV}$ found through a similar optimization procedure.

The efficiency of the H_T requirement on signal MC is shown in Table 3.10. After this requirement, the largest surviving background source is $t\bar{t}$.

N_{jets} Requirement

The final event selection requirement is on the number of jets. The jet definitions used for counting the jets are those of Section 3.3.2, and the requirement is

- $N_{\mathrm{jets}} \geq 2$.

The efficiency is shown in Table 3.10.

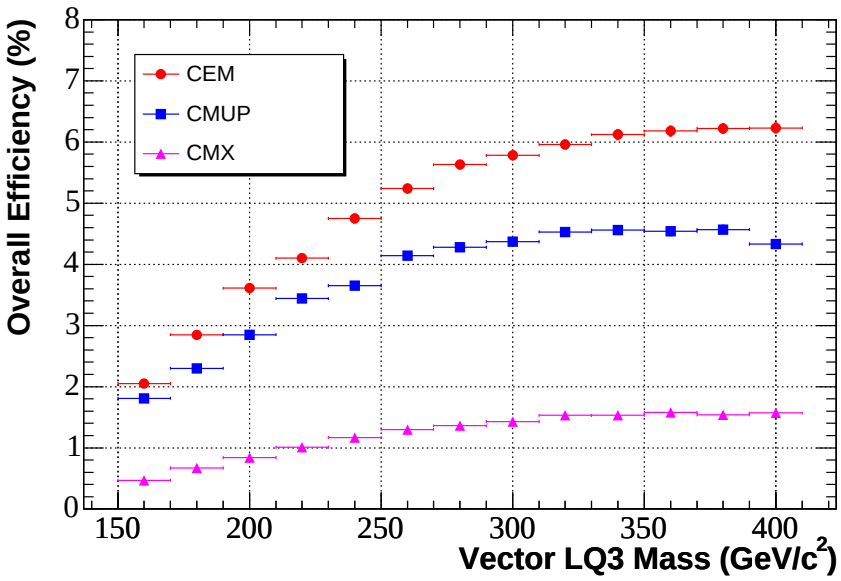

Figure 3.10: The full event selection efficiencies for CEM, CMUP, and CMX as a function of LQ3 mass for an LQ3 with Yang-Mills couplings.

3.5 Efficiencies as a Function of LQ3 Mass

The efficiency of the full event selection depends on LQ3 mass. The dependence is shown in Figure 3.10 and Figure 3.11. The summary of overall efficiencies is shown in Table 3.11 for $m_{\mathrm{LQ3}} = 320\ \mathrm{GeV}/c^2$, separately for the $e\tau_h$ and $\mu\tau_h$ channels. Also, for comparison, Table 3.12 shows the summary of overall efficiencies for an LQ3 with Yang-Mills couplings and $m_{\mathrm{LQ3}} = 360\ \mathrm{GeV}/c^2$, which is near the measured mass limit.

And, The dependence after $H_T > 250\ \mathrm{GeV}$ (safety and signal regions) is shown in Figure 3.12.

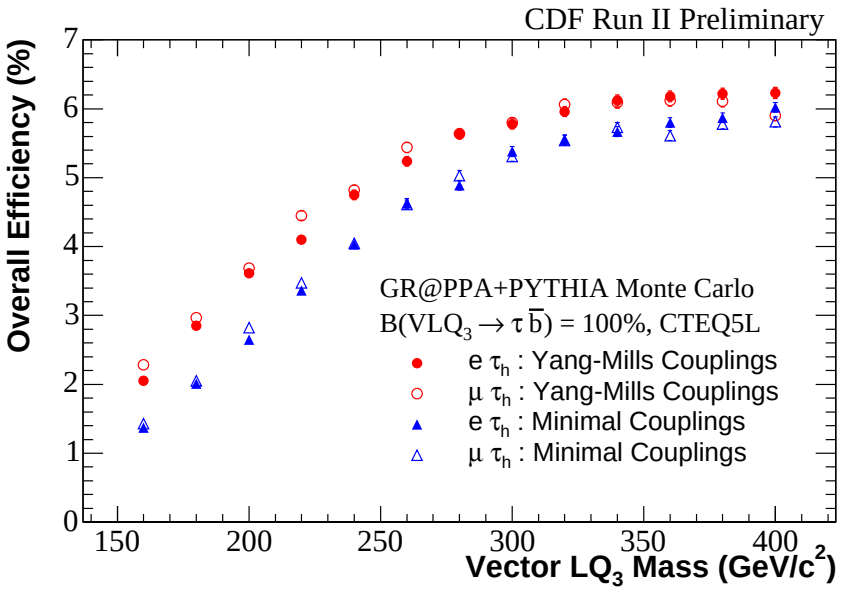

Figure 3.11: The full event selection efficiency as a function of LQ3 mass for the $e\tau_h$ and $\mu\tau_h$ channels, shown separately for the cases of Yang-Mills and Minimal couplings.

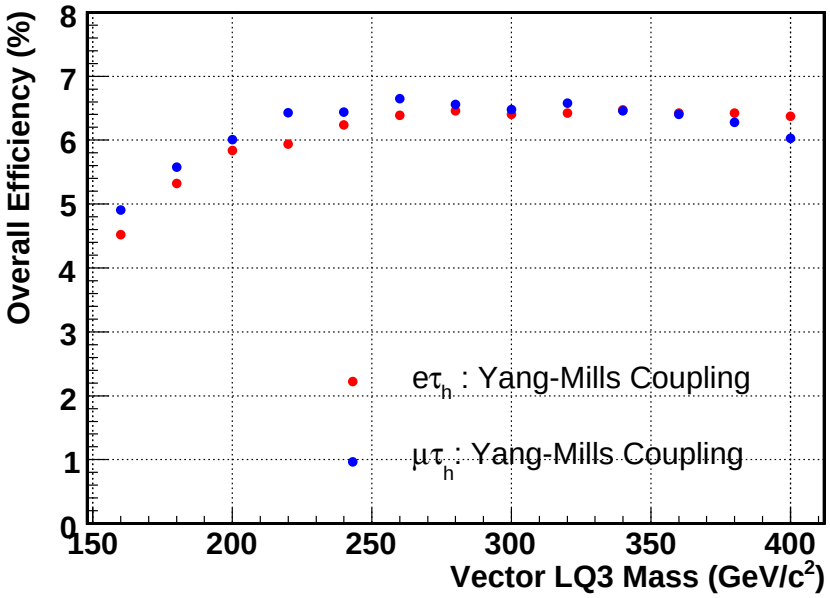

Figure 3.12: The full event selection efficiencies after $H_T > 250$ GeV for the $e\tau_h$ and $\mu\tau_h$ channels as a function of LQ3 mass for an LQ3 with Yang-Mills couplings.

Table 3.11: Summary of overall efficiencies, including acceptances, separations, identification, isolations, trigger, and event level requirements. These apply to an LQ3 with Yang-Mills couplings and $m_{\mathrm{LQ3}} = 320\ \mathrm{GeV}/c^2$.

Requirement	$e\tau_h$ Efficiency (%)	$\mu_{\mathrm{CMUP}}\tau_h$ Efficiency (%)	$\mu_{\mathrm{CMX}}\tau_h$ Efficiency (%)
ℓ acceptance	46.3 ± 0.2	28.4 ± 0.1	9.1 ± 0.1
τ_{h} acceptance	56.0 ± 0.2	56.7 ± 0.3	55.6 ± 0.5
$\ell - \tau_{\mathrm{h}}$ sep.	96.7 ± 0.1	96.3 ± 0.2	97.4 ± 0.2
Subtotal	$25.1 \pm 0.1 \pm 0.4$	$14.6 \pm 0.1 \pm 0.1$	$4.8 \pm 0.1 \pm 0.0$
$\ell - \mathrm{jet}$ sep.	$90.3 \pm 0.2 \pm 0.0$	$88.5 \pm 0.3 \pm 0.0$	$90.8 \pm 0.4 \pm 0.0$
ℓ ID	$82.4 \pm 0.3 \pm 0.8$	$85.2 \pm 0.3 \pm 2.7$	$89.7 \pm 0.4 \pm 0.3$
ℓ iso.	$88.4 \pm 0.2 \pm 2.7$	$94.9 \pm 0.2 \pm 2.8$	$95.4 \pm 0.3 \pm 2.9$
ℓ trigger	$97.0 \pm 0.1 \pm 1.0$	$95.9 \pm 0.2 \pm 1.0$	$95.8 \pm 0.3 \pm 1.0$
$\tau_{\mathrm{h}} - \mathrm{jet}$ sep.	$93.9 \pm 0.2 \pm 0.0$	$93.9 \pm 0.2 \pm 0.0$	$94.5 \pm 0.4 \pm 0.0$
τ_{h} ID	$66.1 \pm 0.4 \pm 0.2$	$66.1 \pm 0.5 \pm 0.2$	$67.5 \pm 0.8 \pm 0.2$
τ_{h} iso.	$79.1 \pm 0.4 \pm 2.4$	$79.2 \pm 0.5 \pm 2.4$	$79.8 \pm 0.8 \pm 2.4$
τ_{h} trigger	$96.9 \pm 0.2 \pm 1.0$	$97.0 \pm 0.2 \pm 1.0$	$97.6 \pm 0.4 \pm 1.0$
Subtotal	$7.6 \pm 0.1 \pm 3.9$	$5.4 \pm 0.1 \pm 4.8$	$1.8 \pm 0.0 \pm 4.0$
Event Selection	78.4 ± 0.2	83.9 ± 0.2	83.3 ± 0.4
Total	$6.0 \pm 0.1 \pm 3.1$	$4.5 \pm 0.1 \pm 4.0$	$1.5 \pm 0.0 \pm 3.3$

Table 3.12: Summary of efficiencies for $m_{\mathrm{LQ3}} = 360\ \mathrm{GeV}/c^2$, which is close to the observed mass limit. The row (Particle Selection) is the summary of acceptances, separations, identification, isolations, and trigger efficiencies. The columns are for $e\tau_h$, $\mu_{\mathrm{CMUP}}\tau_h$, $\mu_{\mathrm{CMX}}\tau_h$.

Requirement	$e\tau_h$ Efficiency (%)	$\mu_{\mathrm{CMUP}}\tau_h$ Efficiency (%)	$\mu_{\mathrm{CMX}}\tau_h$ Efficiency (%)
Particle Selection	7.52 ± 0.08	5.17 ± 0.07	1.84 ± 0.04
Event Selection	81.73 ± 0.19	87.37 ± 0.25	85.83 ± 0.36
Total	6.14 ± 0.07	4.52 ± 0.07	1.58 ± 0.04

Chapter 4

Backgrounds

4.1 Backgrounds

This section describes the contributing backgrounds, how the backgrounds are estimated, and how the uncertainties are obtained.

Note that only a subset of the background categories contribute in the signal region and in the control regions, while the remainder contribute only in the control regions. The latter set is included in this analysis so that the control regions can reliably be used for their intended purpose of validation.

4.1.1 $Z^0/\gamma^* \rightarrow \tau^+\tau^-$, and $Z^0/\gamma^* \rightarrow e^+e^-$ or $Z^0/\gamma^* \rightarrow \mu^+\mu^-$

Both the $e\tau_h$ and $\mu\tau_h$ channels can suffer contamination from the $Z^0/\gamma^* \rightarrow \tau\tau$ process if two additional jets that pass the analysis requirements are present. Note also that one of the taus must pass as the hadronic tau and one must pass as the leptonic tau. The contribution from this source is estimated using about 7.6 million events of PYTHIA MC (dataset zewk8t).

The $e\tau_h$ channel can also have a contribution from $Z^0/\gamma^* \rightarrow e^+e^-$. It is possible that one of the electrons fakes a hadronic tau and there are at least two jets in the event that pass the jet requirements. Also it is possible that one of the electrons is not reconstructed (or does not combine with the other electron to get eliminated by the Z^0 veto) and there are at least three jets in the event, one of which fakes a hadronic tau. The contribution for this source is estimated using approximately 2.9 million events of PYTHIA MC (dataset zewk6d).

Likewise, the $\mu\tau_h$ channel can have a contribution from $Z^0/\gamma^* \rightarrow \mu^+\mu^-$. Again, there are two possibilities: one of the muons fakes a hadronic tau and there are at least two jets in that event that pass the jet requirements, or one of the muons is missed (or does not combine with the other muon to get eliminated by the Z^0 veto) and there are at least three jets in the event, one of which fakes a hadronic tau. This source is estimated using roughly 3.1 million events of PYTHIA MC (dataset zewk6m).

The systematic uncertainties considered for each of the above sources include those due to the jet energy scale and $\not\!\!E_T$. The techniques used to evaluate the uncertainties are the same as those used for the signal and are detailed for that purpose in Section 5.1. The systematic uncertainties for fake rates are 20% for electrons faking taus, and 40% for muons faking taus [57, 58].

4.1.2 $W + \mathrm{jets}$

Events with $W + \mathrm{jets}$ can mimic the LQ3 signature, particularly when $W \to e\nu$, $W \to \mu\nu$, or $W \to \tau\nu$ followed by $\tau \to e\nu$ or $\tau \to \mu\nu$. In addition to the resulting lepton, a jet must fake a hadronic tau, and two additional jets must pass the jet requirements.

The samples used for this study include about 5.4 million events of $W \to e\nu$ PYTHIA MC (dataset wewkfe), about 3.1 million events of $W \to \mu\nu$ PYTHIA MC (dataset wewk6m), and about 8.7 million events of $W \to \tau\nu$ PYTHIA MC (dataset wewk9t).

The modeling of this background in Monte Carlo simulation is somewhat unreliable in normalization and in distribution among the jet multiplicity bins. We account for this by scaling the MC to match the data in control regions with enhanced $W + \mathrm{jets}$ contributions. A good kinematic quantity to use for this is the transverse mass, M_T, of the lepton and $\not\!\!E_T$:

$$M_T = \sqrt{2p_T{}^{(\mu)}\not\!\!E_T(1 - \cos\Delta\phi)} \text{ for muons and} \tag{4.1}$$

$$M_T = \sqrt{2E_T^{(e)}\not\!\!E_T(1 - \cos\Delta\phi)} \text{ for electrons,} \tag{4.2}$$

where $\Delta\phi$ is the angle between the lepton direction and the $\not\!\!E_T$ direction. In the region with $M_T > 40$ GeV, the $W + \mathrm{jets}$ contribution dominates for the cases of $N_{jets} = 0$ and $N_{jets} = 1$, and is comparable to all other sources combined for $N_{jets} \geq 2$. This will be explained in Figure 4.7. The scaling procedure, performed for each jet multiplicity bin (control regions CR0J, CR1J, and CR2J, see Figure 4.1), uses a χ^2 between the data and the sum of all backgrounds, and minimizes this χ^2 to find the $W + \mathrm{jets}$ scale factor. This is done for a combined sample of $e\tau_h$ and $\mu\tau_h$ since the scale factors should be the same for both channels, and there is a benefit to the increased statistics of the combined sample. The procedure is repeated for $M_T > 60$ GeV and the differences between results obtained using $M_T > 40$ GeV and $M_T > 60$ GeV are used as systematic uncertainties on this scaling method. The resulting scale factors are shown in Table 4.1.

The statistics of the sample are further enhanced by relaxing some of the τ_h identification requirements and deriving a scale factor in the lower H_T region where there are more events. The τ_h identification requirements that are relaxed include: changing the tau isolation from no tracks with $p_T > 1$ GeV/c to no tracks with $p_T > 2$ GeV/c, dropping the requirement on the number of tracks in the 10-30 degree annulus, and increasing the track+π^0 mass cut to 4 GeV/c^2. Also, we drop the the opposite sign charge requirement. The enhanced statistics lead to a smaller scale factor, and therefore a smaller statistical uncertainty on this background prediction.

4.1.3 W^+W^-

The production of W^+W^- pairs and subsequent decay of one W to $\tau\nu$ and the other to $e\nu$ or $\mu\nu$, plus the existence of additional jets, or other combinations, could in principle be a background to

Table 4.1: Scale factors to normalize the $W + \mathrm{jets}$ background from Monte Carlo simulation to data. The first uncertainty is statistical, the second is a systematic.

N_{jets}	Scale Factor
≥ 2	$0.84 \pm 0.38 \pm 0.13$
1	$0.74 \pm 0.13 \pm 0.11$
0	$0.58 \pm 0.06 \pm 0.09$

this search. However, the cross section is small enough that any contribution from this process is negligible. This is found using roughly 0.4 million events of PYTHIA MC (dataset wtop1w). The diboson processes WZ and ZZ are also negligible.

4.1.4 $t\bar{t}$

The background from $t\bar{t}$ events contributes primarily in two ways: (1) The event contains two decays of the type $t \rightarrow Wb$, and one W yields a hadronic tau and the other yields a lepton, and the two b quarks give jets, just as in the LQ3 signal, or (2) there are additional jets in the event (perhaps from one of the W bosons decaying to quarks instead), and one of the available jets fakes an electron, muon, or hadronic tau. There can also be an electron or muon, from a W decay, that fakes a hadronic tau. This background is studied using approximately 0.2 million events of PYTHIA MC (dataset ttop0z), and assuming a $t\bar{t}$ cross section of $6.7\ \mathrm{pb}$.

The systematic uncertainty for the $t\bar{t}$ contribution accounts for the fact that it is made up of two components. The portion that is due to real physics processes is dominated by systematics for the jet energy scale, $\not\!\!E_T$, identification, and isolation. The portion that is due to one sort of particle faking another is dominated by uncertainties in the fake rates, which is approximated with 50% by several fake rates: jets faking taus ($\sim 40\%$), electrons faking taus ($\sim 20\%$), muons faking taus ($\sim 40\%$), jets faking electrons ($\sim 40\%$) and jets faking muons ($\sim 40\%$) [57, 58, 59].

4.1.5 QCD

The production of light quarks through QCD processes can mimic the signal by jets faking leptons and hadronic taus. There must also be additional jets to satisfy the $N_{\mathrm{jets}} \geq 2$ requirement. For heavy flavor quarks, the signal candidate muon or electron can come from the semileptonic decay of a hadron containing the heavy quark, and a semileptonic decay product can also fake a hadronic tau.

The technique used to estimate the background from QCD follows [38] and uses the amount of data in a non-signal region where the lepton is non-isolated ($2 < I < 10$), where QCD dominates, to project into a more signal-like region where the lepton is isolated ($0 < I < 2$). The method uses the ratio (2-0)/(10-2) = 2/8 to perform the scaling, and utilizes the fact that the QCD background is flat as a function of isolation. The data sample used for this background estimate is the same as the one used to look for LQ3 events.

To further reduce the statistical uncertainty of this background estimate, we obtain a larger sample, and therefore a smaller scale factor, by relaxing some of the event requirements. In particular, we change the requirement on the number of tracks from being 1 or 3 to simply being < 4. We also remove the opposite sign requirement. Together, these reduce the scale factor by approximately another factor of 4.

4.1.6 $\gamma + \mathrm{jets}$

Events with a photon and additional jets can fake the signal signature due to photon conversions that are not removed by the conversion veto. One of the two conversion products could be missed, or the two could be too close together and appear as a single electron, and could become the electron candidate. Plus, a jet could fake the hadronic tau, while two other jets could satisfy the $N_{\mathrm{jets}} \geq 2$ requirement.

This background is estimated using the same data sample that is used for the LQ3 search. We use like-sign (LS) data events (to avoid including our signal) to determine the number of events, $N_{\mathrm{LS\ data}}$, with well isolated electrons ($0 < I < 2$). From this we subtract the like-sign background, $N_{\mathrm{LS\ bkg}}$, using non-isolated events for the QCD estimate and events with well isolated electrons for all of the other categories of backgrounds already discussed. The difference, $D = N_{\mathrm{LS\ data}} - N_{\mathrm{LS\ bkg}}$, is attributed to the conversions from $\gamma + \mathrm{jets}$. Next, the control regions are used to count the number, N_{conv}, of like-sign or opposite-sign (OS) events that pass the conversion tagger (by reversing the conversion veto). Finally, the ratio D/N_{conv} is used as a scale factor to multiply the number of tagged conversions in each region to estimate the contribution from $\gamma + \mathrm{jets}$ and to determine the statistical uncertainty. The systematic uncertainties on the final event estimates include the uncertainty on the scale factor. The resulting scale factors are shown in Table 4.2.

4.1.7 Summary of Backgrounds

The samples used to estimate backgrounds are summarized in Table 4.3. The number estimates are given within Section 5.

4.2 Definition of the Signal and Control Regions

Three different control regions are used in the plane of N_{jets} versus H_T to verify our understanding of the composition of the backgrounds, and our understanding of distributions for the kinematic quantities. We have also defined a *safety* region, and the signal region. This section gives the specifications of these various regions.

The three control regions are called CR0J, CR1J, and CR2J and their locations in the plane of N_{jets} versus H_T are shown in Figure 4.1. The CR stands for control region, and the 0J, 1J, or 2J specifies the number of jets (0, 1, or ≥ 2). Regions CR0J and CR1J include the H_T range $H_T > 80$ GeV, while region CR2J is restricted to $80 < H_T < 250$ GeV.

Table 4.2: $\gamma + \text{jets}$ is estimated using data for the LQ3 search. We use LS data events (to avoid including our signal) to determine the number of events $N_{\text{LS data}}$. From this we subtract the LS background $N_{\text{LS bkg}}$. The difference, $D = N_{\text{LS data}} - N_{\text{LS bkg}}$, is attributed to the conversions from $\gamma + \text{jets}$. Next, the control regions are used to count the number, N_{conv}, of LS or OS events that pass the conversion tagger. Finally, the ratio D/N_{conv} is used as a scale factor to multiply the number of tagged conversions in each region to estimate the contribution from $\gamma + \text{jets}$.

Process	Number of Events	Sign	Conversion
Data	97	LS	veto
$Z^0/\gamma^* \to \tau^+\tau^-$	1.94	LS	veto
$Z^0/\gamma^* \to e^+e^-$	3.94	LS	veto
$W + \text{jets}\,(W \to e\nu)$	30.3	LS	veto
$W + \text{jets}\,(W \to \tau\nu)$	9.34	LS	veto
$t\bar{t}$	0.0624	LS	veto
QCD	30.5	LS	veto
Total background	76.1	LS	veto
$D(= N_{\text{LS data}} - N_{\text{LS bkg}})$	20.9	LS	veto
Data	287	OS or LS	tagged
$f_{\text{conv}}(= D/N_{\text{conv}})$	0.073		

Table 4.3: Background processes. Except for the QCD and $\gamma + \text{jets}$ which are data-based, all the other use the PYTHIA MC generator. The number of events quoted is after application of a good run list. The factor multiplying the cross section. It is due to the ratio of the full mass range to the limited mass range in which the production was done.

Process	Dataset ID	release	# events	cross section	scale factor
$Z^0/\gamma^* \to \tau^+\tau^-$	zewk8t	5.3.3_EWK	7,598,445	1.95×255 pb	0.0192
$Z^0/\gamma^* \to e^+e^-$	zewk6d	5.3.3_EWK	2,879,005	1.95×255 pb	0.0556
$Z^0/\gamma^* \to \mu^+\mu^-$	zewk6m	5.3.3_EWK	3,050,971	1.96×255 pb	0.0362
$W + \text{jets}\,(W \to e\nu)$	wewkfe	5.3.2_EWK	5,366,615	2687 pb	0.161
$W + \text{jets}\,(W \to \mu\nu)$	wewk6m	5.3.3_EWK	3,114,127	2687 pb	0.237
$W + \text{jets}\,(W \to \tau\nu)$	wewk9t	5.3.3_EWK	8,709,395	2687 pb	0.485
W^+W^-	wtop1w	5.3.3	373,511	11 pb	0.00950
$t\bar{t}$	ttop0z	5.3.3	208,335	6.7 pb	0.0104
QCD	etlp0d	5.3.1			0.25
$\gamma + \text{jets}$	etlp0d	5.3.1			

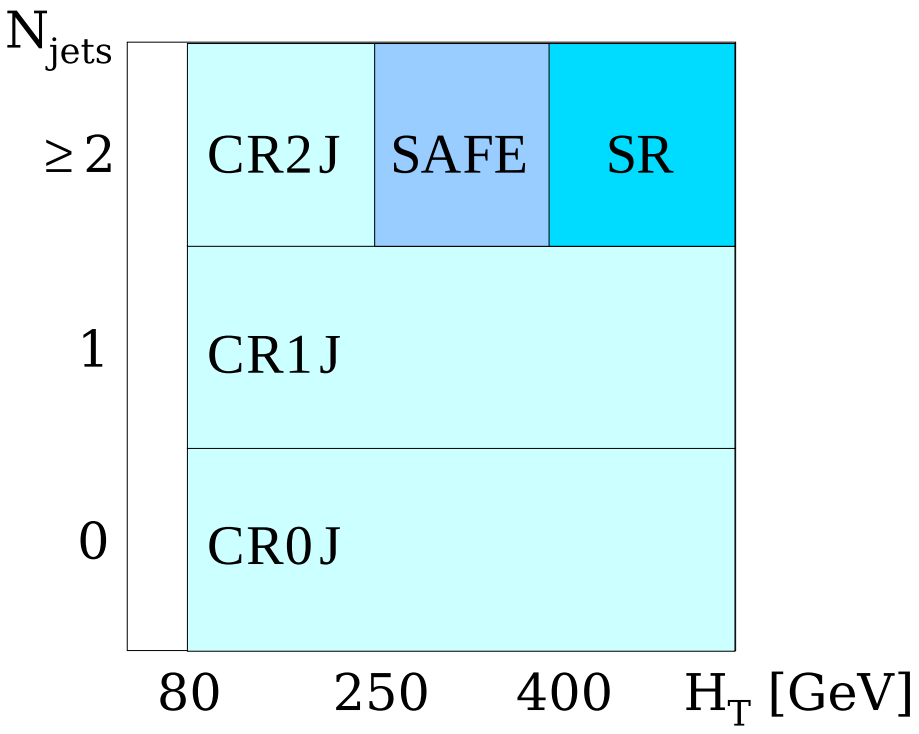

Figure 4.1: Definitions of the control regions (CR0J, CR1J, and CR2J), the safety region (SAFE), and the signal region (SR). Details are given in the text of Section 4.2.

The signal region (SR) is defined as having $N_{\text{jets}} \geq 2$ and $H_T > 400$ GeV. This is the region for which the analysis has been optimized. The safety region (SAFE) has $N_{\text{jets}} \geq 2$ and $250 < H_T < 400$ GeV, and serves as a buffer between the signal region and the control region. The control region below $H_T = 250$ GeV will not be sensitive to a vector leptoquark heavier than the existing limit of $m_{\text{LQ3}} > 225$ GeV/c^2, while the safety region of $250 < H_T < 400$ GeV could have such sensitivity. Therefore, the data in the safety region had not been examined until the control region studies were completed. Note that the final result uses a simultaneous fit to both the safety and signal regions.

4.3 Control Region Checks

Figures 4.2- 4.9 show distributions in the control regions defined in Section 4.2. In each case, the left column of plots are for the $e\tau_h$ channel and the right column for the $\mu\tau_h$ channel. Also, the first, second, and third rows are for the CR0J, CR1J, and CR2J control regions, respectively. The individual contributions are stacked in the histograms. The legends are self explanatory, with two exceptions. First, the signal leakage is shown (but not seen) by including the LQ3 signal MC ($m_{\text{LQ3}} = 280$ GeV/c^2) in these plots as a white histogram with a red boarder. Only the red boarder is visible (at the top of each histogram), since there is no signal contribution in the control regions. Second, the contribution from $W + \text{jets}$ background is divided into two components for each channel depending upon the decay mode of the W: one where $W \to e\nu$ or $W \to \mu\nu$ is

shown as yellow above the gray line and one where $W \rightarrow \tau\nu$ is shown as yellow below the gray line.

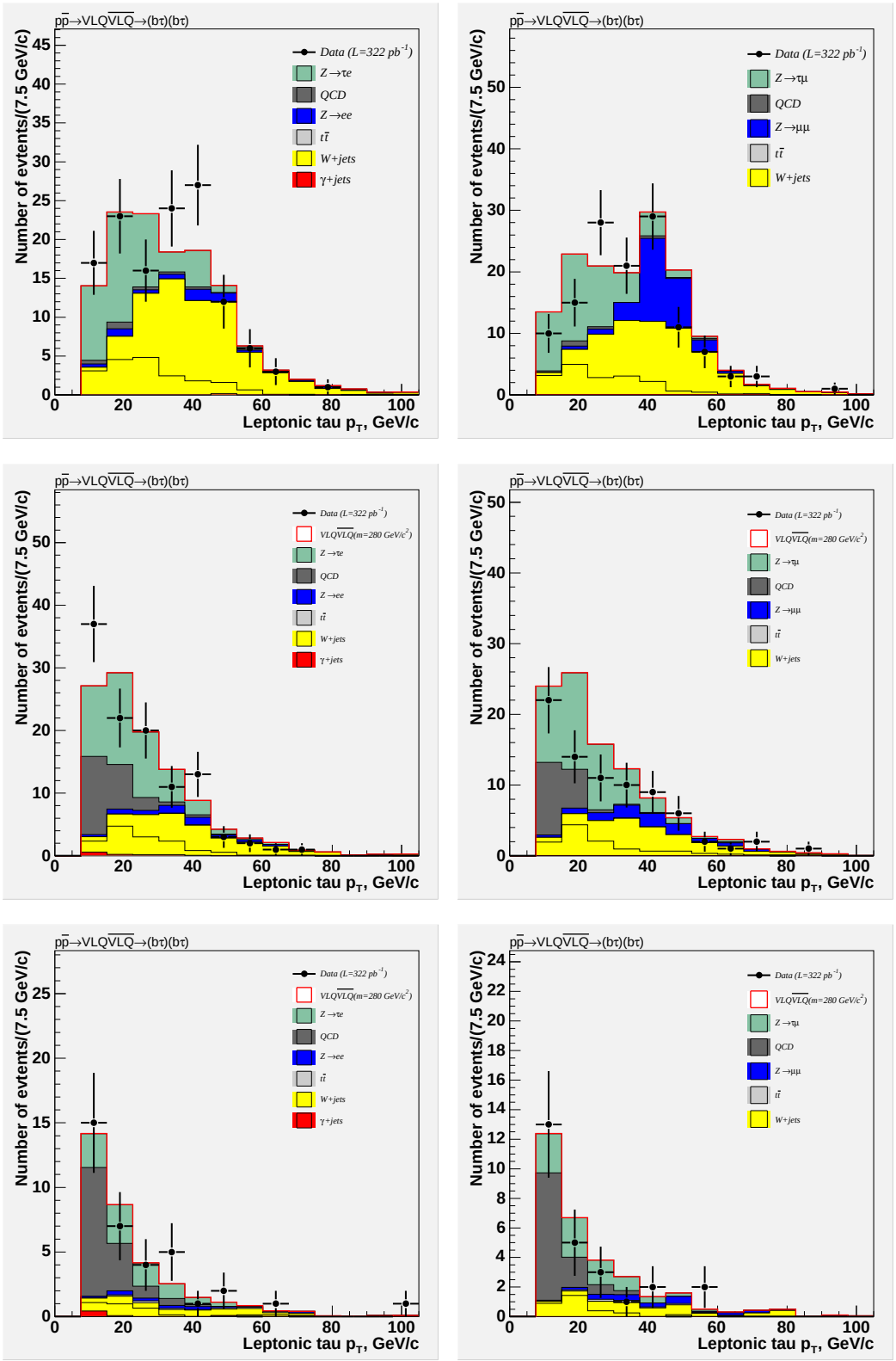

Figure 4.2: Distributions of electron E_T (left) and muon p_T (right) for control regions CR0J (top row), CR1J (middle row), and CR2J (bottom row).

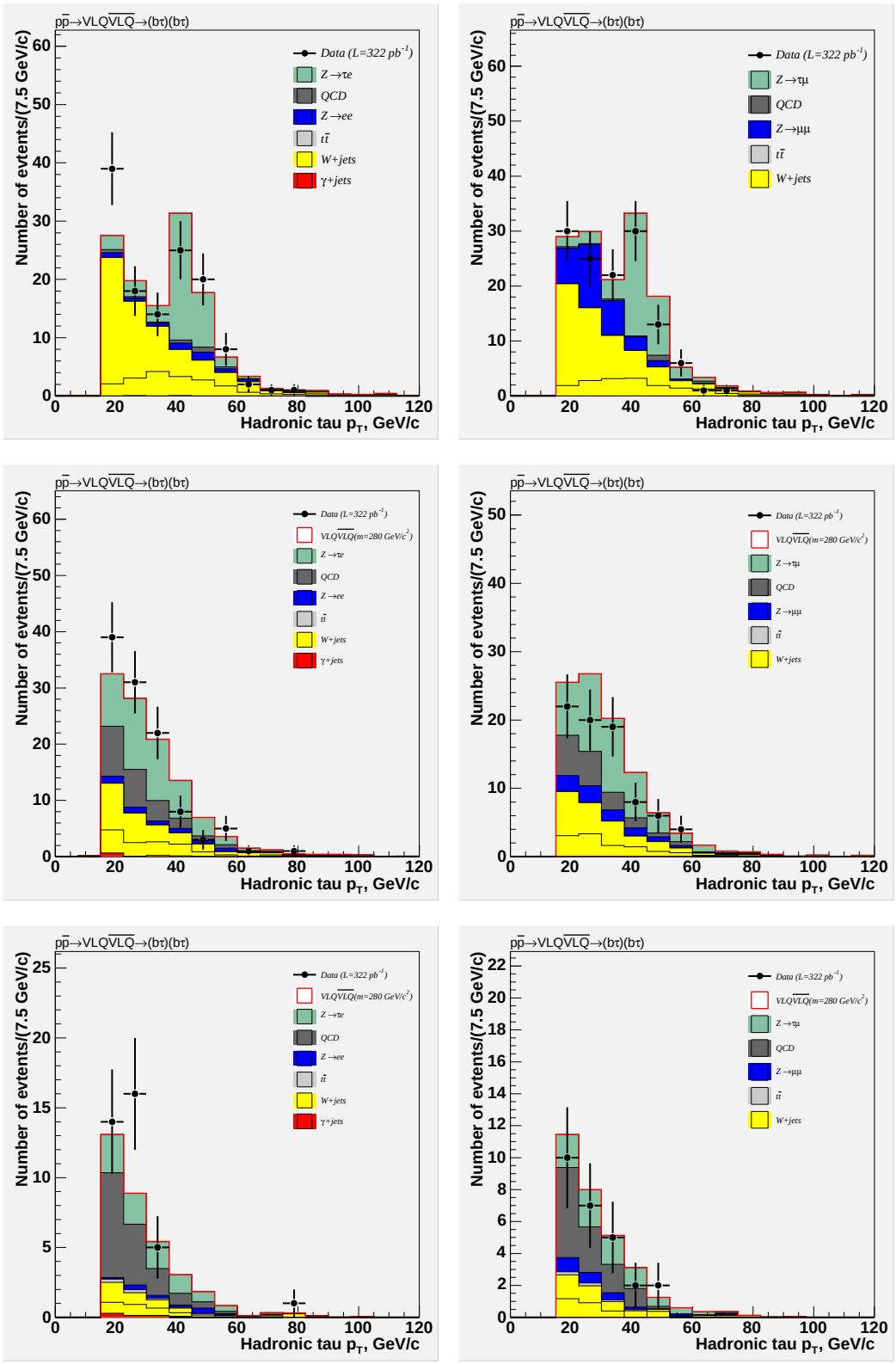

Figure 4.3: Distributions of hadronic tau p_T in the electron channel (left) and muon channel (right) for control regions CR0J (top row), CR1J (middle row), and CR2J (bottom row).

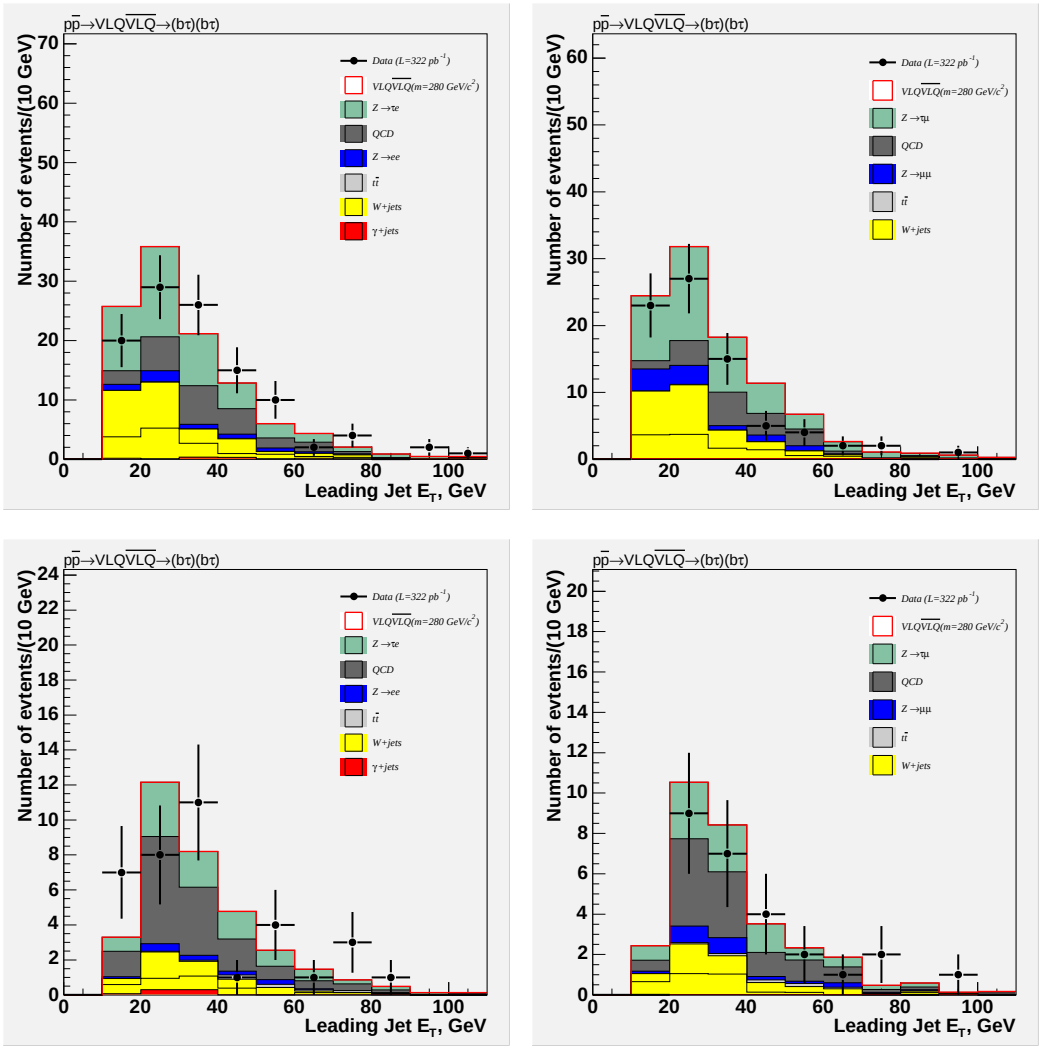

Figure 4.4: Distributions of leading jet E_T in the electron channel (left) and muon channel (right) for control regions CR1J (top), and CR2J (bottom). Note that this cross check does not apply to the CR0J region.

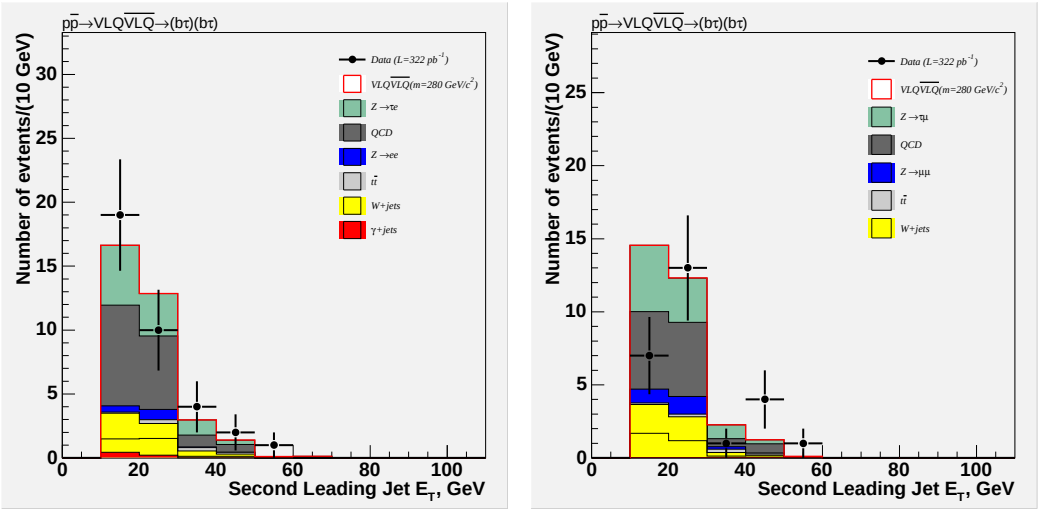

Figure 4.5: Distributions of second most leading jet E_T in the electron channel (left) and muon channel (right) for control region CR2J. Note that this cross check does not apply to the CR0J or CR1J regions.

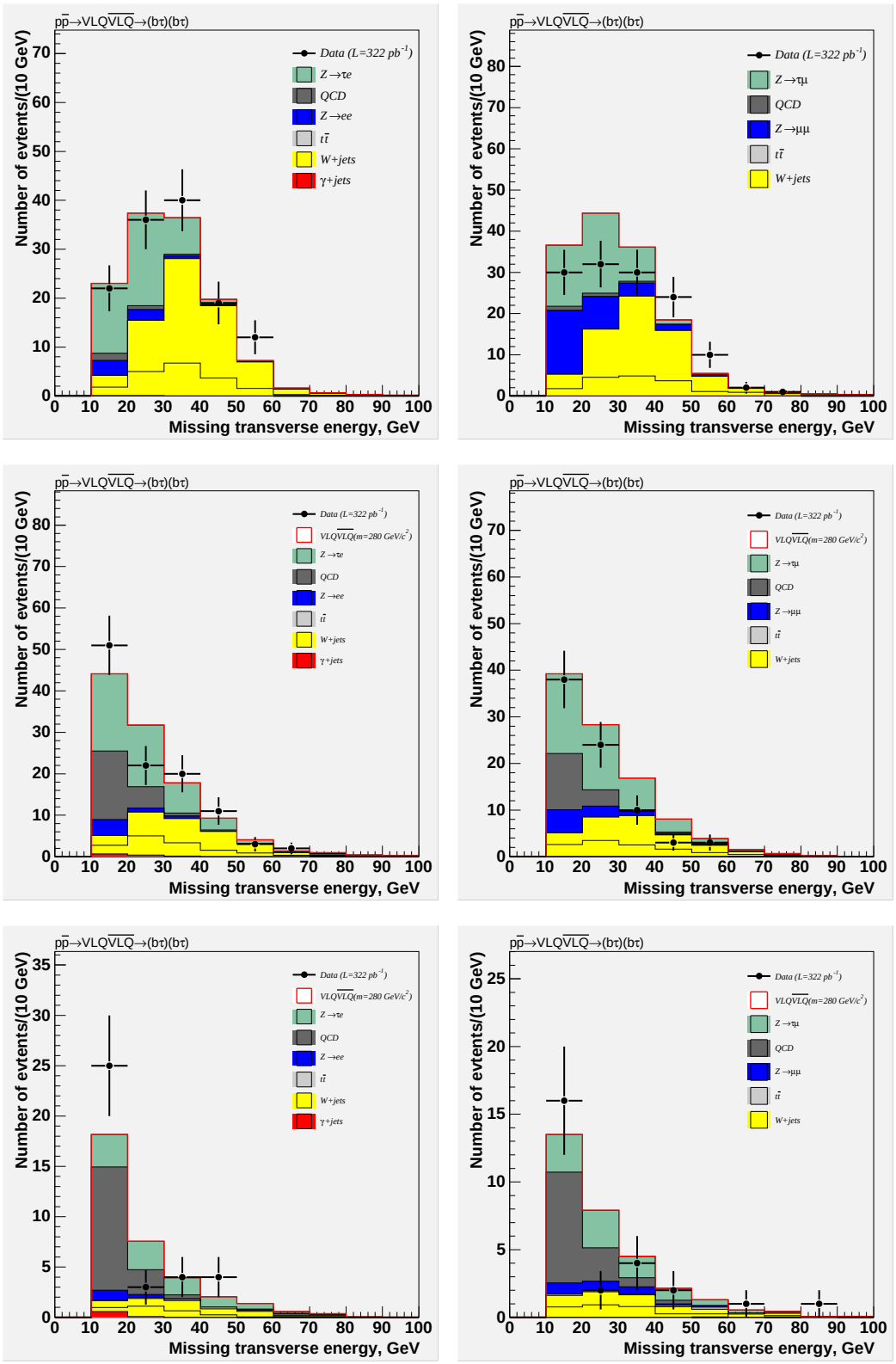

Figure 4.6: Distributions of $\not\!\!E_T$ in the electron channel (left) and muon channel (right) for control regions CR0J (top row), CR1J (middle row), and CR2J (bottom row).

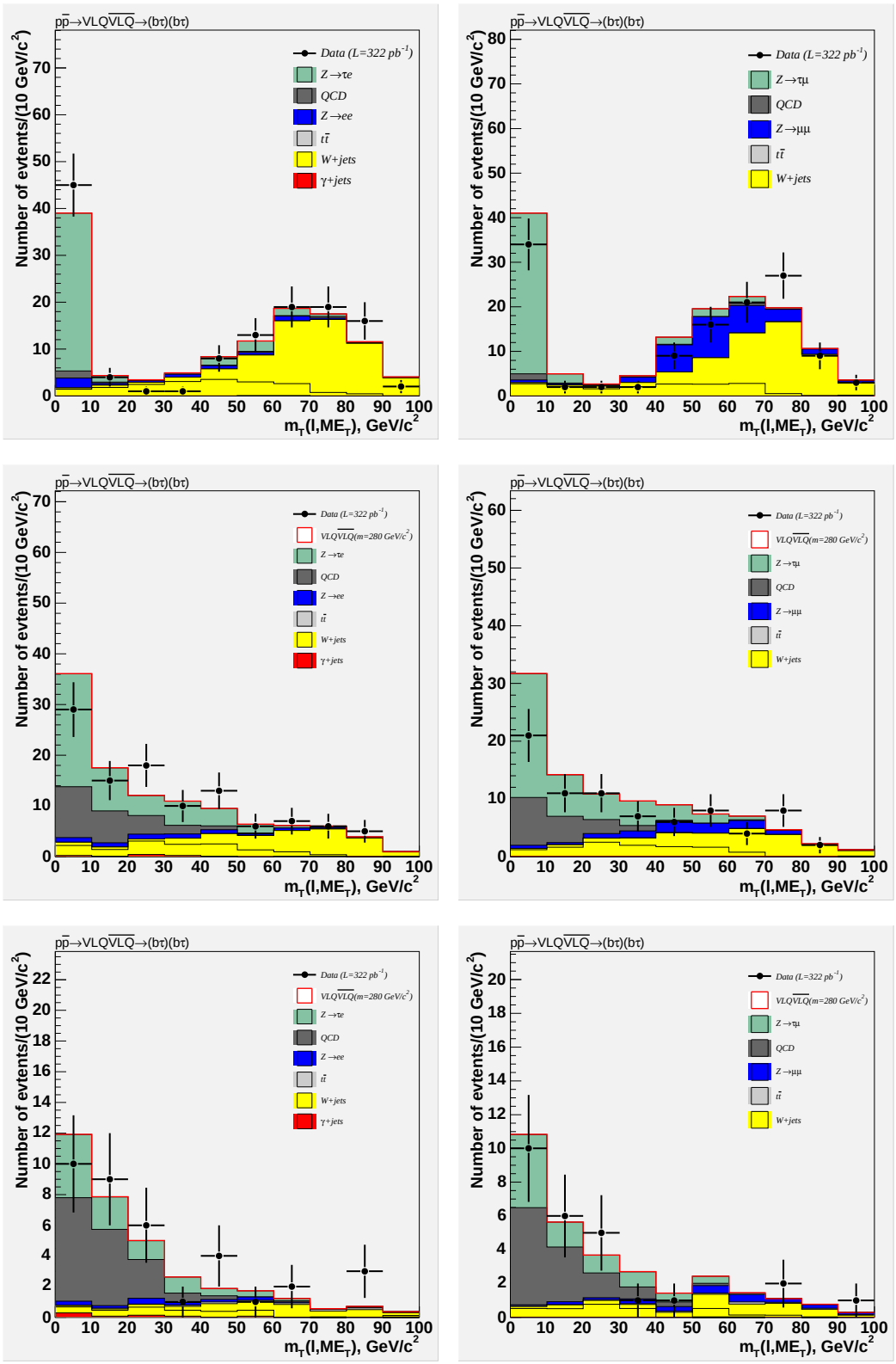

Figure 4.7: Distributions of M_T in the electron channel (left) and muon channel (right) for control regions CR0J (top row), CR1J (middle row), and CR2J (bottom row).

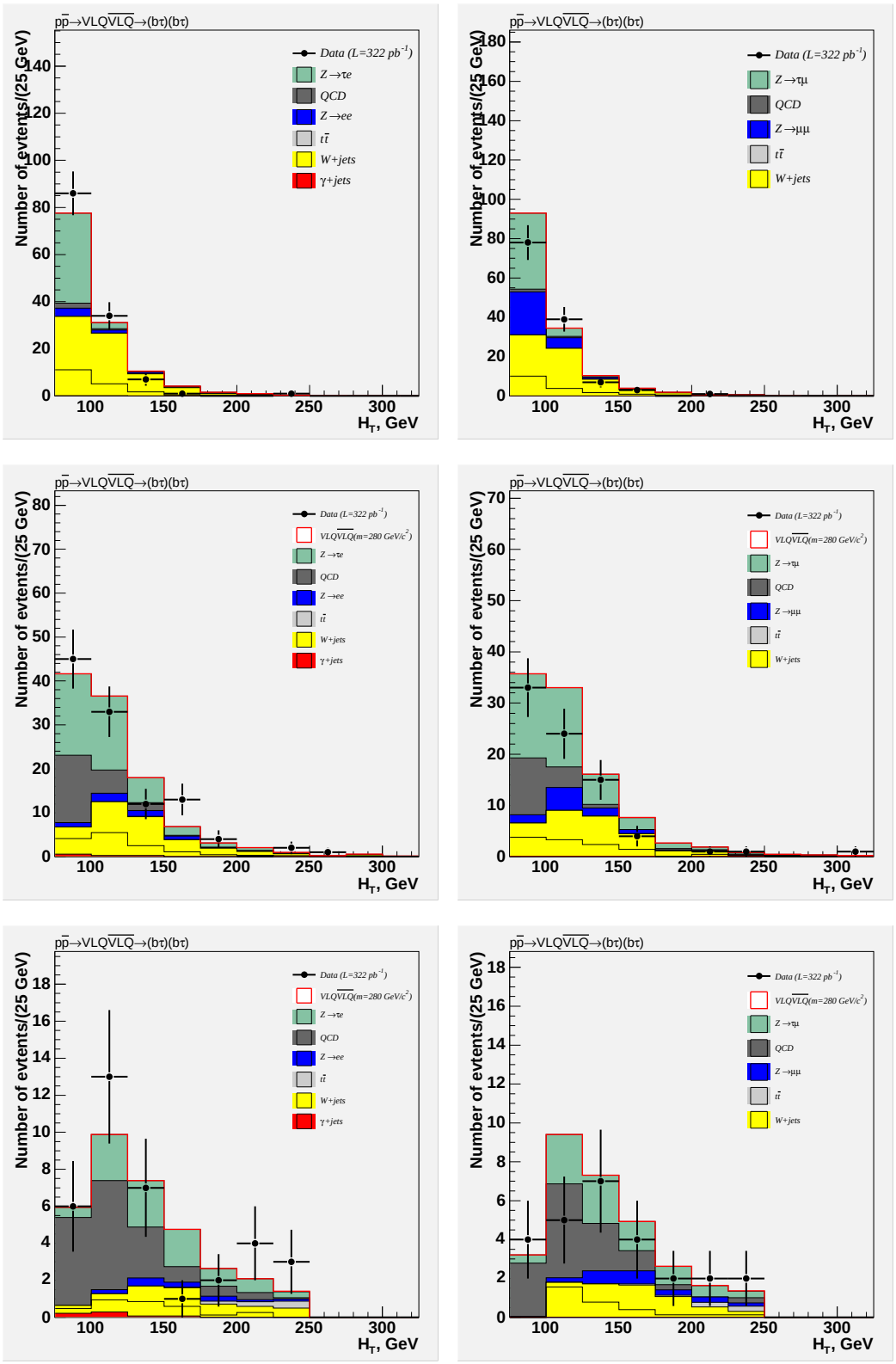

Figure 4.8: Distributions of H_T in the electron channel (left) and muon channel (right) for control regions CR0J (top row), CR1J (middle row), and CR2J (bottom row).

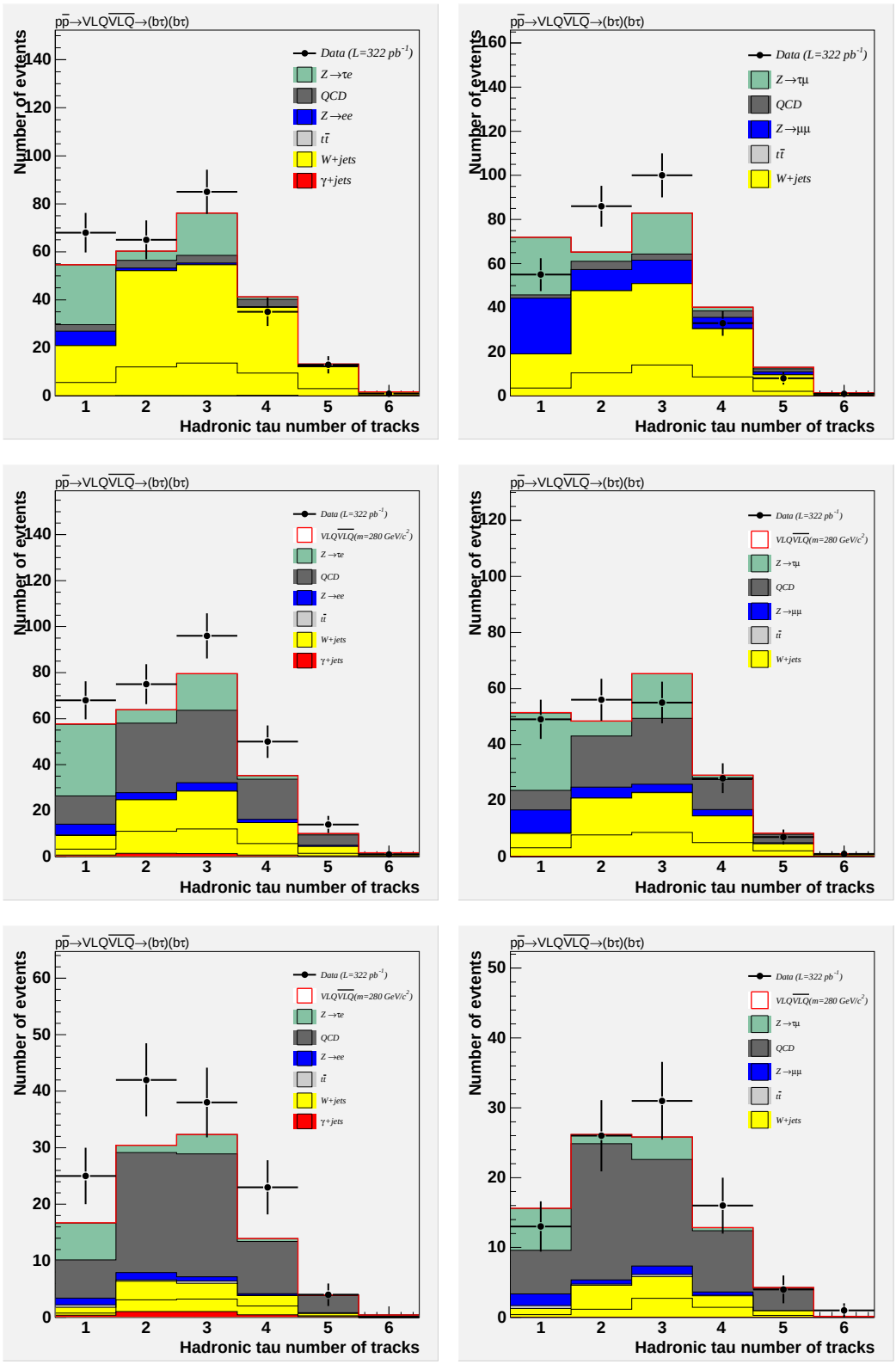

Figure 4.9: Distributions of N_{prongs} of the hadronic tau in the electron channel (left) and muon channel (right) for control regions CR0J (top row), CR1J (middle row), and CR2J (bottom row).

Chapter 5

Results and Discussion

5.1 Systematic Uncertainties

This section discusses the systematic uncertainties. Several of these uncertainties are either obtained from reference [44], or derived using similar techniques as used for the systematics of that analysis.

The standard uncertainty of 6% is applied to the integrated luminosity [36].

5.1.1 Uncertainties in the Event Selection

Parton Distribution Functions

To assign an uncertainty due to the choice of a Parton Distribution Function (PDF), we use a technique of weighting MC events. We follow the procedure described in [60], and illustrated in [61].

The considered PDFs are CTEQ5L (as the default), MRST72, MRST75, CTEQ6L, CTEC6L1, and 40 varieties of CTEQ6M. Half of the CTEQ6M varieties correspond to a negative variation of one of 20 eigenvectors and half correspond to a positive variation. The two main advantages of the MC weighting method are that a single MC sample can be used (as opposed to generating a sample for each PDF) and the correlations among the relatively similar PDFs are taken into account.

The weights are calculated as the product of the alternative PDF values for the proton partons and the antiproton partons, divided by the product of the default PDF values (used in the generator) for the proton partons and the antiproton partons. The ratio, between events that pass all analysis requirements and all events considered, of these weights, is then used for the selection uncertainty. They are combined for the different trial PDFs in a non-trivial way: If the positive and negative alternative PDFs produce shifts of the ratio that go in the corresponding positive or negative directions, then each variation is included in the corresponding positive or negative uncertainty. If both the positive and negative alternative PDFs produce shifts of the ratio that go in the same direction, then the mean of the squared variation is included in that side of the uncertainty but not in the

Table 5.1: Systematic uncertainties (in %) on full selection due to the choice of PDF, shown for the $e\tau_h$ and $\mu\tau_h$ channels. The prescription for calculating the positive and negative uncertainties is described in the text, and the two are averaged. The uncertainty due to α_s is combined in quadrature with the average to give the total.

$e\tau_h$	160 GeV/c^2 [%]	200 GeV/c^2 [%]	260 GeV/c^2 [%]	320 GeV/c^2 [%]	360 GeV/c^2 [%]
Positive	1.5	1.0	0.7	0.4	0.4
Negative	2.6	1.8	1.2	0.7	0.5
Average	2.0	1.4	0.9	0.6	0.4
α_s	1.2	1.2	0.6	0.7	0.5
Total	2.4	1.9	1.1	0.9	0.7
$\mu\tau_h$	160 GeV/c^2 [%]	200 GeV/c^2 [%]	260 GeV/c^2 [%]	320 GeV/c^2 [%]	360 GeV/c^2 [%]
Positive	1.6	0.8	0.5	0.6	0.3
Negative	3.1	1.1	0.8	1.0	0.7
Average	2.3	0.9	0.7	0.8	0.5
α_s	1.3	1.2	0.7	0.7	0.0
Total	2.7	1.5	1.0	1.1	0.5

other. For example, if both the PDFs produce a positive shift of the ratio, then the mean of the squared variation is included only in the positive uncertainty.

The resulting systematic uncertainties are shown in Table 5.1 for a range of LQ3 masses. The negative and positive uncertainties are averaged and then combined in quadrature with the uncertainty due to α_s, which is calculated using the ratio of the weights between the MRST72 and MRST75 PDFs.

There is a dependence on mass for the uncertainty due to PDF choice, and the uncertainties are smaller than those estimated for the RPV stop analysis [44]. This is likely due to the lower fraction, at higher LQ3 mass, of the gluon-gluon production component where the different PDF choices can have more impact, and also due to the larger parton momentum fraction. As an additional check, we produce a signal MC sample with $m_{\mathrm{LQ3}} = 100$ GeV/c^2 and find an average uncertainty due to PDF choice of 4.2%, which extends the range of the mass dependence, and is comparable to the level of uncertainty estimated for the mass range considered for the RPV stop analysis.

Jet Energy Scale

The jet energy scale systematic is evaluated using a standard procedure whereby the jet energy scale is shifted up and down by one σ and the number of events in the signal region under these two scenarios is compared to the nominal. The `JetUser` package allows for such shifts in the jet energy scale using routines related to the jet correction calculations. The changes, in percentages,

due to the $+1\sigma$ and -1σ variations are averaged to arrive at the systematic. These results are summarized in Table 5.2 for a range of LQ3 mass, for both the $e\tau_h$ and $\mu\tau_h$ channels.

Missing Transverse Energy

There is a small systematic uncertainty due to the imprecise knowledge of $\not\!\!E_T$. In particular, $\not\!\!E_T$ corrections include corrections for jets and taus. The correction due to jet energy is accounted for by the systematic discussed above. The systematic due to the taus is estimated by using a simpler tau cluster momentum calculation rather than the preferred expanded tau cluster momentum used in the default analysis. The change in the full selection with respect to the default yields the results shown in Table 5.3 for a range of LQ3 mass, for both the $e\tau_h$ and $\mu\tau_h$ channels.

Initial State Radiation and Final State Radiation

The systematic uncertainty due to the imperfect modeling of initial state radiation (ISR) and final state radiation (FSR) is measured by comparing the number of events that enter the signal region in the default configuration (with ISR and FSR both at a nominal level) to configurations with more or less ISR or FSR. This was done for the three mass points $m_{\mathrm{LQ3}} = 200$, 260, and 320 GeV/c^2. The results of the study are reported in Tables 5.4 and 5.5.

Acceptance, ID, and Isolation

Some of the systematic uncertainties due to the acceptance, ID, and isolation requirements mentioned in Section 3.3. They are repeated here for completeness. The uncertainty due to the electron ID was discussed in Section 3.3.2 and is 1.0%. The systematic for the muon ID comes from the references given in Section 3.3.2 and is 3.0%. The systematic due to the tau ID is 3.0% as shown in Section 3.3.2. As mentioned in Section 3.3.2, a systematic of 3.0% is used to cover the uncertainties in the isolation.

Summary of Systematics on the Full Selection

Table 5.4 shows a summary of the systematic uncertainties for the electron channel and Table 5.5 shows the uncertainties for the muon channel. The individual contributions are combined in quadrature to give the total uncertainties given at the bottom of each table.

5.1.2 Uncertainties in the Cross Section

Parton Distribution Functions

The systematic uncertainty on the cross section due to the choice of PDF is estimated with the Monte Carlo generator for the CTEQ6M PDFs. The positive and negative differences between the CTEQ6M eigenvectors and the default CTEQ6M are combined in the same way as for the systematic on the full selection, as discussed in Section 5.1.1. The resulting systematics, for a range of LQ3 masses, are reported in Table 5.6.

Table 5.2: Systematic uncertainties (given in %) on full selection due to the jet energy scale.

$e\tau_h$	m_{LQ3}						
	160	180	200	220	240	260	280
$+1\sigma$	7.2	5.8	5.1	4.6	3.6	2.4	1.7
-1σ	−7.7	−5.4	−5.3	−4.9	−4.4	−3.2	−2.6
Average	7.5	5.6	5.2	4.8	4.0	2.8	2.1
$e\tau_h$	m_{LQ3}						
	300	320	340	360	380	400	
$+1\sigma$	1.4	1.2	0.9	0.7	0.4	0.4	
-1σ	−2.3	−1.4	−1.1	−1.1	−0.7	−0.8	
Average	1.8	1.3	1.0	0.9	0.5	0.6	
$\mu\tau_h$	m_{LQ3}						
	160	180	200	220	240	260	280
$+1\sigma$	6.9	6.8	4.9	4.2	3.7	2.2	2.2
-1σ	−6.8	−6.8	−5.7	−4.7	−4.3	−3.3	−2.5
Average	6.8	6.8	5.3	4.4	4.0	2.7	2.4
$\mu\tau_h$	m_{LQ3}						
	300	320	340	360	380	400	
$+1\sigma$	1.5	1.5	1.0	0.7	0.5	0.3	
-1σ	−2.1	−1.4	−1.2	−0.9	−0.7	−0.6	
Average	1.8	1.4	1.1	0.8	0.6	0.4	

Table 5.3: Systematic uncertainties (given in %) on full selection due to the tau correction to the missing transverse energy.

	m_{LQ3}						
	160	180	200	220	240	260	280
$e\tau_h$ channel	−0.1	0.1	−0.1	0.0	0.0	−0.1	−0.1
$\mu\tau_h$ channel	0.0	0.1	0.1	−0.2	−0.1	0.1	−0.1
	m_{LQ3}						
	300	320	340	360	380	400	
$e\tau_h$ channel	−0.1	0.0	0.1	−0.1	0.0	0.0	
$\mu\tau_h$ channel	0.0	−0.1	0.1	0.0	0.1	0.0	

Table 5.4: Summary of systematic uncertainties for the $e\tau_h$ channel, given in %.

	m_{LQ3}												
Source	160	180	200	220	240	260	280	300	320	340	360	380	400
PDF	2.4	2.1	1.9	1.6	1.4	1.1	1.0	1.0	0.9	0.8	0.7	0.7	0.6
ISR	3.6	3.6	3.6	3.6	3.6	3.6	3.6	3.6	3.6	3.6	3.6	3.6	3.6
FSR	3.7	3.7	3.7	3.7	3.7	3.7	3.7	3.7	3.7	3.7	3.7	3.7	3.7
Jet Scale	7.5	5.6	5.1	4.8	4.0	2.8	2.1	1.8	1.3	1.0	0.9	0.5	0.6
$\not{E}_T$	0.1	0.1	0.1	0.0	0.0	0.1	0.1	0.1	0.0	0.1	0.1	0.0	0.0
Acceptance	1.7	1.7	1.7	1.7	1.7	1.7	1.7	1.7	1.7	1.7	1.7	1.7	1.7
Lepton ID	1.0	1.0	1.0	1.0	1.0	1.0	1.0	1.0	1.0	1.0	1.0	1.0	1.0
Tau ID	3.0	3.0	3.0	3.0	3.0	3.0	3.0	3.0	3.0	3.0	3.0	3.0	3.0
Isolation	3.0	3.0	3.0	3.0	3.0	3.0	3.0	3.0	3.0	3.0	3.0	3.0	3.0
Total	10.5	9.2	8.9	8.6	8.1	7.6	7.4	7.3	7.1	7.1	7.1	7.0	7.0

Table 5.5: Summary of systematic uncertainties for the $\mu\tau_h$ channel, given in %.

	m_{LQ3}												
Source	160	180	200	220	240	260	280	300	320	340	360	380	400
PDF	2.7	2.1	1.5	1.3	1.1	1.0	1.0	1.0	1.1	0.8	0.5	0.5	0.4
ISR	3.7	3.7	3.7	3.7	3.7	3.7	3.7	3.7	3.7	3.7	3.7	3.7	3.7
FSR	3.6	3.6	3.6	3.6	3.6	3.6	3.6	3.6	3.6	3.6	3.6	3.6	3.6
Jet Scale	6.9	6.8	5.3	4.4	4.0	2.7	2.4	1.8	1.4	1.1	0.8	0.6	0.4
$\not{E}_T$	0.0	0.1	0.1	0.2	0.1	0.1	0.1	0.0	0.1	0.1	0.0	0.1	0.0
Acceptance	1.0	1.0	1.0	1.0	1.0	1.0	1.0	1.0	1.0	1.0	1.0	1.0	1.0
Lepton ID	3.0	3.0	3.0	3.0	3.0	3.0	3.0	3.0	3.0	3.0	3.0	3.0	3.0
Tau ID	3.0	3.0	3.0	3.0	3.0	3.0	3.0	3.0	3.0	3.0	3.0	3.0	3.0
Isolation	3.0	3.0	3.0	3.0	3.0	3.0	3.0	3.0	3.0	3.0	3.0	3.0	3.0
Total	10.4	10.3	9.2	8.7	8.5	7.9	7.8	7.7	7.6	7.5	7.5	7.4	7.4

Table 5.6: Summary of systematic uncertainties on the cross section, given in %.

	m_{LQ3}					
Source	160	180	200	220	240	260
PDF						
Positive	7.0	7.1	7.5	7.7	7.9	8.4
Negative	−10.9	−11.1	−11.3	−11.4	−11.7	−12.0
Q^2						
$Q = 0.5m_{\mathrm{LQ3}}$	43.7	43.6	44.0	44.2	44.8	45.1
$Q = 2m_{\mathrm{LQ3}}$	−27.9	−28.2	−28.3	−28.3	−28.6	−28.9
Total +	44.1	44.2	44.6	44.9	45.5	45.9
Total −	−30.0	−30.3	−30.5	−30.5	−30.9	−31.3

	m_{LQ3}				
Source	280	300	320	340	360
PDF					
Positive	8.8	9.3	9.9	10.4	11.3
Negative	−12.4	−13.0	−13.6	−14.4	−15.0
Q^2					
$Q = 0.5m_{\mathrm{LQ3}}$	45.5	46.3	46.5	47.3	48.0
$Q = 2m_{\mathrm{LQ3}}$	−29.1	−29.3	−29.7	−30.0	−30.4
Total +	46.3	47.2	47.5	48.4	49.3
Total −	−31.6	−32.1	−32.7	−33.3	−33.9

Choice of Q^2 Scale

The dominant uncertainty on the LQ3 cross section comes from the choice of the Q^2 scale. The Q^2 value enters the simulation through several mechanisms, including the matrix elements, the ISR calculations, and the momentum available to the hard process. Here we have opted to follow the same course as the CDF RunII 1^{st} and 2^{st} generation leptoquark searches (see for example [62, 63, 64]) and use $Q = m_{\mathrm{LQ3}}$ as a default. For heavier objects such as a vector leptoquark, this may not be the most likely Q^2, but we take a self-consistent approach. We include the systematic as discussed below. Also, our LQ3 Monte Carlo simulation is of leading order, and the cross section is thus more dependent on Q^2 than it would be for a simulation of higher orders.

The systematic uncertainty is obtained by calculating the cross section, over a range of LQ3 masses, for the two cases: $Q = 2m_{\mathrm{LQ3}}$ and $Q = 0.5m_{\mathrm{LQ3}}$. The positive (negative) excursion of the cross section with respect to the default scenario of $Q = m_{\mathrm{LQ3}}$ is combined in quadrature with the positive (negative) uncertainty due to the PDF choice discussed in Section 5.1.2. The resulting systematics due to Q^2, and the total systematics on the cross section, are reported in Table 5.6.

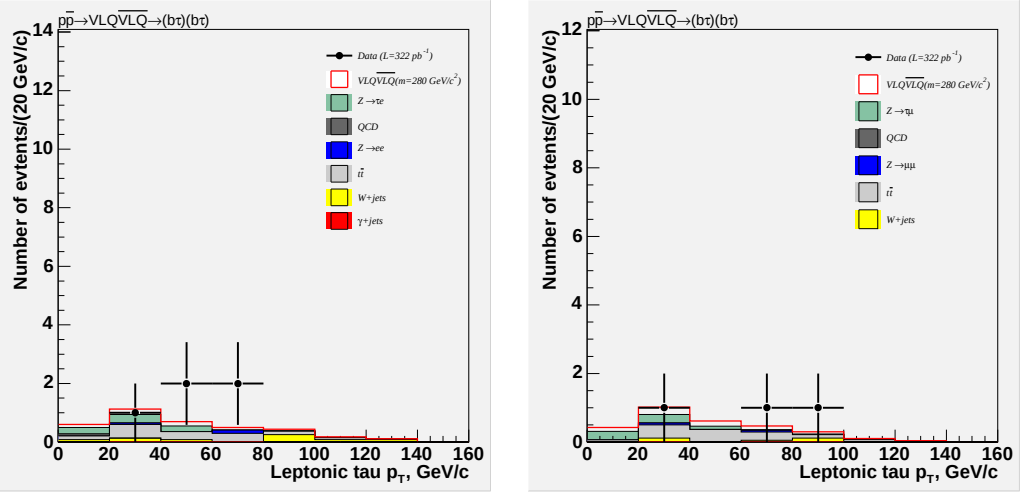

Figure 5.1: Distributions of electron E_T (left) and muon p_T (right) for the safety region.

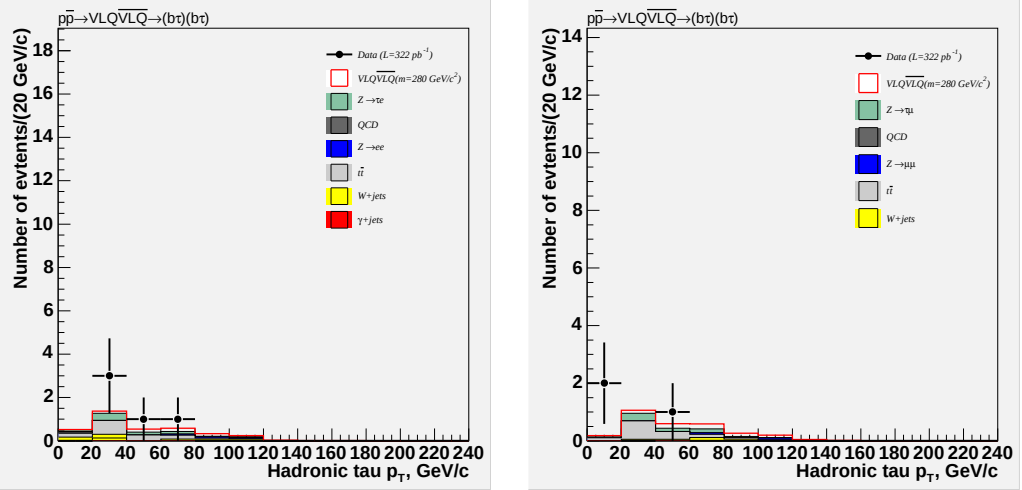

Figure 5.2: Distributions of hardronic tau p_T in the electron channel (left) and muon channel (right) for the safety region.

5.2 Safety Region Results

The safety region ($N_{\text{jets}} \geq 2$ and $250 < H_T < 400$ GeV) contains 5 events in the $e\tau_h$ channel and 3 events in the $\mu\tau_h$ channel. The systematic uncertainties in safety region are shown in Table 5.7 for Jet Energy Scale and in Table 5.8 for Missing Transverse Energy. The full acceptances are summarized in Table 5.9 and in Table 5.10.

The kinematic distributions are shown in Figures 5.1- 5.8. The signal and background yields in the safety region are included in Table 5.12 for the $e\tau_h$ channel and in Table 5.13 for the $\mu\tau_h$ channel.

Table 5.7: Systematic uncertainties (given in %) in safety region due to the jet energy scale.

$e\tau_h$	m_{LQ3}						
	160	180	200	220	240	260	280
$+1\sigma$	-1.8	-3.9	-6.3	-7.9	-9.7	-8.3	-8.4
-1σ	1.2	2.3	5.2	7.8	10.5	12.4	13.9
$Average$	1.5	3.1	5.7	7.8	10.1	10.3	11.2
$e\tau_h$	m_{LQ3}						
	300	320	340	360	380	400	
$+1\sigma$	-12.1	-12.3	-13.7	-15.8	$-11.4.4$	-12.0	
-1σ	14.5	12.1	12.3	18.5	11.4	18.0	
$Average$	13.3	12.2	13.0	17.2	11.4	15.0	
$\mu\tau_h$	m_{LQ3}						
	160	180	200	220	240	260	280
$+1\sigma$	-3.9	-4.5	-3.9	-8.5	-11.6	-9.3	-15.1
-1σ	0.0	2.0	6.7	7.7	8.6	10.7	11.1
$Average$	2.0	3.2	5.3	8.1	9.9	10.0	13.1
$\mu\tau_h$	m_{LQ3}						
	300	320	340	360	380	400	
$+1\sigma$	-9.1	-16.4	-11.5	-11.5	-9.5	-14.7	
-1σ	12.9	17.1	15.6	18.0	9.5	16.0	
$Average$	11.0	16.8	13.5	14.5	9.5	15.3	

Table 5.8: Systematic uncertainties (given in %) in safety region due to the tau correction to the missing transverse energy.

	m_{LQ3}						
	160	180	200	220	240	260	280
$e\tau_h$ channel	0.1	-0.3	-0.1	0.3	0.1	0.4	0.8
$\mu\tau_h$ channel	-0.1	-0.1	-0.3	0.5	0.2	-0.6	0.0
	m_{LQ3}						
	300	320	340	360	380	400	
$e\tau_h$ channel	0.8	0.4	-0.5	-0.8	-0.5	0.0	
$\mu\tau_h$ channel	-0.5	0.0	-0.8	-1.0	-1.6	0.0	

Table 5.9: Full acceptance table in SAFE and SR regions for $e\tau_h$

m_{VLQ3} (GeV/c^2)	SAFE (%)	SR (%)
160	2.47 ± 0.05	2.05 ± 0.05
180	2.47 ± 0.05	2.85 ± 0.05
200	2.23 ± 0.05	3.61 ± 0.06
220	1.84 ± 0.04	4.10 ± 0.06
240	1.49 ± 0.04	4.75 ± 0.07
260	1.15 ± 0.03	5.24 ± 0.07
280	0.83 ± 0.03	5.63 ± 0.07
300	0.62 ± 0.02	5.78 ± 0.07
320	0.46 ± 0.02	5.96 ± 0.07
340	0.35 ± 0.02	6.12 ± 0.08
360	0.24 ± 0.02	6.18 ± 0.08
380	0.20 ± 0.01	6.22 ± 0.08
400	0.14 ± 0.01	6.23 ± 0.08

Table 5.10: Full acceptance table in SAFE and SR regions for $\mu\tau_h$

m_{VLQ3} (GeV/c^2)	SAFE (%)	SR (%)
160	2.63 ± 0.05	2.28 ± 0.05
180	2.61 ± 0.05	2.97 ± 0.05
200	2.32 ± 0.05	3.69 ± 0.06
220	1.98 ± 0.04	4.45 ± 0.07
240	1.63 ± 0.04	4.81 ± 0.07
260	1.21 ± 0.03	5.44 ± 0.07
280	0.93 ± 0.03	5.63 ± 0.07
300	0.68 ± 0.03	5.80 ± 0.07
320	0.53 ± 0.02	6.05 ± 0.08
340	0.37 ± 0.02	6.09 ± 0.08
360	0.28 ± 0.02	6.12 ± 0.08
380	0.18 ± 0.01	6.12 ± 0.08
400	0.13 ± 0.01	5.91 ± 0.07

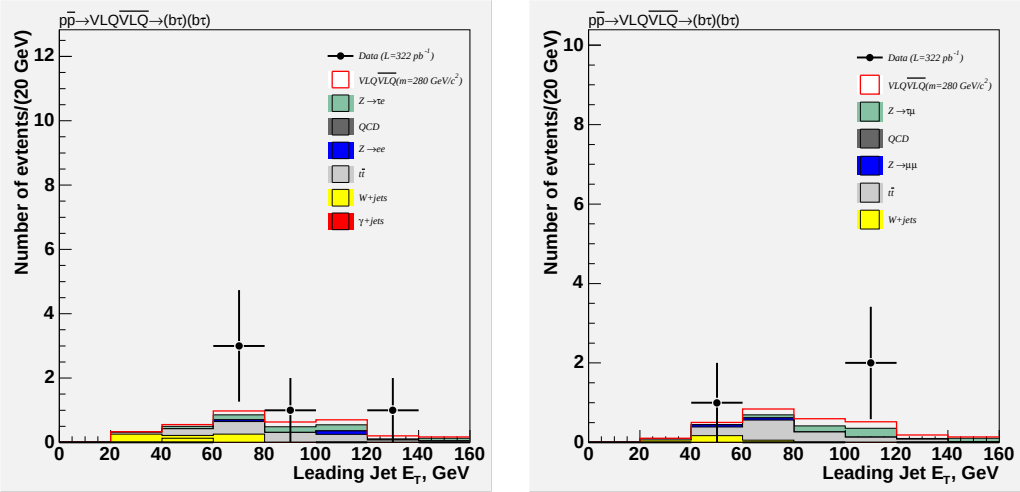

Figure 5.3: Distributions of the leading jet E_T in the electron channel (left) and muon channel (right) for the safety region.

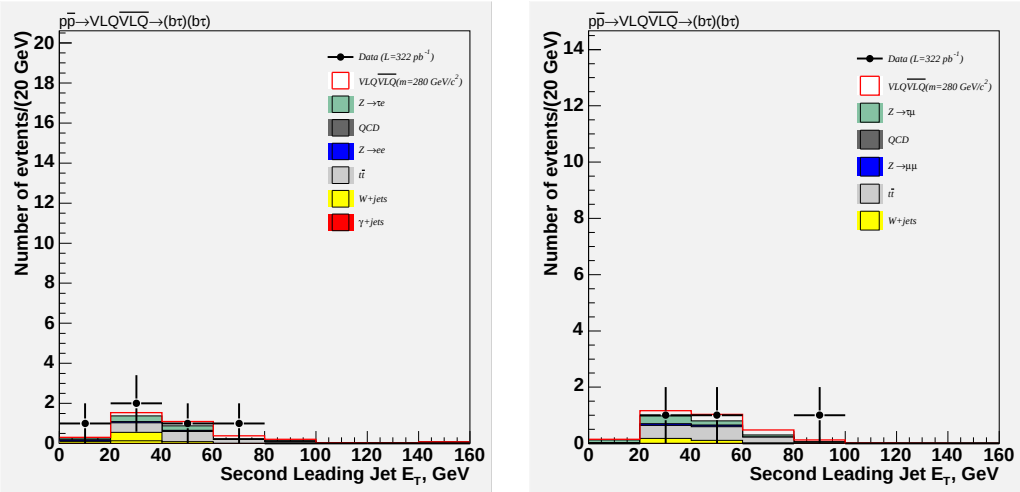

Figure 5.4: Distributions of the second jet E_T in the electron channel (left) and muon channel (right) for the safety region.

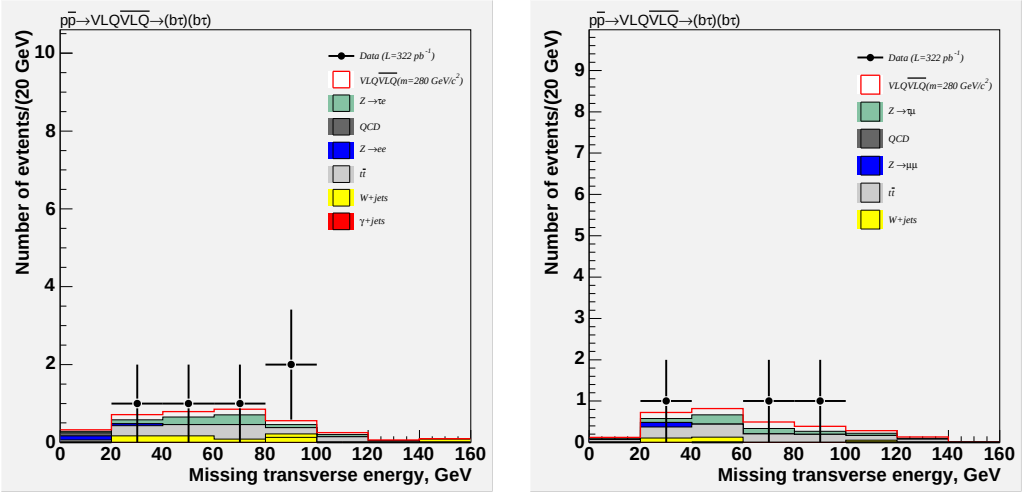

Figure 5.5: Distributions of $\not\!\!E_T$ in the electron channel (left) and muon channel (right) for the safety region.

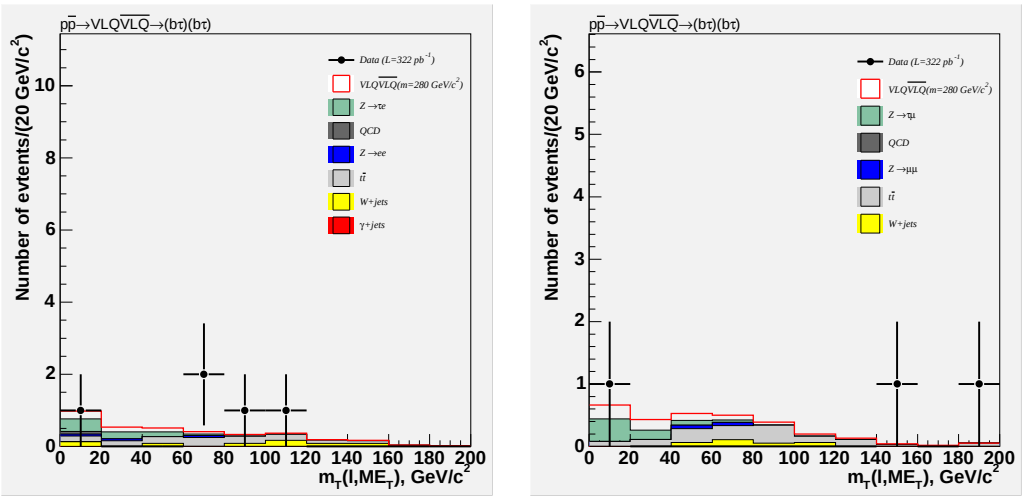

Figure 5.6: Distributions of M_T in the electron channel (left) and muon channel (right) for the safety region.

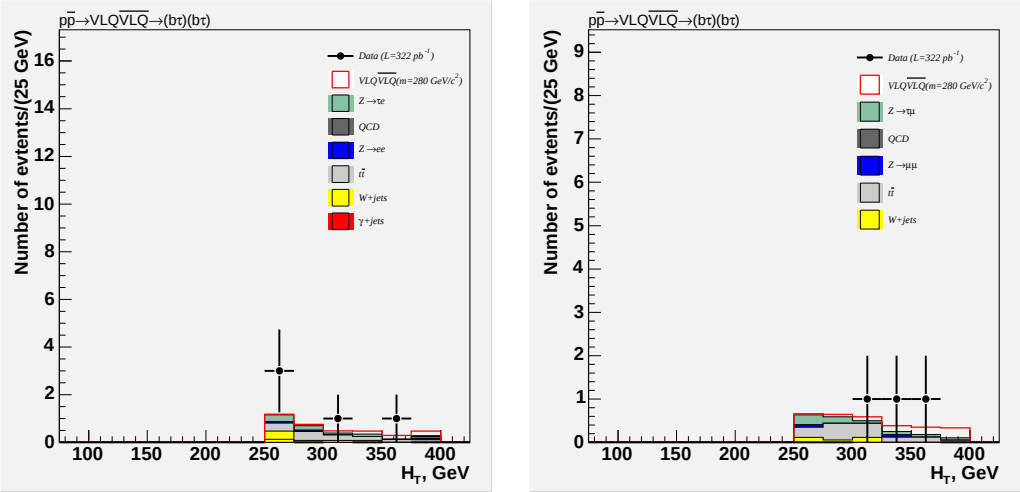

Figure 5.7: Distributions of H_T in the electron channel (left) and muon channel (right) for the safety region.

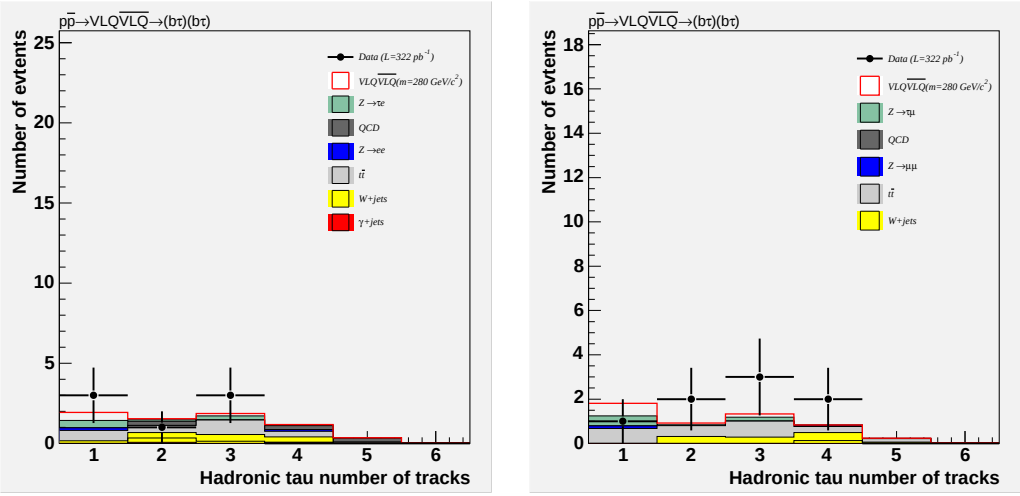

Figure 5.8: Distributions of N_{prongs} in the electron channel (left) and muon channel (right) for the safety region.

5.3 Signal Region Results

After all of the analysis requirements, background estimates, and control region checks were finalized, the signal region was studied. The signal region ($N_{\text{jets}} \geq 2$ and $H_T > 400$ GeV) contains 0 events in the $e\tau_h$ channel and 0 events in the $\mu\tau_h$ channel.

5.4 Combined Fit

5.4.1 Fit Method

As discussed earlier, the signal region has optimal sensitivity to the highest possible mass limit in the absence of the signal of new physics. However, the existing limit on the leptoquark mass is rather low compared to the sensitivity of the current analysis. Thus, if leptoquarks exist with a true mass substantially lower than the high mass region targeted in this analysis, a significant part of the leptoquark signal will appear in the SAFE region. Therefore, to ensure high sensitivity of the analysis to lower mass leptoquarks, while still exploring the high mass range, the fit procedure utilizes both the signal and safety regions, treating them essentially as separate bins.

	$250 < H_T < 400$	$400 < H_T < \infty$
$e\tau_h$ channel	A1	A2
$\mu\tau_h$ channel	B1	B2

Table 5.11: Definition of four regions used in the fitting procedure.

We build the likelihood function as follows: we start with full rates of signal and background processes, ν_i in each of the four regions $i = A1,\ B1,\ A2,\ B2$ (defined in Table 5.11):

$$\nu_i = \nu_i^b + \nu_i^s \tag{5.1}$$

and use Poisson probability to calculate the probability of the true rates being within $d\nu_i$ of ν_i given the number of observed events N_i:

$$d\mathcal{P} = \prod_{i=A1,B1,A2,B2} P(\nu_i, N_i) d\nu_i, \tag{5.2}$$

where $P(\nu_i, N_i)$ is the Poisson distribution for the expected rate ν_i. We then perform a transformation of variables $(\nu_i) \rightarrow (\nu_i^s)$ (assuming backgrounds are known exactly for now, but including the uncertainties later). The Jacobian of this transformation is unity. Finally, we replace the signal rate in region i with a physically meaningful cross-section using $\nu_i^s = \sigma_i(\text{VLQ3}\overline{\text{VLQ3}}) \times L \times \text{Br}(\tau\tau \rightarrow \tau_l\tau_h) \times \alpha_i$ (for the time being, we allow for different experimental cross-sections for each region), where α_i is the full selection efficiency of signal events for region i, and L is the integrated luminosity. The Jacobian of this transformation is $L^3 \prod \alpha_i$ (up to a constant). We then include prior knowledge about the acceptances and the fact that there must be a unique cross-section, regardless of region, by introducing an additional prior of the form:

$$\delta(\sigma_{A1} - \sigma_{B1})\delta(\sigma_{A2} - \sigma_{B2})\delta(\sigma_{B1} - \sigma_{A2}), \tag{5.3}$$

which reduces the number of integration variables by three.

Then, we take into account that in each region the portion of the backgrounds obtained using MC scales with the luminosity by breaking each rate into luminosity dependent and luminosity independent parts: $\nu_i^b = \nu_i^{b'} + \nu_i^{b''}(L - L_0)/L_0$ (L is the same L as in the signal rate estimation so that they are integrated together). Next, we take into account the uncertainties in the background rates by introducing a gaussian prior (the non-physical cases of negative background rates are explicitly cut off in the final integral).

Lastly, we incorporate a mechanism for correlated systematic uncertainties by replacing the background rates with:

$$\nu_i^b + \sum x_k \delta_k \nu_i^b, \tag{5.4}$$

where x_k is a parameter determining the degree of variation in the k^{th} systematic effect (e.g. if the systematics is taken to be a gaussian, $x_k = 1$ would corresponds to a one sigma deviation) and $\delta_k \nu_i^b$ is a measure of the systematic effect on the background rate. We perform exactly the same modification to the acceptances:

$$\alpha_i \to \alpha_i + \sum x_k \delta_k \alpha_i^b. \tag{5.5}$$

Parameters x_k become additional integration variables in the final likelihood, and we supply their priors in the form of $exp(-x_k^2/2)$.

At this point, the likelihood is constructed and we integrate out the nuisance parameters (all parameters except the cross-section σ). The Likelihood is in fact a probability density function. We use 95% C.L. highest posterior density intervals to determine the maximum allowed cross-section value, which we report as the final limit as a function of leptoquark mass. Given that we end up observing no new physics signal, this is equivalent to just integrating the likelihood function from $\sigma = 0$ to the point where 95% of the full integral is reached.

5.4.2 Fit Results

The fit gives the 95% C.L. upper limit on the LQ3 pair production cross section at each mass point that is probed. The results are plotted in Figure 5.9. The red and blue curves containing data points are the experimental results given by the fitter for the cases of Yang-Mills and Minimal couplings, respectively. The smooth red and blue curves are the corresponding theoretical cross sections as discussed in Section 1.2. The intersection of the experimental curves and corresponding central theoretical curves determine the 95% C.L. upper limit LQ3 pair production cross section, and the 95% C.L. lower limit on the LQ3 mass. Likewise, the intersection of the experimental curves and the -1σ theoretical curves give the limits that include the theoretical uncertainty. The results are quoted in the next section.

The result is a 95% C.L. upper limit on the VLQ3 pair production cross section of $\sigma < 344$ fb, assuming Yang-Mills couplings and Br(LQ3 $\to b\tau$) $= 1$, and a lower limit on the VLQ3 mass of $m_{\text{VLQ3}} > 317$ GeV/c^2. If theoretical uncertainties on the cross section are applied, the results are $\sigma < 353$ fb and $m_{\text{VLQ3}} > 303$ GeV/c^2. For a VLQ3 with Minimal couplings, the upper limit

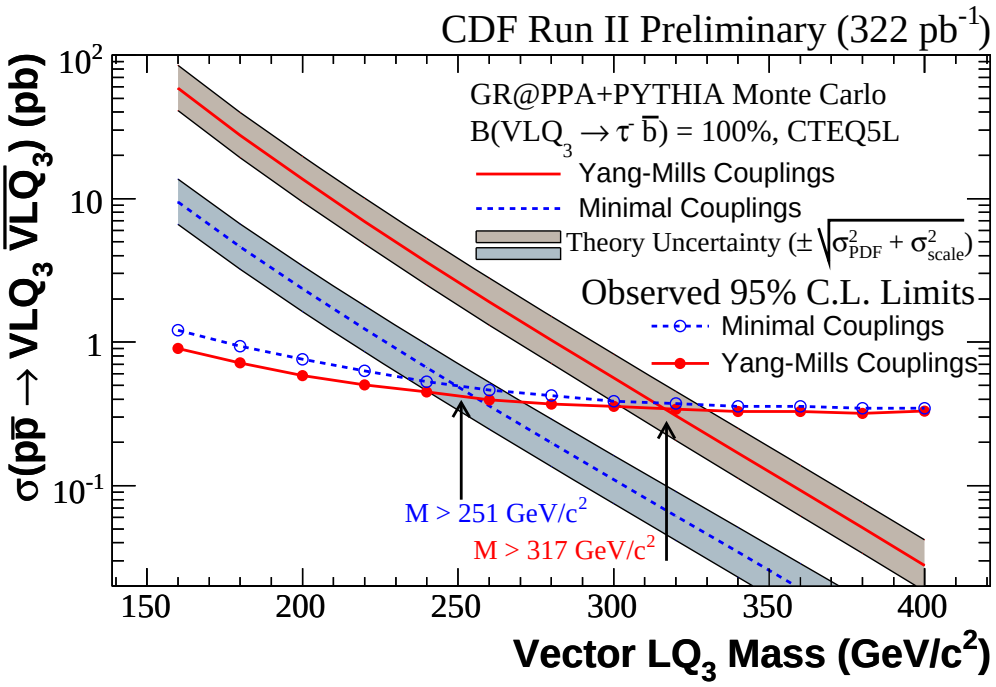

Figure 5.9: Pair production cross section as a function of LQ3 mass for experimental results (curves with data points) and theory predictions (solid curves) for the cases of Yang-Mills couplings (red) and Minimal couplings (blue). The band due to the uncertainty on the theoretical prediction for the cases of Yang-Mills couplings (brown) and Minimal couplings (gray) are also shown, and includes the uncertainty due to the choices of PDF and Q^2 scale.

on the cross section is $\sigma < 493$ fb ($\sigma < 554$ fb) and the lower limit on the mass is $m_{\mathrm{VLQ3}} > 251$ GeV/c^2 ($m_{\mathrm{VLQ3}} > 235$ GeV/c^2) for the nominal (1σ varied) theoretical expectation.

These results for both coupling cases are imploved from CDF Run I, which the lower mass limits are $m_{\mathrm{VLQ3}} > 225$ GeV/c^2 for Yang-Mills couplings and $m_{\mathrm{VLQ3}} > 170$ GeV/c^2 for Minimal couplings.

Table 5.12: Event estimates for the $e\tau_h$ channel. The number of events are given for each background category, the sum of the backgrounds, and for the data. For each number, the statistical uncertainty is given first, followed by the systematic uncertainty. The regions CR0J, CR1J, CR2J, SAFE, and SIGNAL are defined in Section 4.2.

	CR0J	CR1J	CR2J
Backgrounds:			
$Z^0 \to \tau\tau \to e\tau_h$	$39.86^{+0.85}_{-0.85} \pm 3.22$	$43.02^{+0.88}_{-0.88} \pm 3.80$	$9.09^{+0.41}_{-0.41} \pm 1.06$
$Z^0 \to ee$	$5.45^{+0.55}_{-0.55} \pm 1.12$	$6.62^{+0.61}_{-0.61} \pm 1.47$	$1.22^{+0.26}_{-0.26} \pm 0.33$
QCD	$2.83^{+0.47}_{-0.47} \pm 0.32$	$22.66^{+1.32}_{-1.32} \pm 5.63$	$15.23^{+1.08}_{-1.08} \pm 3.85$
$t\bar{t}$	$0.01^{+0.01}_{-0.0} \pm 0.01$	$0.30^{+0.06}_{-0.06} \pm 0.07$	$0.81^{+0.09}_{-0.09} \pm 0.22$
$W(\to e\nu) + \text{jets}$	$53.06^{+1.13}_{-1.13} \pm 9.82$	$20.29^{+0.79}_{-0.79} \pm 4.87$	$3.51^{+0.35}_{-0.35} \pm 1.72$
$W(\to \tau\nu) + \text{jets}$	$20.68^{+1.43}_{-1.43} \pm 4.43$	$14.90^{+1.37}_{-1.37} \pm 3.73$	$2.87^{+0.64}_{-0.64} \pm 1.99$
$\gamma + \text{jets}$	$0.18^{+0.18}_{-0.09} \pm 0.00$	$1.44^{+0.36}_{-0.36} \pm 0.29$	$0.66^{+0.07}_{-0.00} \pm 0.18$
Total Background	$122.08^{+2.14}_{-2.14} \pm 11.31$	$109.23^{+2.35}_{-2.35} \pm 9.27$	$33.39^{+1.40}_{-1.39} \pm 4.80$
Data	129	110	36

	SAFE	SIGNAL
Backgrounds:		
$Z^0 \to \tau\tau \to e\tau_h$	$0.67^{+0.11}_{-0.11} \pm 0.15$	$0.04^{+0.04}_{-0.02} \pm 0.00$
$Z^0 \to ee$	$0.45^{+0.19}_{-0.13} \pm 0.10$	$0.00^{+0.06}_{-0.00} \pm 0.00$
QCD	$0.08^{+0.12}_{-0.05} \pm 0.00$	$0.00^{+0.08}_{-0.00} \pm 0.00$
$t\bar{t}$	$1.35^{+0.12}_{-0.12} \pm 0.39$	$0.15^{+0.04}_{-0.04} \pm 0.04$
$W(\to e\nu) + \text{jets}$	$0.60^{+0.15}_{-0.15} \pm 0.29$	$0.07^{+0.07}_{-0.04} \pm 0.03$
$W(\to \tau\nu) + \text{jets}$	$0.14^{+0.23}_{-0.09} \pm 0.08$	$0.00^{+0.14}_{-0.00} \pm 0.00$
$\gamma + \text{jets}$	$0.00^{+0.09}_{-0.00} \pm 0.00$	$0.00^{+0.09}_{-0.00} \pm 0.00$
Total Background	$3.28^{+0.40}_{-0.27} \pm 0.52$	$0.25^{+0.21}_{-0.06} \pm 0.05$
Data	5	0

Table 5.13: Event estimates for the $\mu\tau_h$ channel. The number of events are given for each background category, the sum of the backgrounds, and for the data. For each number, the statistical uncertainty is given first, followed by the systematic uncertainty. The regions CR0J, CR1J, CR2J, SAFE, and SIGNAL are defined in Section 4.2.

	CR0J	CR1J	CR2J
Backgrounds:			
$Z^0 \to \tau\tau \to \mu\tau_h$	$42.03^{+0.87}_{-0.87} \pm 2.91$	$40.10^{+0.85}_{-0.85} \pm 2.22$	$8.34^{+0.39}_{-0.39} \pm 0.70$
$Z^0 \to \mu\mu$	$27.06^{+1.19}_{-1.19} \pm 8.45$	$8.39^{+0.66}_{-0.66} \pm 2.74$	$2.20^{+0.34}_{-0.34} \pm 0.73$
QCD	$2.30^{+0.56}_{-0.56} \pm 0.39$	$16.54^{+1.50}_{-1.50} \pm 2.91$	$11.58^{+1.25}_{-1.25} \pm 2.05$
$t\bar{t}$	$0.04^{+0.03}_{-0.02} \pm 0.00$	$0.32^{+0.06}_{-0.06} \pm 0.07$	$0.67^{+0.08}_{-0.08} \pm 0.13$
$W(\mu+\nu)+\text{jets}$	$56.60^{+1.59}_{-1.59} \pm 7.98$	$21.99^{+1.12}_{-1.12} \pm 4.23$	$4.36^{+0.53}_{-0.53} \pm 1.74$
$W(\tau+\nu)+\text{jets}$	$19.11^{+1.37}_{-1.37} \pm 2.71$	$13.13^{+1.28}_{-1.28} \pm 2.56$	$3.44^{+0.70}_{-0.70} \pm 2.53$
Total Background	$147.13^{+2.62}_{-2.62} \pm 12.29$	$100.46^{+2.51}_{-2.51} \pm 6.74$	$30.58^{+1.62}_{-1.62} \pm 3.83$
Data	129	79	26

	SAFE	SIGNAL
Backgrounds:		
$Z^0 \to \tau\tau \to \mu\tau_h$	$0.59^{+0.10}_{-0.10} \pm 0.06$	$0.09^{+0.05}_{-0.03} \pm 0.03$
$Z^0 \to \mu\mu$	$0.10^{+0.10}_{-0.05} \pm 0.04$	$0.00^{+0.05}_{-0.00} \pm 0.00$
QCD	$0.00^{+0.13}_{-0.00} \pm 0.00$	$0.00^{+0.13}_{-0.00} \pm 0.00$
$t\bar{t}$	$1.24^{+0.11}_{-0.11} \pm 0.29$	$0.15^{+0.04}_{-0.04} \pm 0.05$
$W(\mu+\nu)+\text{jets}$	$0.31^{+0.18}_{-0.11} \pm 0.11$	$0.00^{+0.06}_{-0.00} \pm 0.00$
$W(\tau+\nu)+\text{jets}$	$0.00^{+0.14}_{-0.00} \pm 0.00$	$0.00^{+0.14}_{-0.00} \pm 0.00$
Total Background	$2.25^{+0.32}_{-0.20} \pm 0.32$	$0.24^{+0.22}_{-0.05} \pm 0.05$
Data	3	0

Chapter 6

Conclusion

We have searched for a third generation vector leptoquark (VLQ3) in the di-tau plus di-jet channel in proton-antiproton collisions at $\sqrt{s} = 1.96$ TeV. The data was taken with the Collider Detector at Fermilab (CDF) in Run II. We used the data corrected using the *Lepton+Track* triggers. The corresponding integrated luminosity of the data used in this analysis was 322 pb^{-1}.

The model being explored is that of third generation vector leptoquark pair production, followed by the subsequent decay of each VLQ3 to a b quark and a tau lepton ($\beta = 1$). And, This search explores a vector like Yang-Mills couplings ($\kappa = \lambda = 0$) as well as minimal couplings ($\kappa = 1$ and $\lambda = 0$).

In this analysis, we defined the signal region as having $N_{\text{jets}} \geq 2$ and $H_T > 400$ GeV. This is the region for which the analysis has been optimized. The safety region has $N_{\text{jets}} \geq 2$ and $250 < H_T < 400$ GeV, and serves as a buffer between the signal region and the control region. The control region below $H_T = 250$ GeV will not be sensitive to a vector leptoquark heavier than the existing limit of $m_{\text{LQ3}} > 225$ GeV/c^2, while the safety region of $250 < H_T < 400$ GeV could have such sensitivity. Therefore, the data in the safety region had not been examined until the control region studies were completed. And, the final result uses a simultaneous fit to both the safety and signal regions.

In the safety region ($N_{\text{jets}} \geq 2$ and $250 < H_T < 400$ GeV), we found 5 events in the $e\tau_h$ channel and 3 events the $\mu\tau_h$ channel, while the total background is expected to be $3.28^{+0.40}_{-0.27}(stat.) \pm 0.52(syst.)$ in the $e\tau_h$ channel and $2.25^{+0.32}_{-0.20}(stat.) \pm 0.32(syst.)$ events in the $\mu\tau_h$ channel,

The signal region ($N_{\text{jets}} \geq 2$ and $H_T > 400$ GeV) contains 0 events in the $e\tau_h$ channel and 0 events in the $\mu\tau_h$ channel, while the total backgound is expected to be $0.25^{+0.21}_{-0.06}(stat.) \pm 0.05(syst.)$ in the $e\tau_h$ channel and $0.24^{+0.22}_{-0.05}(stat.) \pm 0.05(syst.)$ in the $\mu\tau_h$ channel. Thus no significant excess is observed.

We obtained a 95% C.L. upper limit on the VLQ3 pair production cross section of $\sigma < 344$ fb, and a lower limit on the VLQ3 mass of $m_{\text{VLQ3}} > 317$ GeV/c^2, assuming Yang-Mills couplings and Br(LQ3 $\rightarrow b\tau$) $= 1$. If 1σ theoretical uncertainties on the cross section are included, the results are $\sigma < 353$ fb and $m_{\text{VLQ3}} > 303$ GeV/c^2. For a VLQ3 with Minimal couplings, the upper limit on the cross section is $\sigma < 493$ fb ($\sigma < 554$ fb) and the lower limit on the

mass is $m_{\mathrm{VLQ3}} > 251\ \mathrm{GeV}/c^2$ ($m_{\mathrm{VLQ3}} > 235\ \mathrm{GeV}/c^2$) for the nominal ($1\sigma$ varied) theoretical expectation.

We have improved the lower limits on the VLQ3 mass at the CDF Run I, where the lower limits on the VLQ3 mass are $m_{\mathrm{VLQ3}} > 225\ \mathrm{GeV}/c^2$ for Yang-Mills couplings and $m_{\mathrm{VLQ3}} > 170\ \mathrm{GeV}/c^2$ for Minimal couplings.

Bibliography

[1] H. Georgi and S. L. Glashow,
"Unity Of All Elementary Particle Forces,"
Phys. Rev. Lett. **32**, 438 (1974).

[2] J. C. Pati and A. Salam,
"Lepton Number As The Fourth Color,"
Phys. Rev. D **10**, 275 (1974).

[3] B. Schrempp and F. Schrempp,
"Light Leptoquarks,"
Phys. Lett. B **153**, 101 (1985).

[4] E. Farhi and L. Susskind,
"Technicolor,"
Phys. Rept. **74**, 277 (1981).
E. Eichten, I. Hinchliffe, K. D. Lane and C. Quigg,
"Signatures For Technicolor,"
Phys. Rev. D **34**, 1547 (1986).
S. F. King,
"Dynamical Electroweak Symmetry Breaking,"
Rept. Prog. Phys. **58**, 263 (1995).

[5] W. M. Yao *et al.* [Particle Data Group],
"Review of particle physics,"
J. Phys. G **33**, 1 (2006).

[6] W. Buchmüller, R. Rückl, D. Wyler,
"Leptoquarks in lepton quark collisions,"
Phys. Lett. B **191**, 442 (1987).

[7] F. Abe *et al.* [CDF Collaboration],
"Search for third generation leptoquarks in $\bar{p}p$ collisions at $\sqrt{s} = 1.8$ TeV,"
Phys. Rev. Lett. **78**, 2906 (1997).

[8] Tom Baumann, Melissa Franklin, Colin Gay, Jorge Troconiz,
"Search For Third Generation Leptoquarks in the DiTau Plus DiJet Channel,"
CDF Internal Note 3597 (1996).

[9] J. Blumlein, E. Boos and A. Kryukov,
"Leptoquark pair production in hadronic interactions,"
Z. Phys. C **76**, 137 (1997).

[10] J. Blumlein and R. Ruckl,
"Production of scalar and vector leptoquarks in e+ e- annihilation,"
Phys. Lett. B **304**, 337 (1993).

[11] J.R. Smith, Soushi Tsuno,
"Leptoquark Generator for Hadron Colliders,"
CDF Internal Note 7934 (2005).

[12] C. Adloff *et al.* [H1 Collaboration],
"Observation of events at very high Q**2 in e p collisions at HERA,"
Z. Phys. C **74**, 191 (1997).

[13] J. Breitweg *et al.* [ZEUS Collaboration],
"Comparison of ZEUS data with standard model predictions for e+ p $\rightarrow$ e+ X scattering at high x and Q**2,"
Z. Phys. C **74**, 207 (1997)

[14] "New Results on Neutral and Charged Current Scattering at high Q^2 from H1 and ZEUS,"
Hamburg, Germany, July 28 - August 1 1997.

[15] H1 BSM Working Group,
"New Results on NC and CC-like Events at Very High Q^2 in DIS Collisions at HERA,"
July 1997.

[16] F. Abe *et al.* [CDF Collaboration],
"Search for first generation leptoquark pair production in $p\bar{p}$ collisions at $\sqrt{s} = 1.8$ TeV,"
Phys. Rev. Lett. **79**, 4327 (1997)

[17] B. Abbott *et al.* [D0 Collaboration],
"Search for scalar leptoquark pairs decaying to electrons and jets in $\bar{p}p$ collisions,"
Phys. Rev. Lett. **79**, 4321 (1997).

[18] C. Grosso-Pilcher, G. Landsberg and M. Paterno [CDF Collaboration],
"Combined limits on first generation leptoquarks from the CDF and D0 experiments,"
arXiv:hep-ex/9810015.

[19] M. Kramer,
"Leptoquark production at the Tevatron,"
arXiv:hep-ph/9707422.

[20] G. Chiarelli,
"Search for new physics at colliders,"
AIP Conf. Proc. **815**, 268 (2006).

[21] G. Aubrecht *et al.*,
"A Teachers Guide to the Nuclear Science Wall Chart,"
Contemporary Physics Education Project, 2003,
`http://www.lbl.gov/abc/wallchart/teachersguide/pdf/Chap11.pdf`.

[22] C. W. Schmidt,
"The Fermilab 400-MeV Linac upgrade,"
FERMILAB-CONF-93-111 (1993).

[23] Fermilab Beams Division,
"Run-II Handbook,"
`http://www-bd.fnal.gov/runII/index.html`.

[24] J. Marriner,
"Stochastic Cooling Overview,"
FERMILAB-CONF-03-158 (2003).

[25] R. Blair *et al.*,
"The CDF-II detector: Technical Design Report,"
FERMILAB-PUB-96/390-E (1996).

[26] F. Abe *et al.* [CDF Collaboration],
"The CDF detector: an overview,"
Nucl. Instrum. Meth. A **271**, 387 (1988).

[27] T. K. Nelson *et al.*,
FERMILAB-CONF-01/357-E.

[28] A. Sill *et al.*,
Nucl. Instrum. Methods A **447**, 1 (2000).

[29] T. Affolder *et al.*,
Nucl. Instrum. Methods A **485**, 6 (2002).

[30] K. T. Pitts *et al.*,
FERMILAB-CONF-96-443-E.

[31] `http://penn01.fnal.gov/~cot/`

[32] R. Brun, K. Hakelberg, M. Hansroul, and J.C. Lasalle,
CERN-DD-78-2,
CERN-DD-78-2-REV.

[33] CDF collaboration,
"Measurement of the B Hadron Masses in Exclusive J/ψ Decay Channels,"
CDF Public Note 6963.

[34] D. Acosta *et al.* [CDF Collaboration],
"A Time-of-Flight detector in CDF-II,"
Nucl. Instrum. Methods A **518**, 605 (2004).

[35] `http://huhepl.harvard.edu/~cmx/cdfnotes/`

[36] For sources used in luminosity uncertainty, see
http://www-cdf.fnal.gov/~konigsb/lum_official_page.html and
http://www-cdf.fnal.gov/~konigsb/TotalLumUncertainty-04-09-15.pdf.

[37] V. Martin,
"High-Pt Muon ID Cuts and Efficiencies for use with 5.3.1 Data and 5.3.3 MC,"
CDF Internal Note 7367 (2005).

[38] S. Baroiant *et al.*,
"Measurement of $Z \to \tau\tau$ Cross-Section -Electron Channel,"
CDF Internal Note 6552 (2004).

[39] S. Baroiant *et al.*,
"Measurement of $\sigma(Z \to \tau\tau)Br(Z \to \tau\tau)$ in $p\overline{p}$ Collisions at $\sqrt{s} = 1.96\,\mathrm{TeV}$,"
CDF Internal Note 8132 (2006).

[40] S. Baroiant *et al.*,
"Measurement of $Z \to \tau\tau$ Cross-Section Measurement,"
CDF Internal Note 7589 (2005).

[41] F. Abe *et al.* [CDF Collaboration],
"The Topology of three jet events in $\bar{p}p$ collisions at $\sqrt{s} = 1.8$ TeV,"
Phys. Rev. D**45**, 1448 (1992).

[42] J-F Arguin *et al.*,
"Generic Jet Energy Corrections for Run II data used for the Winter Conferences,"
CDF Internal Note 6280 (2003).

[43] J-F Arguin *et al.*,
"Jet Corrections for Summer 2003 Analysis,"
CDF Internal Note 6565 (2003).

[44] V. Khotilovich *et al.*,
"Search for Pair Production of Stop Quarks Decaying to τ and a b Jet,"
CDF Internal Note 7704 (2005).

[45] C. Hill *et al.*,
"Electron Identification in Offline Release 5.3,"
CDF Internal Note 7309 (2005).

[46] A. Soha *et al.*,
"Electron ID Efficiencies for Intermediate p_T Using $\Upsilon \to e^+e^-$ Events,"
CDF Internal Note 7713 (2005).

[47] V. Martin,
"High-p_T muons, recommended cuts and efficiencies for release 5.3,"
CDF Internal Note 7031 (2004).

[48] S. Baroiant *et al.*,
"Measurement of the Electron Trigger Efficiencies for Level1 and Level2 8 GeV Triggers,"
CDF Internal Note 6257 (2003).

[49] S. Baroiant *et al.*,
"Measurement of Level3 Trigger Efficiency for 8 GeV Inclusive Electron Trigger Using Conversions,"
CDF Internal Note 6324 (2003).

[50] Z. Wan *et al.*,
"Muon Trigger Efficiencies for v5.3 Tau Data,"
CDF Internal Note 7837 (2005).

[51] S. Baroiant *et al.*,
"XFT Efficiency for the Isolated Track Leg of the Electron+Track Trigger,"
CDF Internal Note 6510 (2003).

[52] S. Baroiant *et al.*,
"Lepton+Track Triggers: Measurement of the Level3 Trigger Efficiency for Taus,"
CDF Internal Note 6553 (2003).

[53] S. Baroiant *et al.*,
"Measurement of Tau ID Efficiencies for the First 72 pb^{-1} of CDF Run II Data,"
CDF Internal Note 7013 (2004).

[54] E. Halkiadakis *et al.*,
"A Conversion Removal Algorithm for the 2003 Winter Conferences,"
CDF Internal Note 6250 (2003).

[55] D. Gerdes,
"Study of Conversion Removal for the Lepton+Jets Sample,"
CDF Internal Note 2903 (1995).

[56] A. Taffard,
"Run II Cosmic Ray tagger,"
CDF Internal Note 6100 (2003).

[57] Jon Insler, Sarah Demers, Kevin McFarland and Tony Vaiciulis,
"Determining the Electron Fake Rate to Hadronic taus from the Data,"
CDF Internal Note 6408 (2003).

[58] Sarah Demers, Kevin McFarland and Anthony Vaiciulis,
"Checking muon to tau fake with $Z \to \mu\mu$ data,"
CDF Internal Note 6954 (2003).

[59] Stephane Tourneur and Aurore Savoy-Navarro,
"A method to estimate the tau fake rate: from dijet to W+jets,"
CDF Internal Note 8208 (2006).

[60] See
http://cdfrh0.grid.umich.edu/%7Emiller/pdf/pdf_ acceptance.html.

[61] O. Gonzalez, C. Rott,
"Uncertainties due to the PDFs for the gluino-sbottom search,"
CDF Internal Note 7051 (2004).

[62] S. Rolli *et al.*,
"Search For First Generation Scalar Leptoquarks" ($1^{\rm st}$ generation scalar leptoquarks in LQ$\to eqeq$ and LQ$\to eq\nu_e q$),
CDF Internal Note 7181 (2004).

[63] D. Tsybychev, Ph.D. Thesis, University of Florida
"Search For First-Generation LeptoQuarks In The Jets And Missing Transverse Energy Topology In Proton-Antiproton Collisions At Center-Of-Mass Energy $1.96\,\mathrm{TeV}$,"
CDF Internal Note 7636 (2005).

[64] D. Ryan, Ph.D Thesis, Tufts University
"Direct Searches for Scalar Leptoquarks at the Run II Tevatron"
($2^{\rm nd}$ generation scalar leptoquarks in LQ$\to \mu q\mu q$ and LQ$\to \mu q\nu_\mu q$),
CDF Internal Note 7425 (2005).